Critical features of colossal magnetoresistive manganites

Y Tokura

Department of Applied Physics, University of Tokyo, Tokyo 113-8656, Japan
and
Correlated Electron Research Center (CERC), National Institute for Advanced Industrial
Science and Technology (AIST), Tsukuba 305-8562, Japan
and
ERATO Spin Superstructure (ERATO-SSS) Project, Japan Science and Technology
Agency (JST), c/o AIST, Tsukuba 305-8562, Japan

Abstract

Colossal magnetoresistance (CMR) phenomena are observed in the perovskite-type hole-doped
manganites in which the double-exchange ferromagnetic metal phase and the charge–orbital
ordered antiferromagnetic phase compete with each other. The quenched disorder arising
from the inherent chemical randomness or the intentional impurity doping may cause major
modifications in the electronic phase diagram as well as in the magnetoelectronic properties
near the bicritical point that is formed by such a competition of the two phases. One is the
phase separation phenomenon on various time-scales (from static to dynamic) and on various
length-scales (from glass-like nano to grain-like micron). The other is the enhanced phase
fluctuation with anomalous reduction in the transition temperatures of the competing phases
(and hence in the bicritical-point temperature). The highly effective suppression of such a
phase fluctuation by an external magnetic field is assigned here to the most essential ingredient
of the CMR physics. Such profound and dramatic features as appearing in the bicritical region
are extensively discussed in this paper with ample examples of the material systems specially
designed for this purpose. The unconventional phase-controls over the competing phases in
terms of magnetic/electric fields and photo-excitations are also exemplified.

(Some figures in this article are in colour only in the electronic version)

Contents

1. Introduction

The terminology 'colossal magnetoresistance' (CMR) [1] was coined to distinguish the gigantic negative magnetoresistance observed in the perovskite-related manganese oxides (manganites), as exemplified for the case of $La_{2/3}Ca_{1/3}MnO_3$ in figure 1, from the giant magnetoresistance (GMR) observed in transition metal systems in multilayer or granular forms. The MR in the perovskite manganites near the Curie temperature (T_C) was already known at a very early stage of the study on transition-metal oxides. For example, the paper in 1969 by Searle and Wang [2] reported thoroughly the magnetic field dependence of the resistivity for a flux-grown crystal of $La_{1-x}Pb_xMnO_3$, in particular the large MR near T_C, as well as the phenomenological analysis. Soon after, Kubo and Ohata [3] gave a theoretical account for this phenomenon using the so-called double-exchange Hamiltonian (or the s–d model with on-site ferromagnetic interaction), which includes the essential ingredient of the double-exchange mechanism elaborated by Zener [4], Anderson and Hasegawa [5] and de Gennes [6]. Interest in the MR of these manganites has been revived of late since the rediscovery of the CMR phenomena or even the more astonishing magnetic field induced insulator–metal [7–11] and/or lattice-structural [12] transitions. At present, the perovskite manganites are the most representative materials system which can show versatile unconventional electronic-lattice structural changes or insulator–metal transitions upon stimulation by external stimuli, not only by magnetic field but also by irradiation with light [13], x-rays [14] and electron-beams [15] as well as current injection [16]. The underlying mechanism for such electronic phase transitions is believed to be common to that of CMR. The purpose of this review paper is to coherently describe the physical origin of CMR and the related electronic and lattice-structural changes in terms of the concept of phase competition and multi-criticality, while taking ample examples of the experimental results.

The physics of CMR is also closely related to the *bad metal* features which are ubiquitously observed in the conducting transition-metal oxides with strong electron–electron (electron correlation) and/or electron–lattice interactions. The correlated electrons, which are almost localized on the respective atomic sites, bear three attributes, namely, charge, spin and orbital degrees of freedom [17]. The conduction electrons with an orbital degree of freedom (3d e_g orbitals) are scattered not only by the strong electron correlation (or spin correlation dependent) effect but also by the strong electron–lattice coupling termed the Jahn–Teller interaction. The collective or local Jahn–Teller distortions, as described by the displacement of the oxygen ions surrounding Mn sites, are observed everywhere when the compound shows the dramatic resistive (e.g. insulator-to-metal) or magnetic (e.g. antiferromagnetic-to-ferromagnetic) transitions. The possibility of phase inhomogeneity or phase separation has often been argued as the essential ingredient in CMR physics [18], which is also considered in this paper as one of the inherent features under the *bicritical* phase competition. The nomenclature '*bicritical*' used throughout this paper stands for the critical features emerging around the first-order phase transition boundary as formed by some two competing phases. When the phase stability is represented as the phase diagram plotted in the plane of temperature versus some control parameter, the respective phases are bifurcated by the first-order transition line, usually parallel to the temperature axis. The bifurcation temperature in the phase plane gives rise to the *bicritical point*, near which many unconventional features including CMR are expected to show up. In the present case of manganites with active spin–charge–orbital degrees of freedoms, the competing phases closely related to the CMR physics are the ferromagnetic–metallic, the charge–orbital ordered antiferromagnetic–insulating and the uniformly orbital-ordered antiferromagnetic metallic states, etc, as detailed in the next section.
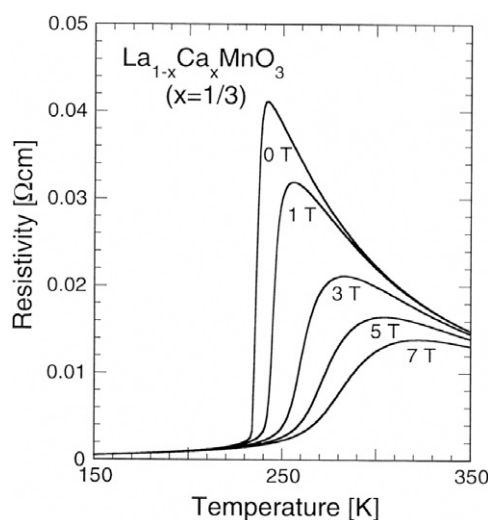
Figure 1. Colossal magnetoresistance (CMR) behaviour for the $La_{0.67}Ca_{0.33}MnO_3$ single crystal.

In such a strongly electron-correlated and/or electron–lattice-coupled system as the perovskite manganites, there are two important electronic parameters: the band filling (or doping level) and the one-electron bandwidth (or electron hopping interaction), both of which can be controlled to a considerable extent by modifying the chemical composition of the perovskite. Both parameters control the kinetic energy of the conduction electrons which governs the competition among the different electronic phases. We will see ample examples of the chemical control of these electronically important parameters to bring the compound to the bicritical or multicritical region under the phase competition.

The format of this paper is as follows: in section 2, we first give an overview of the spin–charge–orbital phase diagrams in the plane of hole-doping (band-filling) and temperature, as realized in several perovskite-type manganites with various one-electron bandwidths. The prescription for controlling the one-electron bandwidth and band filling is given there with use of the perovskite structure. In addition to the staggered orbital ordering at the end of the (undoped) Mn^{3+}-based compound, the hole-doped manganites show a variety of orbital ordered or disordered structures, which totally govern the sign and magnitude of spin exchange interactions. Some low-dimensional ferromagnetic spin arrangements via the directional double-exchange interaction are highlighted. As the most important source of the CMR related charge insulation, the charge–orbital order accompanying the complex spin order (the so-called CE type) is described together with the magnetic field induced melting of the order.

Section 3 is devoted to the elucidation of the fundamental bicritical features due to the competition between the ferromagnetic-metallic and the charge–orbital ordered insulating phases. The bicritical phase diagram is, however, largely modified accompanying the loss of the long-range order region when the composition of the perovskite A-sites (mixed rare-earth and alkaline-earth ion sites) is changed even without change in the band filling and the averaged lattice structure, implying the extreme sensitivity of the electronic state to the randomness near the bicritical region of the perovskite manganites. The electronic structure as investigated by optical spectroscopy for the manganite near the critical region (CMR regime) is also presented.

On the basis of the preceding results, we argue in section 4 on the important role of the quenched disorder, i.e. the temperature-independent disorder arising from chemical doping
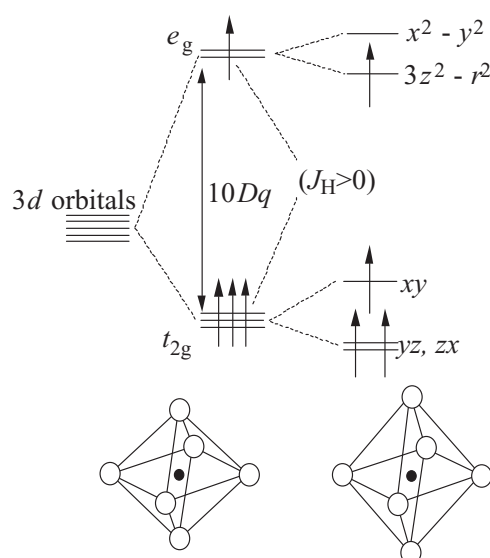
Figure 2. Crystal-field splitting of the five-fold degenerate atomic 3d levels into lower t_{2g} (triply degenerate) and higher e_g (doubly degenerate) levels. The Jahn–Teller distortion of the MnO_6 octahedron further lifts each degeneracy.

procedures near the bicritical region. To demonstrate this, we compare the phase diagrams between the cases with and without the quenched disorder by utilizing the A-site rare-earth and alkaline-earth ion ordered perovskites and their solid-solution (disordered) analogues. Then we show the global phase diagram for the phase-competing manganites in the parameter space of the magnitude of quenched disorder and the one-electron bandwidth at some fixed band-filling (doping level). When the quenched disorder is too strong, the compounds show the diffuse phase transition accompanying the history-dependent fraction of phase separation, which is to be termed the *magneto-electronic relaxor* in analogy with the ferroelectric relaxor. (The nomenclature '*relaxor*' had been originally coined to represent the material that shows a diffuse ferroelectric phase transition with frequency-dependent maximum temperature of huge dielectric response due to ferroelectric micro-embryos coexistent with the paraelectric state.) The underlying physics for the disorder-induced modification of the electronic phase, which accompanies the emergence of the CMR state, is argued in the light of recent advances in theoretical studies. In section 5 the summary and final remarks for the more generalized scheme for phase control are described.

2. Spin–charge–orbital phase diagrams

2.1. Fundamental electronic and lattice features in manganites

Each manganese (Mn) ion in the perovskite is surrounded by an oxygen octahedron. The 3d orbitals on the Mn-site placed in such an octahedral coordination are subject to the partial lifting of the degeneracy into the lower-lying t_{2g} states and the higher-lying e_g states [19]. In the Mn^{3+}-based compounds, the Mn site shows the electronic configuration of $t_{2g}^3 e_g^1$ (total spin number $S = 2$, figure 2). The t_{2g} electrons, less hybridized with O 2p states and more stabilized by the crystal field splitting, are viewed as always localized by the strong correlation effect and as forming the local spin ($S = 3/2$) even in the metallic state with the e_g electrons as the charge

carriers. The e_g electrons become localized when the hopping interaction is relatively small. The cause of the e_g electron localization is two-fold: one is electron correlation such as the t_{2g} electron, even though the e_g states are more strongly hybridized with the O 2p states. This correlation effect would by itself lead only to the Mott insulating state unless carrier-doped. The other is the Jahn–Teller coupling of the e_g electron with the surrounding oxygen displacement. The Jahn–Teller coupling lifts the degeneracy of the e_g orbital by causing the deformation of the MnO_6 [20]. The most frequently observed deformation of the nearly cubic (e.g. perovskite) lattice is, for example, the elongation of the z-axis (apical) oxygen position coupled with the occupied $3z^2$–r^2 orbital, or the elongation of the x and y-axes (in-plane) oxygen positions coupled with the occupied x^2–y^2 orbital. When the e_g band filling is close to 1 (or otherwise to some commensurate value), the individual Jahn–Teller distortions are cooperatively induced, leading to symmetry lowering of the lattice form or a new superstructure. Thus, the obital ordering in the manganites is always associated with the cooperative Jahn–Teller distortion. When electron vacancies or holes are created in the e_g orbital states of the crystal and escape from the long-range ordering, the e_g electrons can be itinerant and hence play the role of conduction electron. The latter hole-doping procedure corresponds to the creation of mobile Mn^{4+} species on the Mn sites.

The important consequence of the apparent separation into the local-spin and charge sectors in the 3d orbital electron is the effective strong coupling between the e_g conduction electron spin ($S = 1/2$) and the t_{2g} electron local spin ($S = 3/2$). This on-site ferromagnetic coupling follows Hund's rule. The exchange energy J_H (Hund's-rule coupling energy) is as large as 2–3 eV for the manganites and exceeds the intersite hopping interaction t of the e_g electron between the neighbouring sites, i and j. In the case of the strong coupling limit with $J_H/t \to \infty$, the effective hopping interaction t_{ij} of the conduction electron can be expressed in terms of the Anderson–Hasegawa relation [5],

$$
\begin{aligned}
t_{ij} &= t[\cos(\theta_i/2)\cos(\theta_j/2) + e^i(\phi_i - \phi_j)\sin(\theta_i/2)\sin(\theta_j/2)] \\
&= t\cos(\theta_{ij}/2)\exp(i\alpha_{ij}).
\end{aligned}
\tag{1}
$$

Here, θ_i and ϕ_i are polar and azimuth angles, respectively, of the spin on the site i. Neglecting the phase factor $\exp(i\alpha_{ij})$, the absolute magnitude of the effective hopping depends on the relative angle (θ_{ij}) between the neighbouring (classical) spins. The ferromagnetic interaction via the exchange of the (conduction) electron is termed the double-exchange interaction by Zener [4]. The phase factor $\exp(i\alpha)$ contributes to the Berry phase gained by the hopping electron around the atomic placket or loop. The Berry phase in the present context stands for the phase factor of electron hopping in its quantum-mechanical amplitude and depends on the spin chirality $S_1 \cdot (S_2 \times S_3)$, namely, the solid angle subtended by three spins on the respective sites where the electron is hopping. In the CMR phenomena of the manganites, the Berry phase appears to play a minor role in spite of the early theoretical anticipation [21]. However, the anomalous Hall effect observed around the ferromagnetic transition temperature T_C has been assigned as originating from this effect [22, 23]. More obvious observations and discussion on the role of the Berry phase in the anomalous Hall effect have been argued in the ferromagnetic state with the umbrella spin structure on the pyrochlore lattice in $Nd_2Mo_2O_7$ [24].

By creating electron-vacancy sites (or hole-doping) the e_g electron can hop depending on the relative configuration of the local spins. The ferromagnetic metallic state ($\theta_{ij} = 0$) is stabilized by maximizing the kinetic energy of the conduction electrons. When the temperature is raised to near or above the ferromagnetic transition temperature (T_C), the configuration of the spin is dynamically disordered and accordingly the effective hopping interaction is also subject to disorder and is reduced on average. This would lead to enhancement of the resistivity near and above T_C. Therefore, the large MR can be expected around T_C, since the local spins
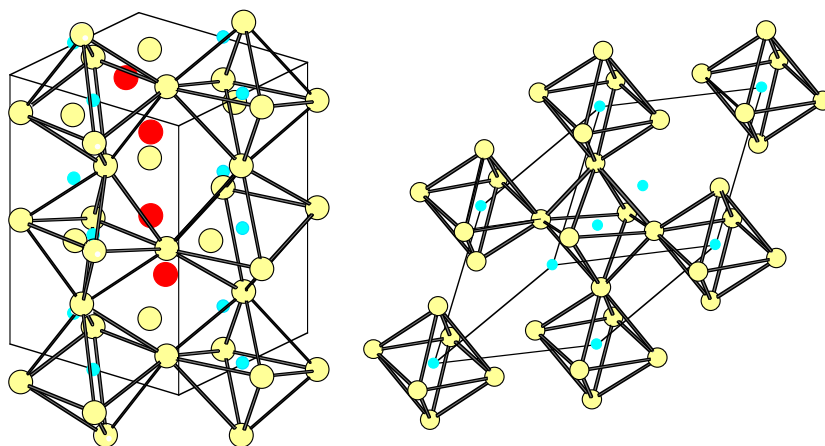
Figure 3. Structures of distorted perovskites of manganite: orthorhombic (left) and rhombohedral (right).

are relatively easily aligned by an external field and hence the randomness of the e_g hopping interaction is reduced. This is the intuitive explanation of the MR observed for the manganite around T_C in terms of the double-exchange (DE) model, as realistically demonstrated for the case of $La_{1-x}Sr_xMnO_3$ ($x \sim 0.3$) with the maximal one-electron bandwidth in terms of the dynamical mean-field treatment [11, 25]. The physics of CMR is, however, obviously more complex and abundant. There are certainly other important factors than in the above simplest DE scenario, which are necessary to interpret important features observed experimentally as first pointed out by Millis *et al* [26]. These are, for example, electron–lattice interaction (dominantly of the Jahn–Teller type), ferromagnetic/antiferromagnetic super-exchange interaction between the local spins, intersite exchange interaction between the e_g orbitals (orbital ordering tendency) and intrasite and intersite Coulomb repulsion interactions among the e_g electrons. These interactions/instabilities occasionally compete with the ferromagnetic DE interaction, producing complex electronic phases as well as gigantic responses of the system to external stimuli, such as CMR or the field-induced insulator–metal transition. Throughout this review paper, we will focus on the competition among the electronic phases, typically between the ferromagnetic metallic (FM) state and the charge–orbital ordered (CO/OO) states with the collectively Jahn–Teller coupled lattice deformations.

Most of the CMR phenomena have been found and investigated so far for the manganese oxide (manganite) compounds with the perovskite-type structure (figure 3). The perovskite-type magnanites have the general formulae, $RE_{1-x}AE_xMnO_3$, where RE stands for the trivalent rare earth elements such as La, Pr, Nd, Sm, Eu, Gd, Ho, Tb, Y etc, or for Bi^{3+} and AE for the divalent alkaline earth ions such as Sr, Ca and Ba or for Pb^{2+}. The (RE, AE) site (the so-called perovskite A-site) can in most cases form a homogeneous solid solution. Perovskite-based structures occasionally show lattice distortion as modifications from the cubic structure. One of the possible origins of the lattice distortion is the deformation of the MnO_6 octahedron arising from the Jahn–Teller effect which is inherent to the high-spin ($S = 2$) Mn^{3+} with a double degeneracy of the e_g orbital. Another lattice deformation comes from the connecting pattern of the MnO_6 octahedra in the perovskite structure, forming a rhombohedral or orthorhombic (the so-called $GdFeO_3$ type) lattice, as shown in figure 3. In these distorted perovskites, the MnO_6 octahedra show alternating buckling. Such a lattice distortion of the perovskite in the form of ABO_3 (here $A = RE_{1-x}AE_x$ and $B = Mn$ for the present manganites) is governed by

Table 1. Ionic radii (in ångstroms) for elements involved in the perovskite structure of manganite. Cited mostly from the values tabulated by Shannon [28]. The perovskite A-site is coordinated by 12 O_2^- ions. Some values of 12-coordination rare-earth 3+ ions are missing in Shannon's table and are inferred here from the respective 9-coordination values.

Ca^{2+}	Sr^{2+}	Ba^{2+}	Mn^{3+}	Mn^{4+}	O^{2-}		
1.34	1.44	1.61	0.645	0.530	1.40		
La^{3+}	Pr^{3+}	Nd^{3+}	Sm^{3+}	Eu^{3+}	Gd^{3+}	Tb^{3+}	Ho^{3+}	Y^{3+}
1.36	1.29	1.27	1.24	1.23	1.21	1.20	1.18	1.18

the so-called tolerance factor f [27], which is defined as

$$f = (r_B + r_O)/\sqrt{2}(r_A + r_O). \tag{2}$$

Here, r_i ($i = A$, B or O) represents the (averaged) ionic size of each element. (The ionic radii for the respective elements in the perovskite-like structure are listed in table 1.) The tolerance factor f measures, by definition, the lattice-matching of the sequential AO and BO_2 planes. When f is close to 1, the cubic perovskite structure is realized. As r_A or equivalently f decreases, the lattice structure transforms to the rhombohedral ($0.96 < f < 1$) and then to the orthorhombic (the so-called $GdFeO_3$ type) structure ($f < 0.96$), in which the B–O–B bond angle (θ) is bent and deviates from $180°$. In the case of the orthorhombic lattice, the bond angle θ varies continuously with f, as exemplified for the case of the $GdFeO_3$-type $REFeO_3$ and $RETiO_3$ [29]. The relation between the bond angle distortion and the tolerance factor f shows little B-site dependence, and hence is likely to be applicable to doped manganites with $GdFeO_3$-type orthorhombic distortion.

The bond angle distortion decreases the one-electron bandwidth W (being proportional to t), since the effective d electron transfer interaction t between the neighbouring B-sites is governed by the super-transfer process via O 2p states. For example, let us consider the hybridization between the 3d e_g state and the 2p σ state in the $GdFeO_3$ type lattice which is composed of the quasi-right octahedra of BO_6 tilting alternately. In the strong ligand field approximation, the p–d transfer interaction t_{pd} is expressed as

$$t_{pd} \approx t_{pd}^0 |\cos\theta|, \tag{3}$$

t_{pd}^0 being for the hypothetical cubic perovskite. Thus, the effective d-d hopping interaction t or the W for the e_g electron state is approximately proportional to t_{pd}^2 and hence to $\cos^2\theta$. In other words, when the compound shows a structural variation in a relatively narrow f-range, W is almost directly proportional to the f-value. This is the reason for the f-value or the ionic radius r_A of the A-site often being used as the abscissa to represent the electronic phase diagram of the perovskite transition-metal oxide with strong electron correlation [29, 30], including the case of perovskite manganites [31].

Another important feature in the perovskite is that the compound is quite suitable for the carrier doping procedure (filling control) since the structure is very robust against the chemical modification on the A-site such as the solid solution of the divalent (alkaline-earth) and trivalent (rare-earth) ions. For example, in $La_{1-x}Ca_xMnO_3$, the solid solution can extend from $x = 0$ to 1. For AE = Sr the x can be extended up to $x = 0.7$ under normal synthetic conditions, but up to $x = 1$ under high pressures or in the form of an epitaxial thin film. In the formula unit of $RE_{1-x}AE_xMnO_3$, the averaged Mn valence varies as $3 + x$. Namely, x produces a vacancy in the e_g electron state at a rate of x per Mn-site and hence is referred to as hole-doping. To be exact, the filling (n) of the e_g electron conduction band is given as $n = 1 - x$.
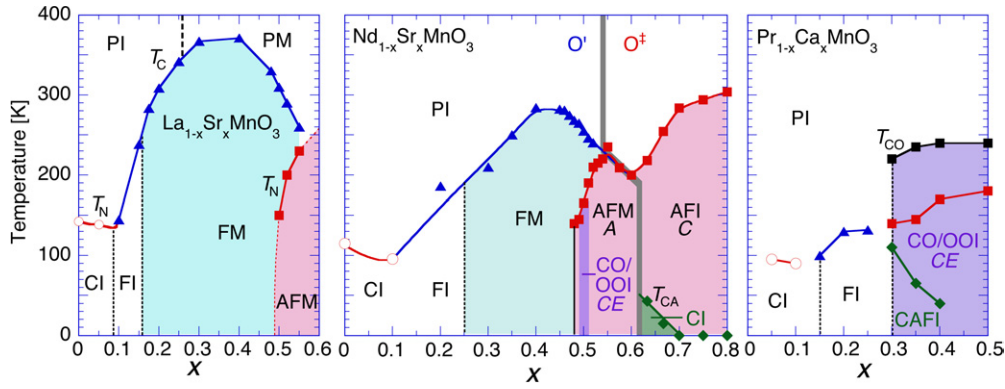
Figure 4. The magnetic as well as electronic phase diagrams of $La_{1-x}Sr_xMnO_3$ (*a*), $Nd_{1-x}Sr_xMnO_3$ (*b*) and $Pr_{1-x}Ca_xMnO_3$ (*c*). PI, PM and CI denote the paramagnetic insulating, paramagnetic metallic and spin-canted insulating states, respectively. FI, FM and AFM denote the ferromagnetic insulating and ferromagnetic metallic and antiferromagnetic (A-type) metallic states, respectively. At $x = 0.5$ in $Nd_{1-x}Sr_xMnO_3$, the charge–orbital ordered insulating (CO/I) phase with CE-type spin ordering is present. For $0.3 \leqslant x \leqslant 0.5$ in $Pr_{1-x}Ca_xMnO_3$, the antiferromagnetic insulating (AFI) state exists in the charge–orbital ordered insulating (CO/OOI) phase. The canted antiferromagnetic insulating (CAFI) state also shows up below the AFI state in the CO/OOI phase for $0.3 \leqslant x \leqslant 0.4$ (from [32]).

2.2. Orbital ordering and dimensional variation of double-exchange interaction

First, we show in figure 4 electronic phase diagrams in the temperature (T) versus hole concentration (x) plane for prototypical compounds [32]; (*a*) $La_{1-x}Sr_xMnO_3$, (*b*) $Nd_{1-x}Sr_xMnO_3$ and (*c*) $Pr_{1-x}Ca_xMnO_3$. As the tolerance factor or equivalently the averaged ionic radius of the perovskite A-site decreases from (La, Sr) to (Pr, Ca) through (Nd, Sr), the orthorhombic distortion of $GdFeO_3$-type increases, resulting in a decrease in the one-electron bandwidth (W) of the e_g-state carriers. This means that other electronic instabilities, such as the charge/orbital-ordering and super-exchange interactions which compete with the DE interaction, may become dominant in specific regions of x and temperature.

Let us begin with the phase diagram for $La_{1-x}Sr_xMnO_3$ with maximal W. The end compound $LaMnO_3$ ($x = 0$) as well as other $REMnO_3$ are strongly affected by both the collective Jahn–Teller effect and the electron correlation effect due to the $n = 1$ filling of the e_g band. The collective Jahn–Teller distortion present in $LaMnO_3$ reflects the orbital ordering such as the alternating $d_{3x^2-r^2}$ and $d_{3y^2-r^2}$ orbitals on the *ab* plane [20, 33]. (Here, the *x* and *y* axes are taken as along the orthogonal Mn–O bond directions on the *ab* plane.) In this Jahn–Teller-distorted and orbital-ordered state, the $LaMnO_3$ undergoes an antiferromagnetic transition at $T_N = 120$ K, which is much lower than the orbital ordering temperature (780 K) [33]. The spin ordering structure is the layered type or the so-called A-type, in which the ferromagnetic *ab* plane is coupled antiferromagnetically along the *c*-axis. In the $GdFeO_3$ type lattice, however, the Dzyaloshinsky–Moriya interaction causes the canting of the spins towards the *c*-axis, and hence produces the weak ferromagnetism below T_N. Incidentally, the highly distorted $REMnO_3$ with RE = Tb and Dy shows magnetic frustration because of the competition between the nearest-neighbour ferromagnetic and the next-nearest-neighbour antiferromagnetic interactions [34], which result in the long-period (4–8 a_0, $a_0 \sim 0.4$ nm being the cubic perovskite primitive cell) modulation of the spin structure. It has recently been demonstrated that the ground state of these materials shows the ferroelectric state [35], which is supposed to be tied to the specific (e.g. spiral) spin structures.

With hole-doping by substitution of La with Sr, the ordered spins are more canted towards the c-axis direction. In the pioneering paper by Wollan and Koehler [36] for $La_{1-x}Ca_xMnO_3$, they argued on the spin state in such a lightly doped region in terms of the mixture of the ferromagnetic and antiferromagnetic domains. Later, however, de Gennes [6] reinterpreted that the extension of the wavefunction of the hole along the c-axis can mediate the DE-type ferromagnetic coupling, producing the spin canting. As the doping level x increases typically above 0.1, the spin state is turned into a ferromagnetic one, while the compound remains insulating or semiconducting up to the critical doping for the metal–insulator transition, e.g. $x = 0.17$ in $La_{1-x}Sr_xMnO_3$ [37, 38]. Another important consequence of hole-doping is that the static collective Jahn–Teller distortion present in $LaMnO_3$ is diminished with increase in the doping level, perhaps beyond $x = 0.10$. This is manifested by the structural transformation between two types of orthorhombic forms [39]. The nature of the ferromagnetic but insulating state for $0.1 < x < 0.17$ in $La_{1-x}Sr_xMnO_3$, and perhaps up to $x \sim 0.3$ for other narrower-W manganites (e.g. $Pr_{1-x}Ca_xMnO_3$), is still puzzling and under investigation. The implication of the charge and/or orbital ordered state has been obtained by (resonant) x-ray scattering [40,41] and neutron scattering [42]. Now it is generally believed that the origin of the ferromagnetism is due to the ferromagnetic super-exchange interaction, not to the double-exchange interaction, in the orbitally active state. Several models for the orbital ordering, in which the super-exchange interaction can produce the nearly isotropic ferromagnetic interaction, have been suggested for this insulating ferromagnetic region [41–44].

With doping above $x = 0.17$, the ferromagnetic metallic phase appears below T_C which steeply increases with x up to 0.3 and then saturates. In the ferromagnetic metallic phase, there is no trace of orbital order. With further hole-doping above $x = 0.5$, however, the metallic but antiferromagnetic (AF) phase appears [32, 45, 46]. The AF phase above $x = 0.5$ is the A-type (layered type) but its orbital feature is distinct from that of $x = 0$: the metallic or the quasi-metallic A-type AF state is accompanied by a uniform ordering of the x^2–y^2 orbital state. Namely, the quasi-two-dimensional, fully spin-polarized, metallic x^2–y^2 electron band is formed due to the double-exchange interaction, while the ferromagnetic sheet is coupled antiferromagnetically along the c axis mainly due to the super-exchange interaction of the t_{2g} electron spins. This (quasi-)metallic x^2–y^2 orbital-ordered state is ubiquitous in the over-doped ($x = 0.5$–0.6) manganites with relatively large W, e.g. $Pr_{1-x}Sr_xMnO_3$ [47] and $Nd_{1-x}Sr_xMnO_3$ [46, 48, 49], which is free from the long-range charge ordering.

The decrease in W complicates the phase diagram. In particular, when the doping x is close to the commensurate value $x = 1/2$, the charge-ordering instability comes to the surface. In the case of $Nd_{1-x}Sr_xMnO_3$ (figure 4(b)), the ferromagnetic metallic (FM) phase shows up for $x > 0.3$, yet in the immediate vicinity of $x = 1/2$ the FM state changes into the charge-ordered and orbital-ordered insulating (CO/OOI) state with the decrease in temperature below $T_{CO} = 160$ K [50]. This CO/OOI state accompanies the concomitant antiferromagnetic ordering of spins, which is called the CE type [36, 51–53], as shown in figure 5. The nominal Mn^{3+} and Mn^{4+} species with a 1 : 1 ratio show real-space ordering on the (001) plane of the orthorhombic lattice (P_{bnm}), while the e_g orbital shows the 1×2 superlattice on the same (001) plane. Reflecting such an orbital ordering, the ordered spins form a complicated sublattice structure extending over a larger unit cell as shown in the figure. Although a similar concomitant charge and spin ordering is widely seen in $3d$ electron transition metal oxides [29], the most notable feature of the manganites is the magnetic field-induced melting of the CO/OOI state, which shows up as the field-induced phase transition from an antiferromagnetic insulator to a ferromagnetic metal.

With the hole concentration of $x > 0.52$, the A-type (layered type) AF ordering turns up again in $Nd_{1-x}Sr_xMnO_3$ [46–49]. The uniform ordering of x^2–y^2 orbitals makes the phase
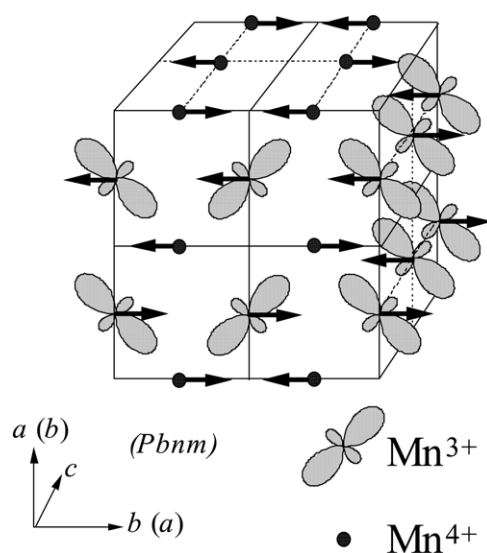
Figure 5. Spin, charge and e_g orbital ordering pattern of the CE type observed for most of the $x \approx 1/2$ manganites. Lobes on the nominal Mn^{3+} sites represent the e_g orbital. The Mn^{4+} sites are indicated by closed circles.

metallic but highly 2D-like ($\sigma_{ab}/\sigma_c \approx 10^4$ at 35 mK) [48], since the inter-plane (c-axis) hopping of the fully spin-polarized $d_{x^2-y^2}$ electron is almost forbidden due to the in-plane confinement in the layered-AF structure as well as to the minimal supertransfer interaction between the x^2-y^2 orbitals along the z-direction. As x is further increased, the rod type (C-type) AF ordering turns up at $x > 0.62$ (figure 4(b)). Considering the elongation of the lattice parameter along the c-axis, the $3z^2-r^2$ orbitals are mostly occupied in the C-type AF phase. This is another form of reduced-dimensional ferromagnetism stabilized by the double-exchange interaction. The mean-field theory for the electronic phase diagram of pseudo-cubic manganites also predicts that the hole-doping drives the electronic phase from the isotropic ferromagnetic state to the layered A-type AF state with the x^2-y^2 orbital order and further to the chain-like C-type AF state with the $3z^2-r^2$ orbital order [54]. The successive magnetic phase change is qualitatively interpreted as follows: on decreasing the filling of the e_g electrons which can mediate the ferromagnetic double-exchange interaction, the compound reduces the dimension of the ferromagnetic form while increasing the number of antiferromagnetic super-exchange interaction paths, namely, 3D for $0.2 < x < 0.5$, 2D for $0.5 < x < 0.6$ and 1D for $0.6 < x < 0.8$. These features at the ground state are schematically summarized in figure 6 [55, 56].

When the bandwidth is reduced with the decrease in the tolerance factor, the sequential A–F–A–C transformation of the long-range magnetic order with hole-doping is violated by the presence of the subsistence of the charge–orbital order (the CE-type spin order), as shown in the ground-state phase diagram (figure 6). In the figure, the notation $C_x E_{1-x}$ for the $x > 0.5$ region represents the incommensurate charge–orbital–spin order where the orbital ordering shows the q-vector $((1-x)/2, (1-x)/2, 0)$ in the cubic setting. (Namely, the separation between the neighbouring orbital stripes along [110] expands with x.) We show the phase diagram for $Pr_{1-x}Ca_xMnO_3$ in figure 4(c) as a typical example of this case, which is discussed in detail in the next section.

Here, it is useful to see the anisotropic electronic structures of the three representative double-exchange (DE) states with varying dimension, namely, the FM with orbital disorder
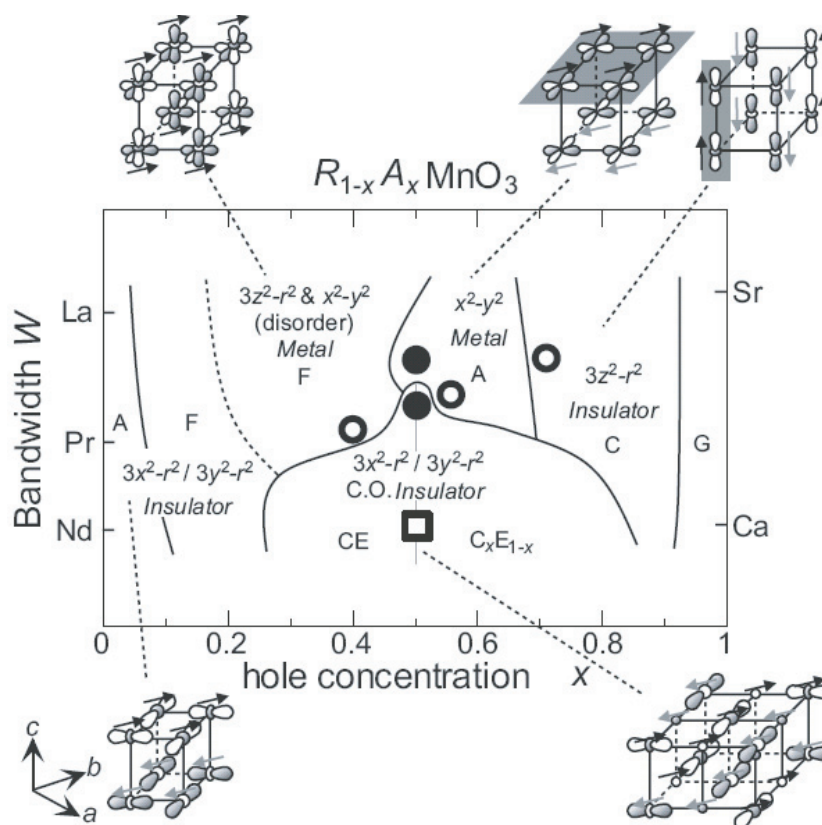
Figure 6. Bandwidth versus hole concentration phase diagram at the ground state of $RE_xAE_xMnO_3$. F denotes a ferromagnetic state. A, CE, C and G denote A-type, CE-type, C-type and G-type antiferromagnetic states, respectively. Illustrations show schematic views of the orbital and spin configurations on Mn sites for the respective phases. The arrows represent the direction of spin, and the lobes show the e_g orbital (from [55, 56]).

(quantum melting), the A-type AFM with $x^2–y^2$ orbital order (OO), and the C-type AFI with $3z^2–r^2$ OO. For this, we exemplify in figure 7 the ground-state (10 K) optical conductivity $\sigma(\omega)$ spectra of $Nd_{1-x}Sr_xMnO_3$ ($x = 0.4, 0.55$ and 0.7) with controlled band fillings (doping levels) [56]. The ferromagnetic spin arrangement with spatial extent of 3D ($x = 0.4$), 2D ($x = 0.55$) and 1D ($x = 0.7$) in $Nd_{1-x}Sr_xMnO_3$ is all due to the DE interaction. In the figure, solid and dashed lines denote the $\sigma(\omega)$ spectra with the light polarization E parallel [$\sigma_\parallel(\omega)$] and perpendicular [$\sigma_\perp(\omega)$] to the ferromagnetically-coupled Mn sites (see and compare the right insets). For $x = 0.4$ with the ferromagnetic-metallic orbital-disordered state, the $\sigma(\omega)$ forms a Drude-like peak, which reflects the coherent motion of charge carriers. (Here we have used the term 'Drude-like' for the shape of $\sigma(\omega)$ with a peak centred at $\omega = 0$, although the whole infrared spectral shape of the $x = 0.4$ compound, whose broad tail of conductivity persists up to ~ 1 eV, cannot be described with the conventional Drude form alone [57, 58].) In the $x = 0.55$ and 0.7 crystals, $\sigma(\omega)$ spectra show a remarkable polarization dependence, reflecting the highly anisotropic electronic structure in the spin and orbital ordered state, as illustrated in the right insets in figure 7. The details of T-dependence of the spectral anisotropy for $x = 0.55$ and 0.7 have been reported to probe the T-dependent orbital ordering [59]. It is worth noting the evolution of the gap structure with reducing dimensionality of the DE interaction; from the
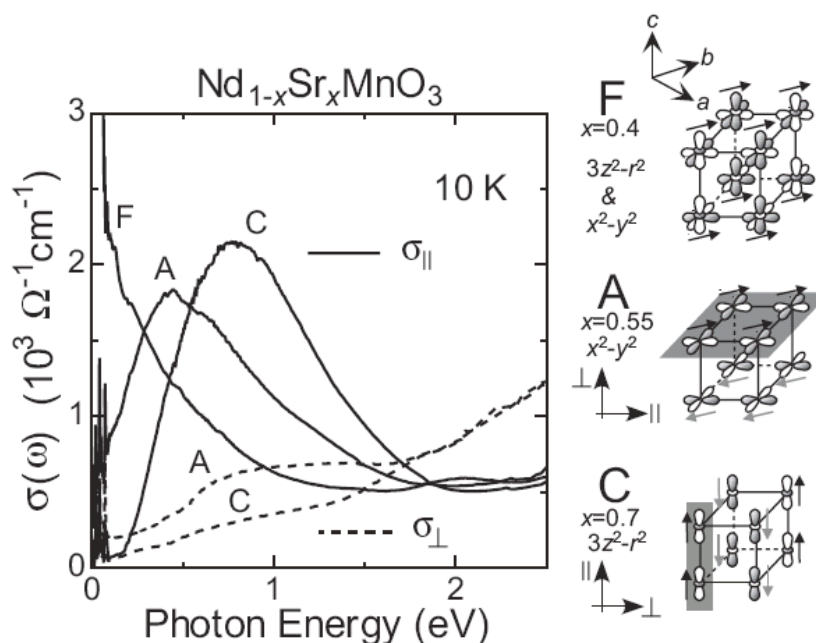
Figure 7. Polarization dependence of the optical conductivity spectra at 10 K for $x = 0.4$, 0.55 and 0.7 crystals of $Nd_{1-x}Sr_xMnO_3$. Illustrations show schematic views of the orbital and spin configurations as well as the relations between the light polarizations ($\parallel$ and $\perp$) and the ordering structures (from [56]).

Drude-like coherent peak for $x = 0.4$ to a *pseudo*-gap for $x = 0.55$ and then to a *real* gap for $x = 0.7$. (Here, the pseudo-gap means the peaked spectral feature with a remaining $\sigma(\omega = 0)$ value but with no Drude-like peak). This signals extremely diffuse charge dynamics within the ferromagnetic 2D sheets and 1D chains.

2.3. Charge–orbital ordering and electronic structure

In the most frequently observed charge and orbital ordering (CO–OO) pattern in the near half-doped ($x \sim 0.5$) manganites as shown in figure 5, the $3x^2$–r^2 and $3y^2$–r^2 orbitals, respectively, form the stripes along the diagonal of the Mn-square lattice. Such an orbital ordering pattern, at least within the *ab* plane, is ubiquitous in all the nearly half-doped compounds including single- or bi-layered manganites and the A-site cation ordered manganites (see section 3.2). Recent soft x-ray spectroscopic studies [61,62], however, favour the orbital ordering of x^2–z^2 and y^2–z^2 type orbitals, rather than the $3x^2$–r^2 and $3y^2$–r^2 type, for the $La_{0.5}Sr_{1.5}MnO_4$ ($x = 0.5$) with a single-layer structure, while the spatial symmetry is the same. The degree of the orbital mixing, e.g. between the $3x^2$–r^2 and x^2–z^2, may vary depending on the crystal structure and/or the local configuration of the MnO_6 octahedra, yet either of the orbital orders can similarly mediate the ferromagnetic double-exchange interaction along the in-plane lobe direction of the ordered orbital and hence realize the so-called CE type spin order, as shown in figure 5, at the ground state. Most of the $x = 0.5$ compounds undergo long-range charge–orbital ordering at higher temperature than the long-range CE type spin ordering. In the case where the ferromagnetic metallic phase is present at temperatures above the CO–OO phase as in $Nd_{0.5}Sr_{0.5}MnO_3$, the transition from the ferromagnetic metallic phase is accompanied by simultaneous long-range order in the charge, orbital and spin sectors [50].
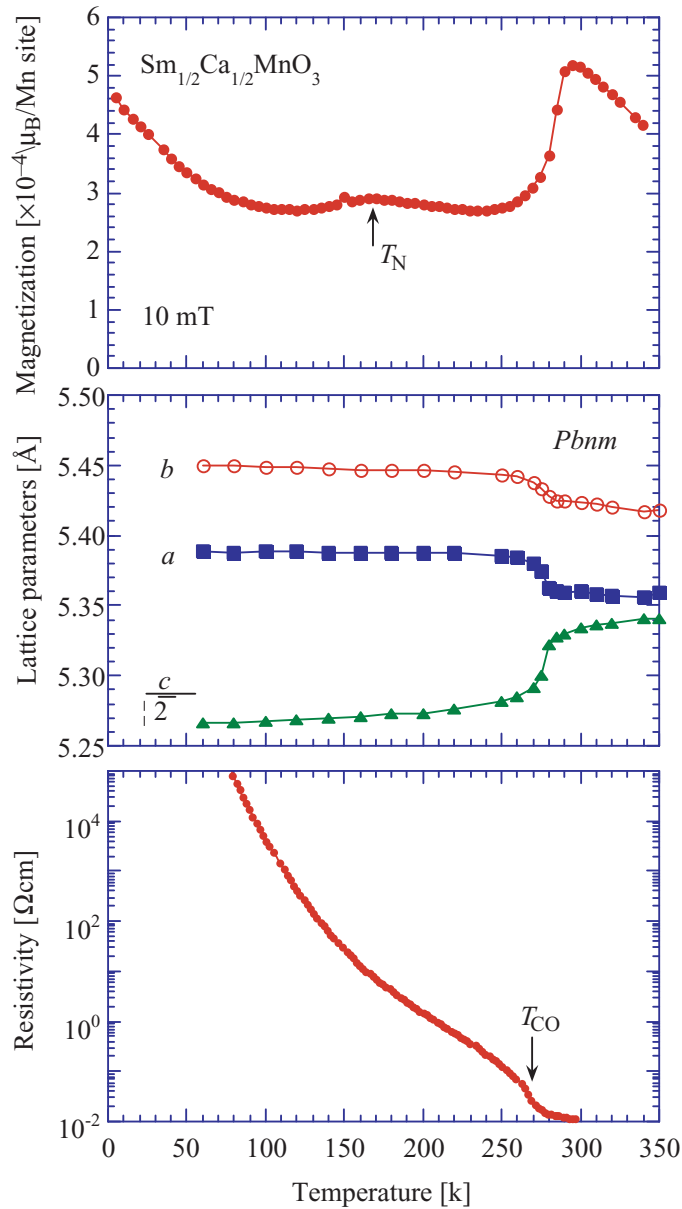
Figure 8. Temperature dependences of magnetization (top), resistivity (middle) and lattice parameters (bottom) observed for $Sm_{1/2}Ca_{1/2}MnO_3$. In $Sm_{1/2}Ca_{1/2}MnO_3$ the critical temperature of the charge/orbital ordering transition ($T_{CO} \approx 270$ K) is higher than the antiferromagnetic Nèel temperature ($T_N \approx 170$ K) (from [32]).

In figure 8 a typical example of the CO/OO transition observed for $Sm_{1-x}Ca_xMnO_3$ ($x = 0.5$) [32] is shown. (The observed features are quite similar also in $Pr_{0.5}Ca_{0.5}MnO_3$ and $Nd_{0.5}Ca_{0.5}MnO_3$, apart from a slight variation of the CO/OO transition temperature.) As shown in the temperature dependences of resistivity and magnetization, the CO/OO transition manifests itself as a decrease in magnetization and increase in resistivity, which locates at
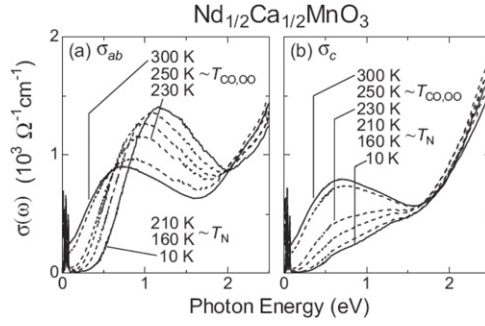
Figure 9. Temperature dependence of the optical conductivity spectra of $Nd_{1/2}Ca_{1/2}MnO_3$ for $E\|ab$ (σ_{ab}) and $E\|c$(σ_c) polarizations (from [56]).

$T_{CO} \approx 270$ K. Changes in lattice parameters are also observed at T_{CO}; elongation in the orthorhombic a and b axes and contraction in the c axis, suggesting that concomitant ordering of the e_g-orbital, as shown in figure 5, occurs simultaneously. As is clear from the temperature dependence of magnetization, however, the antiferromagnetic spin-ordering does not occur concurrently but at a lower temperature, $T_N \approx 170$ K, and no ferromagnetic state is present at zero field. In the reduced-bandwidth (W) systems, such as $RE_{1/2}Ca_{1/2}MnO_3$ (RE = Pr, Nd, Sm, . . .), in which no ferromagnetic or metallic state is realized, a split between T_{CO} and T_N is generally observed. A similar feature is also observed for the related materials with the layered-perovskite structure, $La_{1-x}Sr_{1+x}MnO_4$ ($x = 1/2$), where $T_{CO} \approx 217$ K and $T_N \approx 110$ K [63].

We show in figure 9 the temperature (T) dependence of the optical conductivity spectra for $Nd_{0.5}Ca_{0.5}MnO_3$ [56] as the example showing the CO/OO transition. First, let us see the optical spectra at the ground state, e.g. at 10 K. The $\sigma(\omega)$ spectra below ≈ 2 eV show huge anisotropy with respect to the light polarization E parallel and perpendicular to the c axis, reflecting the highly anisotropic electronic structure in the charge–orbital and CE-type AF ordered state. The $\sigma_{ab}(\omega)$ spectrum shows a prominent peak around ≈ 1 eV, forming a gap (≈ 0.4 eV) structure, whereas the $\sigma_c(\omega)$ spectrum has little spectral weight around ≈ 1 eV. With the increase in T, the peak structure is gradually suppressed and shifted to the lower energy region. The gap structure, which is present in the low-T $\sigma_{ab}(\omega)$ spectra, gradually diminishes at high T, while persistently forming a pseudo-gap structure with a non-zero $\sigma_{ab}(\omega = 0)$ value. As for the $\sigma_c(\omega)$ spectra, in contrast, the low-energy (<1.5 eV) spectral weight, which is suppressed at low T, tends to increase with the increase in T. At T_{CO}, the spectra show a nearly polarization-independent shape with a broad peak around ≈ 0.7 eV. It is noteworthy that an abrupt spectral change from the pseudo-gap to the real-gap like structure is discernible in figure 9 at T_{CO}, while no remarkable change in the spectra takes place around T_N.

To evaluate the T-dependence of the spectral weight, the effective number of electrons $N_{eff}(\omega)$ as defined by the following relation,

$$N_{eff}(\omega) = \frac{2m}{\pi e^2 N} \int_0^\omega \sigma(\omega') \, d\omega', \tag{4}$$

can be used. Here, N represents the number of formula units (i.e. the number of Mn atoms per unit volume). We plot the $N_{eff}[ab]$ and $N_{eff}[c]$ values in figure 10(b) as a function of T, adopting a cut-off energy at $\hbar\omega = 2.0$ eV, below which most of the T-dependent spectral change occurs. At 10 K, $N_{eff}[ab]$ is more than twice as large as the $N_{eff}[c]$, showing a clear anisotropic feature. In the mid-T region, $T_N < T < T_{CO}$, the $N_{eff}[ab]$ decreases while the $N_{eff}[c]$ increases with

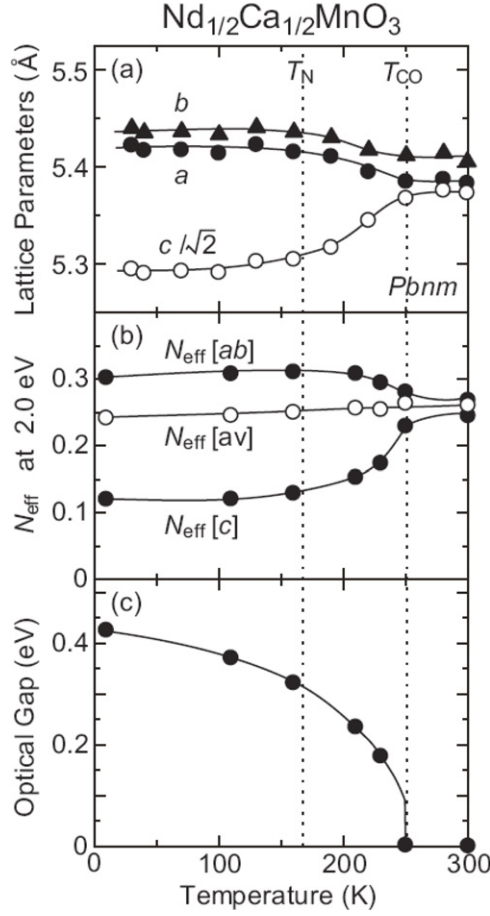**Figure 10.** (a) Temperature dependence of the lattice parameters of $Nd_{1/2}Ca_{1/2}MnO_3$, (b) temperature dependence of the effective number of electrons N_{eff} for the $E\|ab$ and $E\|c$ polarizations which are deduced by integrating the observed $\sigma(\omega)$ spectra over the region, $0\,eV < \hbar\omega < 2.0\,eV$, $N_{eff}[av]$ denotes the averaged spectral weight defined by $N_{eff} = (2N_{eff}[ab] + N_{eff}[c])/3$, and (c) temperature dependence of the optical gap magnitude as estimated by linearly extrapolating the rising part of the optical conductivity spectra for $E\|ab$. Solid lines are merely to guide the eyes (from [56]).

the increase in T, leading to a decrease in the anisotropy. The T dependence of the N_{eff} appears to be related to that of the lattice parameters (figure 10(a)) which is tied to the orbital state via the collective Jahn–Teller effect. This result clearly indicates the strong relationship between the spectral anisotropy and the formation of the orbital ordering. Figure 10(c) displays the T profile of the onset energy for the $\sigma_{ab}(\omega)$ spectrum as a measure of the optical gap energy. At the lowest T (10 K), the gap magnitude is approximately 0.4 eV, which gradually decreases as T is increased (e.g. 0.18 eV at 230 K) and is then suppressed abruptly to zero at T_{CO}. Thus, the onset of the long-range CE-type AF order scarcely induces the abrupt change in the anisotropic electronic structure below ∼2 eV and the gap magnitude, while the charge–orbital order plays a major role in determining them. In figure 10(b) the averaged spectral weight $N_{eff}[av] = (2N_{eff}[ab] + N_{eff}[c])/3$ at 2.0 eV is also shown, as a measure of the total spectral weight below ≈2 eV. In spite of the remarkable T-dependence in $\sigma_{ab}(\omega)$ and $\sigma_c(\omega)$, $N_{eff}[av]$

is nearly T-independent, indicating that the total kinetic energy measured on an energy scale of 2.0 eV is preserved during the charge–orbital order (and CE-type AF) transitions.

Several theoretical studies on the optical properties of the charge–orbital ordered manganites have been reported. Among them, Cuoco *et al* [60] studied the model for the CE phase, which includes on-site and intersite Coulomb interactions as well as the Jahn–Teller orbital polarization, by the exact diagonalization method. The optical excitation can be assigned to transitions between the correlated states of e_g electrons at Mn^{3+} sites, and the pseudo-gap feature in a high T region is reproduced as observed experimentally. The observed anisotropy of the $\sigma(\omega)$ spectra indicates that the kinetic energy of conduction electrons measured on this energy scale (2 eV) is suppressed for the component along the c-axis at the ground state. The peak structure in the $\sigma(\omega)$ spectrum can be assigned to the photo-induced hopping of the e_g electron between Mn^{3+} and Mn^{4+} sites, whose anisotropy can be interpreted in terms of (a) charge (b) orbital and (c) spin orders as follows: (a) the charge stacking along the c-axis prohibits the hopping to the c-direction by the strong on-site Coulomb repulsion, (b) the spectral weight depends on the electron transfer energy, and hence becomes anisotropic in the $3x^2–r^2/3y^2–r^2$-type orbital ordered state and (c) since the total spin quantum number is preserved during the optical excitation, intersite transitions along the c-axis between AF-coupled Mn sites should be forbidden by the large Hund's-rule coupling energy. All of them are relevant to the observed anisotropy in the optical spectra: the mechanisms (a) and (b) simultaneously work for the suppression of the c-polarized spectral weight since the charge and orbital orders occur concomitantly. The mechanism (c) is effective even in the case of short-range correlation and hence may be responsible as well for the anisotropic feature (figure 10(b)) even above T_N.

2.4. Magnetic field effects on charge–orbital ordering

Let us now turn to the magnetic field effects on the charge–orbital ordered (CO–OO) state in the near half-doped manganites with various one-electron bandwidths (W). Figure 11 shows the charge/orbital ordering phase diagrams for various $RE_{1/2} AE_{1/2}MnO_3$ ($x = 0.5$) crystals which are presented on the magnetic field–temperature ($H–T$) plane. The phase boundaries have been determined by measurements of the magnetic field dependence of resistivity ($\rho–H$) and magnetization ($M–H$) at fixed temperatures [50, 64], and those for $RE_{1/2}Ca_{1/2}MnO_3$ (RE = Pr, Nd and Sm) have been obtained by measurements utilizing pulsed high magnetic fields up to 70 T [65]. In this figure, the hatched area represents the magnetic-field hysteresis region accompanied by the first-order nature of the transition. The critical field to transform the CO–OO state to the ferromagnetic metallic (FM) state in $Nd_{1/2}Sr_{1/2}MnO_3$ is about 11 T at 4.2 K, while that in $Pr_{1/2}Ca_{1/2}MnO_3$ increases to about 27 T. In the case of $Sm_{1/2}Ca_{1/2}MnO_3$, the charge/orbital ordering is so robust that the critical field becomes as large as about 50 T at 4.2 K. Figure 11 thus demonstrates that the robustness of the charge/orbital ordering at $x = 1/2$ depends critically on the W controlled with the tolerance factor (or the averaged ionic radius of RE), which is understood in terms of a competition between the DE and CO–OO interactions.

To be further noted in figure 11 is the large hysteresis of the transition (hatched in the figure) which is characteristic of the first order phase transition coupled with the lattice degree of freedom. The change in lattice parameters originates from the field-destruction of orbital ordering. The hysteresis region (hatched area) expands with decreasing temperature especially below 20 K. In the case of the first order phase transition, the transition from the metastable to the stable state occurs by overcoming a free-energy barrier. Since the thermal energy decreases with lowering temperature, a larger (smaller) field than the thermodynamic value is needed to induce the transition from (to) the AF CO/OO to (from) the FM state. Thus
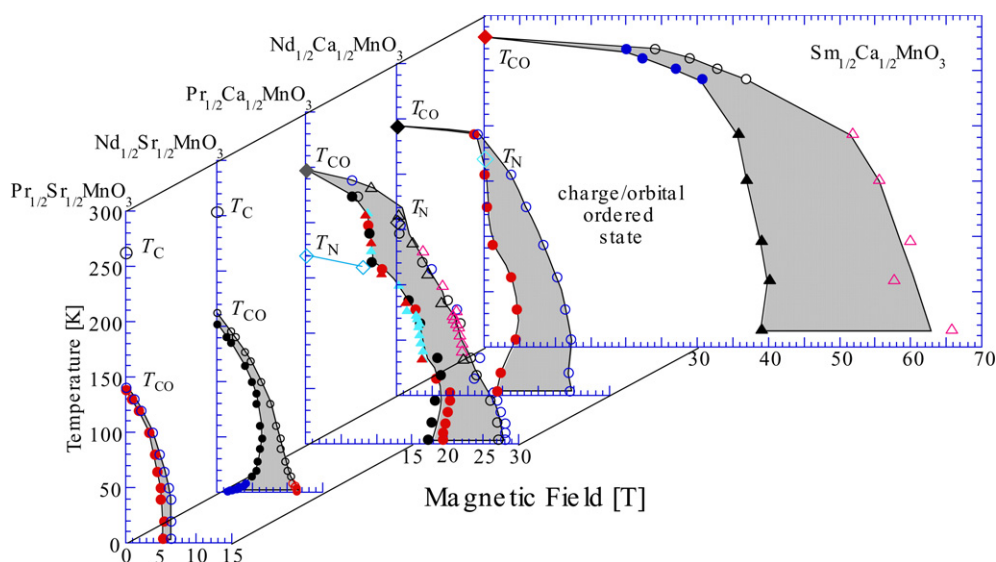
Figure 11. The charge/orbital-ordered phase of various $RE_{1/2}AE_{1/2}MnO_3$ plotted on the magnetic field–temperature plane. The phase boundaries have been determined by measurements of the magnetic field dependence of resistivity (ρ–H) and magnetization (M–H) at fixed temperatures [64, 65], and those for $RE_{1/2}Ca_{1/2}MnO_3$ (RE = Pr, Nd and Sm) have been obtained by measurements utilizing pulsed high magnetic fields up to 70 T (from [32]).

the hysteresis between the field increasing and decreasing runs increases with the decrease in temperature.

The incommensurate doping (i.e. the deviation of the hole doping level from $x = 1/2$) is also important for the relative stability of the CO/OO phase. The stability of the CO/OO state as a function of x is to be determined by the competition with other phases that are realized near the half-doping level ($x = 1/2$); the FM metallic state, the A-type spin-ordered and x^2–y^2-type orbital-ordered state and the C-type spin-ordered and $3z^2$–r^2-type orbital ordered state, as typically seen in the phase diagram of $Nd_{1-x}Sr_xMnO_3$ shown in figure 4(b). In $Nd_{1-x}Sr_xMnO_3$, the CO/OO state is thermodynamically not so stable as the $x \sim 0.5$ compounds of $RE_{1-x}Ca_xMnO_3$ with narrower W and hence emerges only in the immediate vicinity of $x = 0.5$. Thus, the CO/OO phenomena tend to be most stabilized when the band filling coincides with a rational number for the periodicity of the crystal lattice.

In perovskite manganites in which W is further reduced, such as $Pr_{1-x}Ca_xMnO_3$, the CO/OO state associated with the CE type spin order at low temperatures shows up in a much broader range of x [66]. We have already shown in figure 4(c) the electronic phase diagram of $Pr_{1-x}Ca_xMnO_3$ ($0 < x < 0.5$) [67] in which the FM metallic state is no longer realized at zero magnetic field and at ambient pressure. The ferromagnetic but insulating phase appears for $0.15 < x < 0.3$, perhaps accompanying some form of orbital ordering [44], mediating the ferromagnetic super-exchange interaction. With further increase in x, the CO/OO state with $1 : 1$ ordering of Mn^{3+}/Mn^{4+} appears for $x > 0.3$. As reported in an early neutron diffraction study [66], the charge–orbital ordering exists in a broad range of x ($0.3 < x < 0.75$), where the pattern of spin, charge and orbital ordering is basically described by that of $x = 0.5$. The coupling of spins along the c-axis is antiferromagnetic at $x = 0.5$, while the spin arrangement is not antiferromagnetic (or collinear) but canted for $x < 0.5$. Such a modified magnetic state in the underdoped ($x < 0.5$) region is called the pseudo-CE type. As the doping level deviates
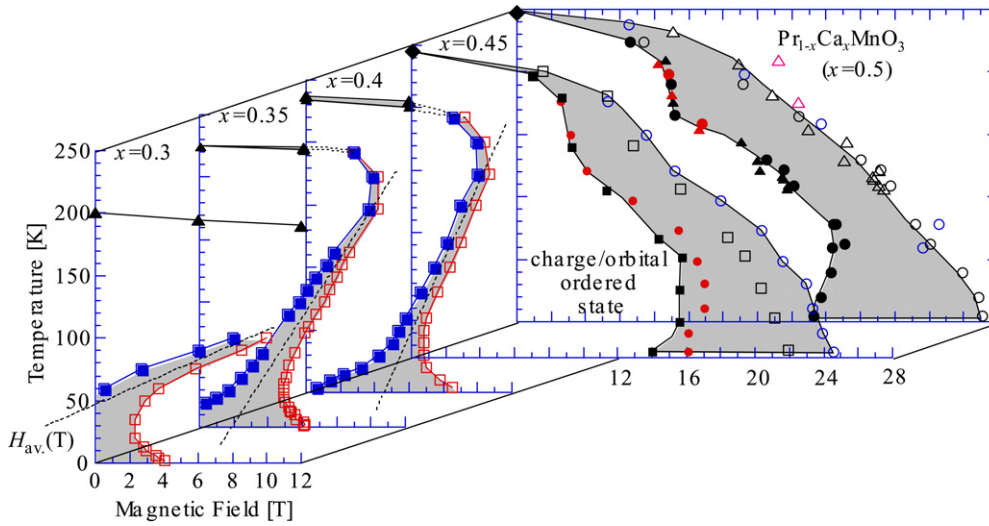
Figure 12. The charge/orbital-ordered state of $Pr_{1-x}Ca_xMnO_3$ ($x = 0.5$, 0.45, 0.4, 0.35 and 0.3), which is plotted on the magnetic field–temperature plane. The hatched area indicates the hysteresis region. In the cases of $x = 0.3$, 0.35 and 0.4, the lines of $H_{av}(T)$ at which the free energies of both the charge/orbital-ordered and the FM metallic states are supposed to be equal are indicated by dashed lines (from [32]).

from the commensurate value of 0.5, extra electrons are doped on the Mn^{4+} sites in a naive sense. To explain the modification of the arrangement of spins along the c-axis, Jirak et al [66] postulated that the extra $3z^2$–r^2 electrons hop along the c-axis mediating the ferromagnetic DE interaction. In fact, the one-dimensional ordering of the $3z^2$–r^2 electrons along the c axis (z direction) has been confirmed by the transmission electron microscopy on $Pr_{1-x}Ca_xMnO_3$ ($x = 3/8 = 0.375$) [68], in which the extra electron density, one per four Mn^{4+}-sites, becomes commensurate. Such an effect of extra electrons on the magnetic structure should be enhanced with the decrease of x from 0.5. In fact, neutron diffraction studies [53, 66] have revealed that the coupling of spins along the c-axis becomes almost ferromagnetic at $x = 0.3$ in spite of the CE-type ordering being maintained within the orthorhombic ab-plane and the OO q-vector within the ab plane being nearly commensurate as in the original $x = 1/2$ state, at least at low temperatures. Above $x = 0.5$, in contrast, the in-plane q-vector for the OO becomes incommensurate, following approximately the relation that $q \sim (1-x)/2$ (in the cubic setting), reflecting the decrease in the e_g electron number [69].

It is now well known [32] that spectacular insulator–metal transitions can be induced by external magnetic fields in the CO/OO manganites of $RE_{1-x}Ca_xMnO_3$, with the doping level mostly between $x = 0.3$ and 0.5. The phase competing with the CO/OO is mainly the ferromagnetic-metallic (FM) one for $x < 0.5$, while for $x > 0.5$ it is the A-type (x^2–y^2 orbital-ordered) or the C-type ($3z^2$–r^2 orbital-ordered) AFM phase, reflecting the aforementioned dimensional crossover of the DE interaction. Therefore, phase conversion due to the Zeeman energy gain by external magnetic fields is rather restricted to the case of the phase competition with the FM state, not the AFM states, and hence to the case of $x < 0.5$. In figure 12 the phase diagrams in the plane of the magnetic field and temperature for $Pr_{1-x}Ca_xMnO_3$ with varying

x from 0.3 up to 0.5 are shown. In this figure, the phase boundaries have been determined by the measurements of the magnetic field dependence of resistivity (ρ–H) and magnetization (M–H) at fixed temperatures. The hatched area in the figure represents the magnetic-field hysteresis region accompanied by the first-order nature of the transition. As already noted above, the critical field to destroy the CO/OO state at $x = 0.5$ becomes as large as about 27 T at 4.2 K, and a similar feature is also seen for $x = 0.45$ [65]. For $x < 0.4$, in contrast, the charge/orbital-ordered phase-region shrinks remarkably, in particular at low temperatures. The averaged value (H_{av}) of the critical fields in the H-increasing and -decreasing runs at a constant temperature apparently decreases with the decrease in temperature below $\approx$175 K ($dH_{av}/dT < 0$). In the case of $x = 0.3$, collapse of the CO/OO state (i.e. appearance of the FM state) is realized by applying an external magnetic field of only several tesla when the temperature is set below 50 K. Another noteworthy aspect in figure 12 is the expansion of the field-hysteresis with decreasing temperature, which is characteristic of the first order phase transition as mentioned above. Such a variation of the CO/OO phase with the doping level has been observed similarly for a further reduced-W system, $Nd_{1-x}Ca_xMnO_3$ [65, 70]. The common feature for the modification of the phase diagram with x seems to be correlated with the action of the extra electron-type carriers in the CE-type structure as well as the increasing stability of the competing FM phase. Thermodynamically, excess entropy may be brought about in the CO/OO state by the extra localized carriers and their relevant orbital degrees of freedom, which are pronounced as x deviates from 0.5. Such excess entropy in the 'doped' CO/OO state may rather stabilize the CO/OO state with increasing temperature and increase the critical magnetic field ($dH_{av}/dT < 0$) as observed in the case of $x < 0.4$ in figure 12.

Next, we show the electronic structural change during the magnetic field induced melting of CO/OO. First, to see the incommensurate doping effect on the electronic structure, the optical conductivity spectrum $\sigma(\omega)$ is shown in figure 13 for $Pr_{1-x}Ca_xMnO_3$ ($x = 0.4$) with $E \| b$ and $E \| c$ at 293 K (a) and 10 K (b) [71]. (Spiky structures below 0.06 eV are due to optical phonon modes.) At 293 K above T_{CO}, the anisotropy of $\sigma(\omega)$ is quite small, as well as in the $x = 0.5$ case of $Nd_{1-x}Ca_xMnO_3$ (figure 9), and the minute polarization dependence is perhaps due to the inherent orthorhombic distortion. With the decrease in temperature from 293 K to 10 K, the spectral weight of both the b- and c-axis polarized $\sigma(\omega)$ below $\approx$0.2 eV is suppressed, indicating the opening of the charge-gap in the CO/OO state. In the CO/OO state at 10 K (viewed as the ground state), the difference between the b- and c-axis polarized $\sigma(\omega)$ becomes large reflecting the anisotropy of the ordering pattern of the charge, spin and orbitals. The most notable anisotropic feature is that each $\sigma(\omega)$ has a different onset energy (Δ_b and Δ_c), as can be estimated by extrapolating linearly the rising part of the b- and c-axis polarized $\sigma(\omega)$ to the abscissa as shown by dashed lines in figure 13(b). It is reasonable to consider that the Δ_b is dominated by the optical transition of a $3x^2$–r^2 or $3y^2$–r^2 electron to the neighbouring Mn^{4+} site with a parallel spin (see figure 3). The $3x^2$–r^2 ($3y^2$–r^2) electron can hardly hop along the c-axis due to a small transfer integral as well as to a large on-site Coulomb energy as argued in the last section. On the other hand, Δ_c originates from the intersite transition of such excess $3z^2$–r^2 electrons as introduced into the CE-type CO/OO state by decreasing x from $x = 1/2$ [66]. The fact of $\Delta_c < \Delta_b$ implies that the effective intersite Coulomb correlation is larger for the in-plane than for the c-axis in such an 'electron-doped' CO/OO state. Under these circumstances, the charge-gap energy should be assigned to Δ_c ($\approx$0.18 eV) at the ground state.

The magnetic field dependence of the b- and c-polarized $\sigma(\omega)$ in a $Pr_{1-x}Ca_xMnO_3$ ($x = 0.4$) crystal at 30 K is shown in figure 14 [71], which represents the field-induced collapse of the gap structure in the course of the magnetic field-induced insulator–metal transition (see the $x = 0.4$ phase diagram shown in figure 12). (Both the b- and c-polarized optical spectra
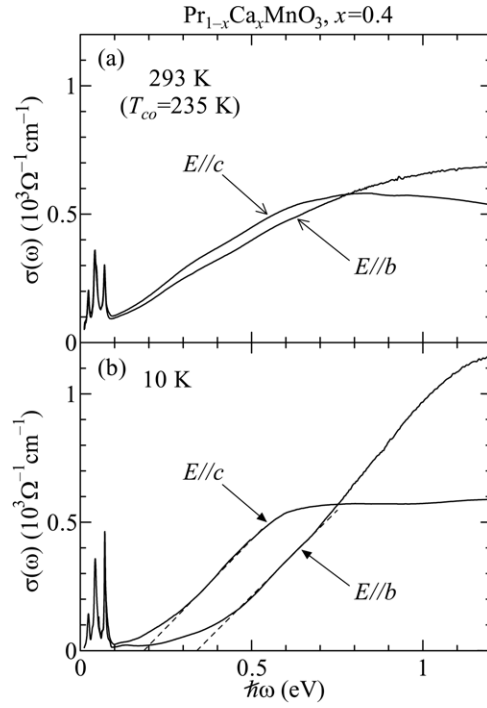
Figure 13. The anisotropy ($E\|b$ and $E\|c$ polarization) of the optical conductivity in a single crystal of $Pr_{1-x}Ca_xMnO_3$ ($x = 0.4$) at 293 K (charge–orbital–spin disordered state) and 10 K (CO/OO state with the pseudo-CE type spin order) (from [71]).

scarcely change from 10 to 30 K.) With the increase in the magnetic field, the spectral weight for b(in-plane)-polarized $\sigma(\omega)$ appears to be transferred from the higher to the lower energy region, accompanying the isosbestic (equal-absorption) point at ≈ 0.7 eV, to fill-in the gap feature. Around 7 T the change in the spectrum is abrupt, violating the isosbestic-point rule, and the metallic feature with closed gap emerges. (A sharp spike structure at the lower edge of the spectrum is due to the highest-lying oxygen stretching mode phonon.) The c-polarized $\sigma(\omega)$ shows a similar dramatic change with the magnetic field. In particular, the onset of the $\sigma(\omega)$, i.e. the charge gap Δ_c, gradually shifts to a lower energy, and at 7 T the charge gap appears to close, reflecting the CO/OOI to FM metal transition. Whereas the resistive transition indicates the strong first-order nature of the phase transition, the electronic structural change up to the transition magnetic field is huge but continuous. Conversely, the charge gap feature in the CO/OO state, which is affected not only by the one-electron bandwidth W but also the incommensurate doping $(1/2 - x)$, determines the relative stability to the FM metal state and hence the transition magnetic field as shown in figures 11 and 12.

It is worth seeing the bandwidth dependence of the CO/OO instability for the incommensurate doping level of $x < 0.5$, since the phase competition between the CO/OO and FM phases is critically dependent on both x and W. We exemplify in figure 15 the phase diagram relevant to the CO/OO transition in the H–T plane for $Pr_{0.65}(Ca_{1-y}Sr_y)_{0.35}MnO_3$ ($x = 0.35$) crystals [72]. With partial substitution of Ca (smaller ion) in $Pr_{1-x}Ca_xMnO_3$ with Sr (larger ion), the orthorhombic distortion decreases. Accordingly W increases, thus favouring the FM state. The CO/OO region in the H–T phase diagram tends to shrink in the area with increasing Sr content, or in other words, the phase diagram appears to shift to
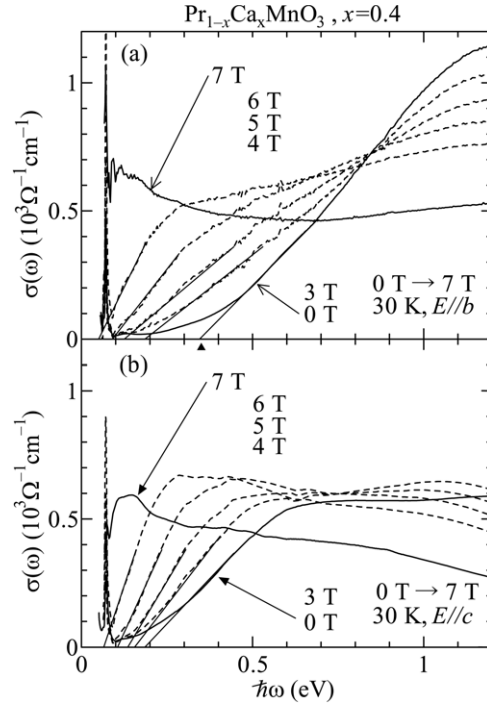
Figure 14. The magnetic-field dependence of b-polarized and c-polarized optical conductivity spectra of $Pr_{1-x}Ca_xMnO_3$ ($x = 0.4$) at 30 K. Thin slanted lines show the extrapolation procedure to determine the onset (gap) values, Δ_b and Δ_c (from [71]).

the lower field as a whole. For $y > 0.5$, the FM phase dominates and its T_C increases as y increases up to 1, i.e. $Pr_{0.65}Sr_{0.35}MnO_3$ (not shown here). This feature confirms again that the insulator–metal phase diagram below $x = 0.5$ (perhaps down to $x = 0.3$) is dominated by the competition between the DE-mediated FM state and the CO/OO state. The bicritical feature arising from this competition is a major issue in this review paper, and we start to see the case of $Pr_{1-x}(Ca_{1-y}Sr_y)_xMnO_3$ as a good example from the next section.

3. Bicritical features and colossal magnetoresistance (CMR) phenomenon

3.1. Competition between the metallic and charge–orbital ordered states

To address the essence of the CMR phenomenon, let us first give an overview of the bicritical competition between the ferromagnetic metallic (FM) state versus the charge–orbital ordered (CO/OO) state (conventionally termed the CE state, although it originally means the spin order in the CO/OO state). The most important and experimentally accessible physical parameter to control the phase competition is the transfer interaction of the conduction e_g electron or the one-electron bandwidth W of the conduction electron band. From an experimental point of view, the W of $RE_{1-x}AE_xMnO_3$ is controlled by the averaged radius of RE^{3+} and AE^{2+}, as described in section 2.1. In the reduced-W cases, other interactions competing with the DE interaction become relatively important, such as the repulsive Coulomb interaction among the e_g electrons, the charge/orbital ordering [73], the super-exchange interaction between the local t_{2g} spins [74], the collective Jahn–Teller distortion [75] etc.
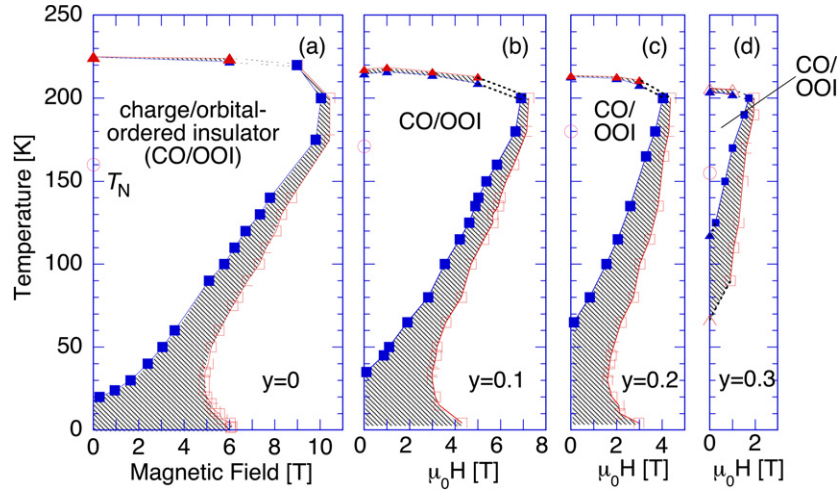
Figure 15. The phase diagrams relevant to the charge/orbital ordered insulator (CO/OOI) state and the ferromagnetic metallic (FM) state in the magnetic field–temperature plane for $Pr_{0.65}(Ca_{1-y}Sr_y)_{0.35}MnO_3$ ($y = 0$ (a), 0.1 (b), 0.2 (c) and 0.3 (d)). The critical magnetic fields (temperatures) from or to the CO/OOI state are denoted with open and closed squares (triangles). The Nèel temperature (T_N) is also indicated as open circles. The hysteretic region is represented by the hatched region (from [77]).

Here, we adopt $Pr_{1-x}Ca_xMnO_3$ as a typical example of the reduced-W cases, where the CO/OO state (the CE-type at $x = 0.5$ [76] or the pseudo-CE-type for $x < 0.5$ [66, 53]) is seen around $x = 1/2$ ($0.3 \leqslant x < 0.75$) in relation to the spatial ordering of nominal Mn^{3+}/Mn^{4+} sites with 1/1. In $Pr_{1-x}Ca_xMnO_3$, the stability of the CO/OO in magnetic fields depends on the deviation of x from 1/2, as argued in section 2.3 [67]. The critical magnetic field for the melting of the CO/OO is as high as 27 T at $x = 0.5$, as shown in figure 12 [65], while it is lowered to a few tesla at $x = 0.3$ [67]. The change in the stability seems to be related to the x-dependent modification of the spin ordering along the c axis in the pseudo-CE-type [66, 53]. In what follows, we restrict ourselves to the bicritical features in the case of slightly underdoped region, e.g. $x = 0.35$ and 0.45, to avoid the special persistence of the CO/OO state characteristic of the $x = 1/2$ filling.

As the counterpart with a relatively large W, we adopt $Pr_{1-x}Sr_xMnO_3$ ($x = 0.35$ and 0.45) whose ground state is a FM produced by the double-exchange interaction. Then, the W in this system can be tuned by partial replacement of Ca with Sr, in the form of $Pr_{1-x}(Ca_{1-y}Sr_y)_xMnO_3$, while keeping the same hole doping level x. Figure 16 exemplifies the temperature profiles of the resistivity of $Pr_{1-x}(Ca_{1-y}Sr_y)_xMnO_3$ ($0 \leqslant y \leqslant 1$) single crystals with (a) $x = 0.35$ and (b) $x = 0.45$, respectively [77]. The CO/OO state is seen at $0 \leqslant y \leqslant 0.3$ and $0 \leqslant y \leqslant 0.2$, respectively, which is manifested by a sudden increase in resistivity at around 220 K. The T_{CO} is systematically lowered as y increases. The CO/OO is, however, replaced by a FM for $y \geqslant 0.4$ ($x = 0.35$) and $y \geqslant 0.25$ ($x = 0.45$), respectively, and the T_C increases as y increases. In accordance with this, steep resistive transitions at T_C observed for $y = 0.4$ and $y = 0.25$ change to rather gradual ones at $y = 1$. In both the cases of $x = 0.35$ and 0.45, the features of the insulator to metal transition upon the substitution of Ca with Sr are quite similar although the critical y values for the transition are different. Incidentally, the resistivity for ($x = 0.35$, $y = 0.3$) shows a large decrease (increase) around 70 K (100 K) in the cooling (warming) process as shown in figure 16(a) [72, 78]. This
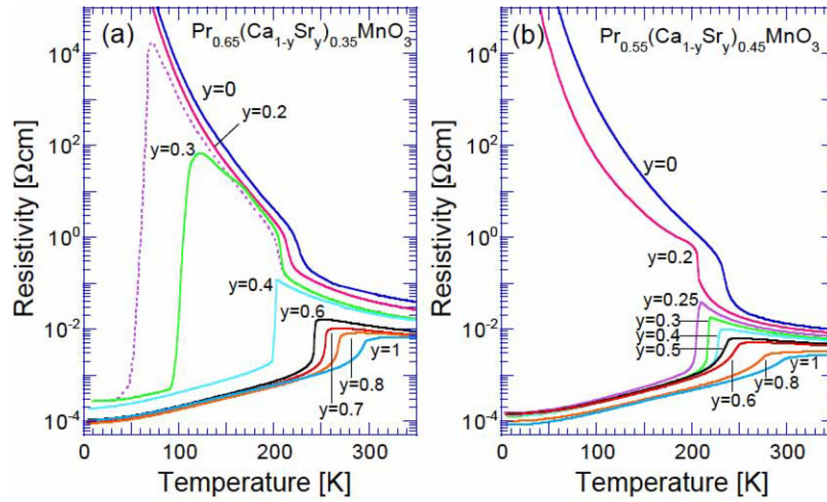
Figure 16. The temperature profiles of resistivity for $Pr_{1-x}(Ca_{1-y}Sr_y)_xMnO_3$ ($0 \leqslant y \leqslant 1$) crystals with (a) $x = 0.35$ and (b) 0.45. Solid and dotted lines denote the warming and cooling runs, respectively (from [77]).
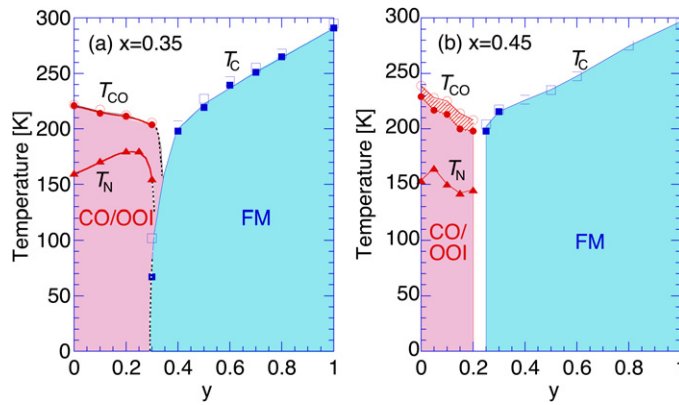

Figure 17. The electronic phase diagrams of $Pr_{1-x}(Ca_{1-y}Sr_y)_xMnO_3$ ($0 \leqslant y \leqslant 1$) with (a) $x = 0.35$ and (b) 0.45. The charge/orbital-ordered insulator and ferromagnetic metal are denoted as CO/OOI and FM, respectively. The transition from (to) the CO/OOI is denoted as open (closed) circles, and that from (to) the FM is open (closed) squares, respectively. The Nèel temperature T_N is denoted as closed triangles. The hysteresis region is hatched (from [72]).

indicates the insulator(CO/OOI)–metal(FM) re-entrant transition, reflecting the multicritical phase competition.

Figure 17 summarizes the electronic phase diagrams of $Pr_{1-x}(Ca_{1-y}Sr_y)_xMnO_3$ ($0 \leqslant y \leqslant$ 1) single crystals with (a) $x = 0.35$ and (b) 0.45, respectively [77]. The CO/OOI phase is replaced with the FM state with an increase in y, as shown in figure 17. In figure 17(a) for $x = 0.35$, however, the FM regime geometrically stretches out in the CO/OOI regime below $\sim$100 K at $y = 0.3$. This gives rise to such a CO/OO re-entrant transition as observed in the temperature dependence of resistivity for the ($x = 0.35$, $y = 0.3$) crystal (figure 16(a)). (Concerning the CO/OO related phase diagram in the $T–H$ plane for $Pr_{1-x}(Ca_{1-y}Sr_y)_xMnO_3$ ($x = 0.35$), see figure 15.) In figure 17(b) for $x = 0.45$, on the other hand, the phase boundary

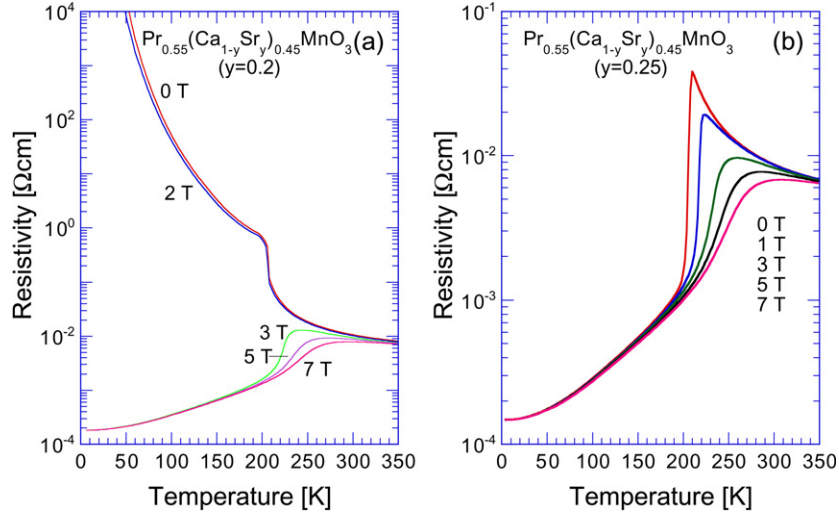**Figure 18.** The temperature profiles of resistivity (in the warming run) in several magnetic fields for $Pr_{0.55}(Ca_{1-y}Sr_y)_{0.45}MnO_3$ crystals with (a) $y = 0.2$ and (b) 0.25 (from [72]).

between the CO/OOI and the FM exists at $0.2 < y < 0.25$, i.e. within the $\Delta y < 0.05$, and hence is almost parallel to the ordinate. As a result, the phase diagram for $x = 0.45$ with respect to the CO/OOI and FM appears as a most prototypical example of the bicritical point feature.

The temperature profiles of resistivity in several magnetic fields are shown in figure 18 for (a) $y = 0.2$ and (b) 0.25 crystals. In figure 18(a), the resistivity curves for $\mu_0 H \leqslant 2\,T$ indicate the CO/OO transition at around 200 K and the subsequent insulating feature down to the lowest temperature. The resistivity for $\mu_0 H \geqslant 3\,T$, on the other hand, shows no manifestation of the CO/OO but a metallic feature below some critical temperatures. The low-temperature phase below 200 K is abruptly switched as a whole from the CO/OOI to the FM by application of $\mu_0 H = 3\,T$ for this compound. In other words, the point of $(T_{CO} = T_C = 200\,K, \mu_0 H = 2\text{--}3\,T)$ also appears as the bicritical point in the (T, H) plane of the CO/OO phase diagram. As the magnetic field is increased, the metallic state is expanded to higher temperatures. On the other hand, in figure 18(b) for $y = 0.25$, a huge decrease in resistivity is already seen at zero field, and the resistive behaviour in magnetic fields shows the prototypical CMR feature. This again confirms that the competition between CO/OO and FM at $y = 0.25$ is so critical that an application of an external magnetic field removes the antiferromagnetic correlation above T_C and causes CMR. Near this bicritical point, therefore, the prototypical CMR feature is seen on the FM side, whereas the melting of the charge/orbital order by relatively low magnetic fields is observed on the CO/OOI side.

We show in figure 19 the extended phase diagram for $x = 0.45$ over a wide regime of the A-site averaged ionic radius r_A [77]. To add the data points to the case of $Pr_{1-x}(Ca_{1-y}Sr_y)_xMnO_3$ ($x = 0.45, 0 \leqslant y \leqslant 1$), we have made use of the results for single crystals of $RE_{1-x}Ca_xMnO_3$ ($x = 0.45$, RE = Gd, Sm and Nd) as well as for $(Pr_{0.5}La_{0.5})_{1-x}Sr_xMnO_3$ and $La_{1-x}Sr_xMnO_3$ ($x = 0.45$) [77]. It is even more evident in this broader perspective that the competition between the CO/OOI and the FM exhibits the bicritical feature: both T_{CO} and T_C systematically decrease towards the CO/OOI–FM phase boundary and finally coincide with each other, $T_{CO} = T_C \approx 200\,K$, forming the bicritical
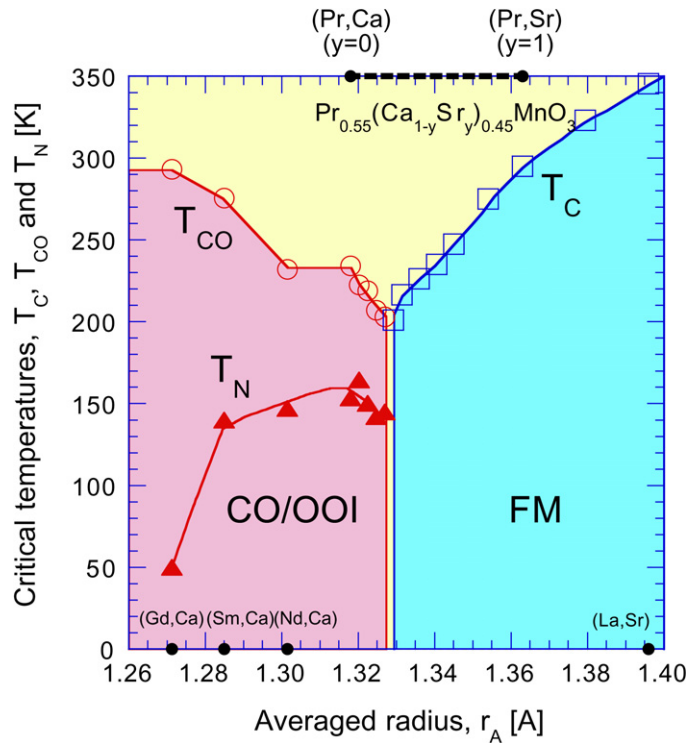
Figure 19. The extended phase diagram for $x = 0.45$ over a wide regime of the A-site averaged ionic radius, which includes the results for single crystals of $R_{1-x}Ca_xMnO_3$ ($x = 0.45$, $R = $ Gd, Sm and Nd) as well as for $(Pr_{0.5}La_{0.5})_{1-x}Sr_xMnO_3$ and $La_{1-x}Sr_xMnO_3$ ($x = 0.45$). The T_{CO} and T_C, which are determined by averaging the values in the cooling and warming runs, are denoted as open circles and squares, respectively. The antiferromagnetic charge/orbital-ordered insulator and ferromagnetic metal are denoted as CO/OOI and FM, respectively. The Nèel temperature T_N is denoted as closed triangles (from [77]).

point. Incidentally, the AF spin ordering temperature, T_N, tends to rather decrease with a decrease in the A-site ionic radius or the W, though showing a critical decrease also near the CO/OO–FM phase boundary. This reflects the fact that the CE-type spin ordering on the *ab* plane is mediated by the local double exchange interaction [66, 76].

The bicritical feature under the competition between the CO/OO and FM phases was also theoretically investigated by Murakami and Nagaosa in terms of the renormalization group (RG) analysis on the phenomenological Ginzburg–Landau (GL) model as constructed by symmetry argument [79]. Beyond the mean-field approximation, the RG analysis predicts the two important features as observed by the experiments: one is the first-order nature of the FM transition on the wider-W side around the bicritical point and the other is the clear dip structure of both the transition temperatures, T_{CO} and T_C, near the critical bandwidth W_c. Both the effects can be considered as originating from the large fluctuation inherent to the bicriticality. Such enhanced fluctuation makes the system sensitive to the applied magnetic field (H), which causes the CMR. The RG analysis on the GL free energy derived the critical scaling law for the relation between H/M and M^2 (Arrott plot), which describes the scaling curve of the experimental data [79]. This confirms the enhanced fluctuation near the bicritical fixed point. This analysis is valid in the case of minimal disorder effect. In the presence of the

relatively strong disorder as described in the next section, however, the fluctuation enhancement with the steep reduction in T_C is too much for the RG analysis to be valid. Thermodynamic singularities near T_C in the samples with possible phase separation have also been discussed in terms of Griffiths singularity [80].

3.2. Enhanced phase fluctuation and CMR

The bicritical features arising from the phase competition between the FM and the CO/OO state is one of the key ingredients in the CMR physics. However, the phase competition feature cannot be determined solely by the 3d electron transfer interaction or one-electron bandwidth W. In other words, the electronic structure/property can be different even for the identically distorted perovskite lattice structure, the latter of which is almost solely determined by the tolerance factor or the A-site averaged ionic radius. This was convincingly suggested by Attfield and Rodriguez-Martinez [81] who demonstrated that the ferromagnetic transition temperature as well as the metal–insulator behaviour depends strongly not only on the averaged ionic radius but also on the size mismatch of the trivalent rare-earth and divalent alkaline-earth ions of the A-site. The latter effect representing the local lattice distortion transmitted from the randomly substituted A-site can be measured by the variance $\sigma^2 = \Sigma(x_i r_i^2 - r_A^2)$, where x_i and r_i are the fractional occupancies and the effective ionic radii of cations of RE and AE, respectively. We will comprehensively argue such a remarkable effect of the quenched disorder on the CMR phenomena in section 4. Here we focus on the case of $RE_{0.55}Sr_{0.45}MnO_3$ (RE = La, Pr, Nd, Sm, Eu, Gd and $Sm_{1-y}Gd_y$ ($0 \leqslant y \leqslant 1$)), which shows a fairly large σ^2 in contrast to the case of $Pr_{0.55}(Ca, Sr)_{0.45}MnO_3$ described in section 3.1. Below we give an overview of the electronic phase diagram for $RE_{0.55}Sr_{0.45}MnO_3$ compared with the case of the prototypically bicritical case of $Pr_{0.55}(Ca, Sr)_{0.45}MnO_3$ to underline the important role of the quenched disorder on the gigantic phase fluctuation and the CMR effect. (Concerning a more global phase diagram in the plane of the quenched disorder and the one-electron bandwidth, see section 4.2.)

Figure 20 shows the electronic phase diagram of the $RE_{0.55}Sr_{0.45}MnO_3$ crystals as a function of the averaged radius of the A-site ions [82] in comparison with that of $Pr_{0.55}(Ca_{1-y}Sr_y)_{0.45}MnO_3$ (see section 3.1). The observed feature shows quite a contrast between the two series of compounds. Nevertheless, the lattice parameters of the orthorhombically distorted perovskite structure (P_{bmn}) are almost identical when the averaged ionic radius plotted as the abscissa is common. In $RE_{0.55}Sr_{0.45}MnO_3$, T_C decreases from ∼280 to ∼130 K as RE changes from Nd to Sm [83]. In $(Sm_{1-y}Gd_y)_{0.55}Sr_{0.45}MnO_3$, it further decreases down to ∼50 K at $y \sim 0.5$, and then the FM is taken over by a spin-glass(SG)-like insulator (SGI) for $y \geqslant 0.6$. In the $Pr_{0.55}(Ca_{1-y}Sr_y)_{0.45}MnO_3$ system, by contrast, the reduction in T_C is not so remarkable as in the $RE_{0.55}Sr_{0.45}MnO_3$ system. Moreover, as described in the previous section, the phase change from a FM to a CO/OOI (long range) is typically bicritical with $T_C = T_{CO} \sim 200$ K. The large modification of the phase diagram in the present case (figure 20) is likely to arise from the random potential affecting the FM versus CO/OO bicritical feature. The source of the random potential may be the local lattice distortion arising from the larger mismatch of the ionic size between RE (Sm, Eu and Gd) and Sr ions than between the Pr and (Ca, Sr) ones [81].

Hereafter, we first focus on the metal–insulator phenomena in single crystals of $RE_{0.55}Sr_{0.45}MnO_3$ (RE = Sm, Eu, Gd and $Sm_{1-y}Gd_y$ ($0 \leqslant y \leqslant 1$)), which is distinct from such a typical bicritical feature as observed in the $Pr_{0.55}(Ca_{1-y}Sr_y)_{0.45}MnO_3$ system. A systematic study of $(Sm_{1-y}Gd_y)_{0.55}Sr_{0.45}MnO_3$ indicates that the FM is kept up to $y \sim 0.5$ (corresponding to RE = Eu) with a reduced T_C of ∼50 K, while it changes
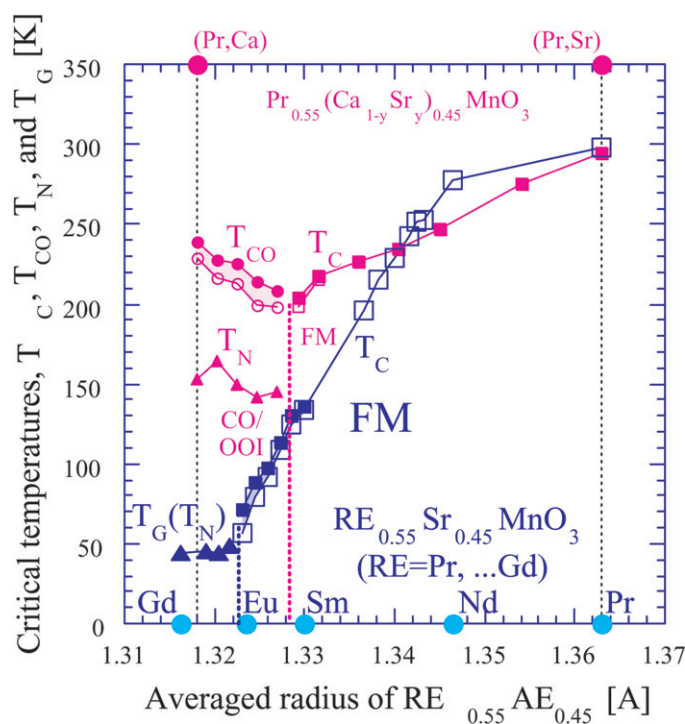
Figure 20. The electronic phase diagram of $RE_{0.55}Sr_{0.45}MnO_3$ (RE = Pr, Nd, Sm, Eu and Gd) as a function of the averaged ionic radius of the A-site in comparison with that of $Pr_{0.55}(Ca_{1-y}Sr_y)_{0.45}MnO_3$. For the $RE_{0.55}Sr_{0.45}MnO_3$ system, the data for $(Nd_{1-y}Sm_y)_{0.55}Sr_{0.45}MnO_3$ $(0 < y < 1)$ and $(Sm_{1-y}Gd_y)_{0.55}Sr_{0.45}MnO_3$ $(0 < y < 1)$ are also indicated. The charge–orbital ordered insulator, spin glass insulator and ferromagnetic metal are denoted as CO/OOI, SGI and FM, respectively. The transition from (to) CO/OOI is represented by closed (open) circles and that from (to) FM by closed (open) squares, respectively. The spin glass transition temperature T_G is indicated by closed triangles. The hysteresis regions are hatched (from [82]).

to a SGI for $y \geqslant 0.6$ [82]. The RE- or y-dependent competing features between a FM and a paramagnetic or SG-like insulator [84, 85] are characterized by short-range charge/orbital ordering, while no macroscopic phase separation is discerned when high-quality single crystal specimens are used. The short-range charge/orbital ordering can be probed by neutron/x-ray/electron diffraction techniques as well as by some optical means, such as optical conductivity and Raman scattering spectra. We show some examples below.

Figure 21 exemplifies the temperature profiles of the charge/orbital correlations coupled with the charge transport for $RE_{0.55}Sr_{0.45}MnO_3$ (RE = Nd, Sm, Eu and Gd) and $(Sm_{1-y}Gd_y)_{0.55}Sr_{0.45}MnO_3$ ($y = 0.5$ and 0.7): (a) intensity of x-ray diffuse scattering around $(2\,2\,0)$ in the orthorhombic *Pbnm* setting (corresponding to $(0\,2\,0)$ reflection in the pseudo-cubic setting), (b) intensity of the Raman phonon mode around $490\,cm^{-1}$ and (c) resistivity. The diffuse scattering intensity (figure 21(a)) and the Raman intensity (figure 21(b)) both represent the charge/orbital correlation. In figure 21(c), an anomaly in resistivity is seen at $\sim280\,K$ ($= T_C$) for RE = Nd, while it is lowered to $\sim130\,K$ for RE = Sm. For RE = Eu, T_C is further lowered to $\sim50\,K$, at which resistivity drops by more than seven orders of magnitude. For RE = Gd, the resistivity is no longer metallic down to the lowest temperature. For an alloying

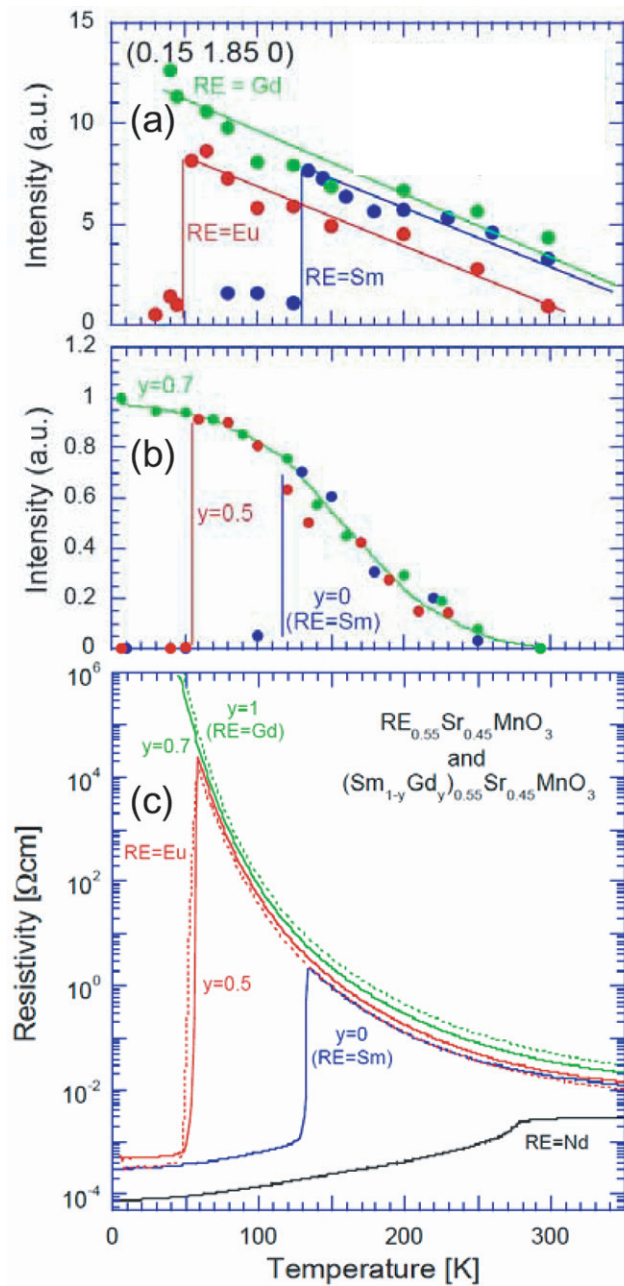**Figure 21.** Temperature profiles of (*a*) the intensity of x-ray diffuse scattering around (0 2 0) diffraction for $RE_{0.55}Sr_{0.45}MnO_3$ (RE = Sm, Eu and Gd), (*b*) the intensity of Raman phonon mode around 490 cm^{-1} (see figure 3) for $(Sm_{1-y}Gd_y)_{0.55}Sr_{0.45}MnO_3$ ($y = 0$, 0.5 and 0.7) and (*c*) resistivity in cooling runs for the crystals of $RE_{0.55}Sr_{0.45}MnO_3$ (RE = Nd, Sm, Eu and Gd) (——) as well as $(Sm_{1-y}Gd_y)_{0.55}Sr_{0.45}MnO_3$ ($y = 0.5$ and 0.7) (······). The solid line in (*a*) and (*b*) is a guide for the eyes. The inset of (*a*) shows x-ray diffuse scattering around (0 2 0) reflection for $Eu_{0.55}Sr_{0.45}MnO_3$ taken at 55 and 45 K. The intensity of the diffuse scattering at (0.15 1.85 0) was estimated by fitting the profile of $(0.15 + \varepsilon\,1.85 + \varepsilon\,0)$ ($-0.25 \leqslant \varepsilon \leqslant 0.25$) with a Gaussian form and normalized by an intensity of (1 1 0) reflection. The reflections are indexed in the pseudo-cubic setting. The reflection at the right side of (0 2 0) is due to the twinning of the crystal (from [82]).

system of $(Sm_{1-y}Gd_y)_{0.55}Sr_{0.45}MnO_3$, the FM state is seen as the ground state at $0 \leqslant y \leqslant 0.5$, while as insulator at $0.6 \leqslant y \leqslant 1$. In figure 21($c$), the temperature profiles of resistivity for $(Sm_{1-y}Gd_y)_{0.55}Sr_{0.45}MnO_3$ ($y = 0.5$ and 0.7) are also shown in comparison with those of $Eu_{0.55}Sr_{0.45}MnO_3$ and $Gd_{0.55}Sr_{0.45}MnO_3$, respectively, whose resistive (and other) behaviour is almost parallel.

In the CO/OO with $x = 1/2$ at $T < T_{CO}$, superlattice diffractions, e.g. (2 5/2 0), in the orthorhombic *Pbnm* setting [48], are formed due to the e_g-orbital ordering on the Mn^{3+} sublattice [36]. Even above T_{CO}, the diffuse scatterings are visible as a sign of the charge/orbital correlation in a short range [86–88]. The temperature dependence of the intensity of such a diffuse scattering is exemplified in figure 20(a). For RE = Sm and Eu, the intensity of diffuse scattering increases as the temperature approaches T_C, but it is suddenly decreased at T_C, which is in accord with the resistive transition shown in figure 21(c). On the other hand, for RE = Gd, the diffuse scattering intensity is found to persist down to the lowest temperature.

Figure 22 shows temperature profiles of magnetization (upper) as well as resistivity (lower) in magnetic fields for the crystals of $y = 0.5$ (right) and 0.7 (left) of $(Sm_{1-y}Gd_y)_{0.55}Sr_{0.45}MnO_3$, which are located in the immediate vicinity of the metal–insulator phase boundary [82]. As shown in the resistivity at zero field, a FM state is seen as the ground state for $y = 0.5$, while as an insulator for $y = 0.7$. In the case of $y = 0.7$, however, a metallic state starts to appear at 3 T and below $\sim$50 K. As the magnetic field is intensified, the metallic state is relatively stabilized in common to both the $y = 0.5$ and 0.7 crystals. In both the cases of $y = 0.5$ and 0.7, rather discontinuous changes in magnetization as well as in resistivity are observed as accompanied by thermal hysteresis, indicating the first order nature of the transitions. For $y > 0.5$, a SG-like state also prevails [84, 85]. The inset shows temperature profiles of ac susceptibility of the $y = 0.7$ crystal, which is a typical example of the insulating phases at $y > 0.5$ in $(Sm_{1-y}Gd_y)_{0.55}Sr_{0.45}MnO_3$. As shown in the inset, cusp structures are seen around 45 K, and the susceptibility below $\sim$45 K becomes frequency dependent. These features are characteristic of a SG state, indicating that the ground state at $y > 0.5$ is a SGI.

Figure 23 shows the temperature profiles of Raman phonon spectra for the crystals of (d) $y = 0.7$ and (e) $y = 0.5$ of $(Sm_{1-y}Gd_y)_{0.55}Sr_{0.45}MnO_3$, which were taken at zero field and 5 T in the incident and scattered light polarizations parallel to each other. For comparison, the spectra of a $Pr_{0.55}Ca_{0.45}MnO_3$ crystal with a long range CO/OO below $\sim$220 K are also displayed in figure 23(c). In the spectra, two major peaks are seen at $\sim$490 cm^{-1} (a Jahn–Teller mode) and $\sim$600 cm^{-1} (a breathing mode). Both the peaks have been assigned to the activated modes due to the CO/OO accompanied by collective Jahn–Teller distortion of MnO_6 octahedra [89, 90]. In the case of $y = 0.5$, the intensities of the phonon modes at zero field show a slight increase as the temperature is lowered from 120 to 60 K. Below T_C ($\sim$50 K), however, the phonon bands disappear. On the other hand, in the case of $y = 0.7$, both the phonon modes at zero field seem to increase in intensity with the decrease in temperature and keep finite intensities even at the lowest temperature. That is, the short-range charge/orbital correlation is removed at $T < T_C$ for $y = 0.5$, while it remains down to the lowest temperature for $y = 0.7$. Note that the temperature variations in the Raman mode intensity for $y = 0$, 0.5 and 0.7 are closely correlated with those of the x-ray diffuse scattering intensity and resistivity as seen in figures 21(a) and (b).

An impact of an external magnetic field also appears in the Raman phonon spectra. In the case of $y = 0.5$, the phonon modes at $\sim$490 and $\sim$600 cm^{-1} are distinctly seen at 60 and 80 K at zero field, while they disappear at 5 T. At 100 K, they are strongly suppressed at 5 T though still discernable. In the case of $y = 0.7$, similarly to the case of $y = 0.5$, the phonon modes are seen at 7 and 30 K at zero field, while they almost disappear at 5 T. At 70 K, they are strongly suppressed at 5 T. For both the $y = 0.5$ and 0.7 crystals, the observed changes in
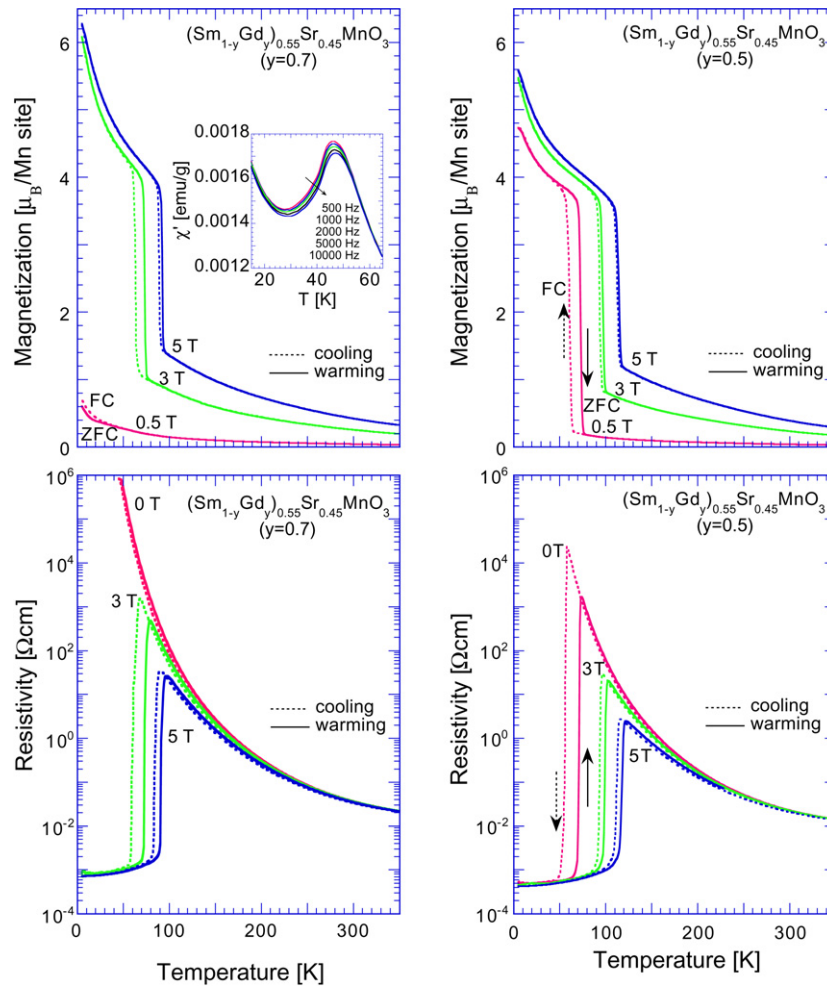
Figure 22. Temperature profiles of magnetization (upper) and resistivity (lower) in magnetic fields for crystals of $y = 0.5$ (right) and 0.7 (left) of $(Sm_{1-y}Gd_y)_{0.55}Sr_{0.45}MnO_3$. For the magnetization measurement, the sample was first cooled to the lowest temperature at zero field and then the magnetic field was set at 0.5 T, and the ZFC (zero field cooled) magnetization was measured with increasing temperature. For the cooling run, the FC (field cooled) magnetization was subsequently measured with decreasing temperature at the same magnetic field. For the other measurements of magnetization as well as resistivity, a prescribed magnetic field was first set at the highest temperature and the cooling and warming runs were measured (from [82]).

the Raman phonon spectra with variations in temperature and magnetic fields agree well with the results shown in figure 22.

The observed behaviour and phase diagram for the present $RE_{0.55}Sr_{0.45}MnO_3$ system are different from the FM versus CO/OO (long-range) bicritical feature observed for $Pr_{0.55}(Ca_{1-y}Sr_y)_{0.45}MnO_3$. Larger randomness arising from the larger mismatch of the ionic size appears to promote the phase fluctuation and reduce both the FM and CO/OO transition temperatures and in particular extinguish the long-range CO/OO down to the lowest temperature. In a most reduced-T_C state, the maximal CMR feature shows up with the strong CO/OO correlation down to T_C. As the bandwidth is further reduced, the charge/orbital correlation remains short-ranged and finally frozen to a glassy state below T_G, as evidenced
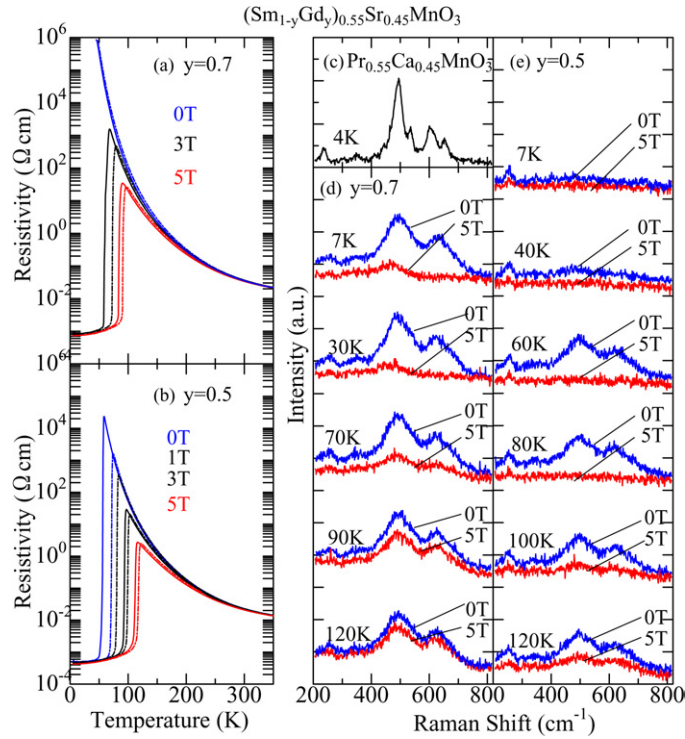
Figure 23. Temperature dependence of Raman phonon spectra (taken at the geometry of incident and scattered light polarizations parallel to each other) at zero field and 5 T for the crystals of $(Sm_{1-y}Gd_y)_{0.55}Sr_{0.45}MnO_3$ with (d) $y = 0.7$ and (e) $y = 0.5$. For comparison, the spectra of the $Pr_{0.55}Ca_{0.45}MnO_3$ crystal with long-range charge–orbital ordering are also shown in (c) (from [82]).

by the diffuse x-ray scattering and the activated broad Raman bands. For $0.6 \leqslant y \leqslant 1$, a paramagnetic ($T > T_G$) or SG-like ($T < T_G$) insulator at zero field is changed to a FM metal by the application of an external magnetic field.

3.3. Optical conductivity spectra for the CMR state

The abrupt switching of the electronic states between the short-range charge/orbital ordered and ferromagnetic metallic states is also manifested by the optical conductivity spectra. Here we exemplify the spectra for $RE_{1-x}Sr_xMnO_3$ (RE = La, Pr, $Nd_{0.5}Sm_{0.5}$, and Sm) with the doping level of $x = 0.4$ (slightly different from the $x = 0.45$ compounds described in the previous section). First, to clarify the nature of the compound series whose optical conductivity spectra are presented here, we show in figure 24 the temperature dependence of resistivity for single crystals of $RE_{1-x}Sr_xMnO_3$ ($x = 0.4$) together with the critical temperatures of the ferromagnetic transition (T_C) for the respective compounds [83] as a function of tolerance factor (f). All the compounds shown in figure 24 have the ferromagnetic metallic (FM) ground state, yet the temperature-dependent behaviour of resistivity depends critically on the RE species, similarly to the $x = 0.45$ case as described in the previous section (figure 20).

We show in figures 25(a)–(d) optical reflectivity spectra of $RE_{1-x}Sr_xMnO_3$ ($x = 0.4$, RE = La, Pr, $Nd_{0.5}Sm_{0.5}$ and Sm) at various temperatures [92]. Peak structures observed at
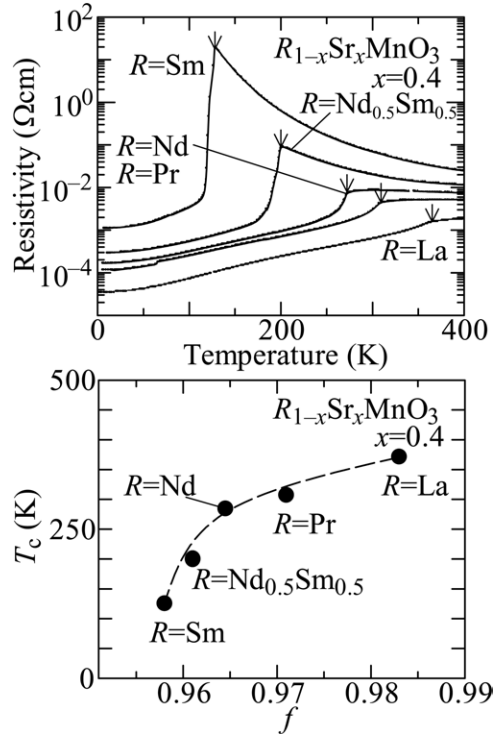
Figure 24. Lower panel: the critical temperature of the ferromagnetic transition (T_C) for the crystals of $RE_{1-x}Sr_xMnO_3$ ($x = 0.4$; RE = La, Pr, $Nd_{0.5}Sm_{0.5}$ and Sm) as a function of the tolerance factor (f), which is defined by equation (2) in the text. The dotted thin line is a guide to the eyes. Upper panel: the temperature dependence of resistivity for crystals of $RE_{1-x}Sr_xMnO_3$ ($x = 0.4$). The arrows indicate T_C (from [89]).

0.02, 0.04 and 0.07 eV are due to optical phonon absorption. The reflectivity spectra for all the crystals depend strongly on temperature, reflecting the changes in the electronic structure with spin-polarization over a broad energy range up to several eV [91]. For RE = La with maximal W, as the temperature decreases below T_C, the reflectivity below 1 eV gradually increases and then the spectra turn into a metallic reflectance band at low temperatures. As the RE-site is changed from La to Sm, the metallic reflectance band becomes more obscure, and phonon structures are pronounced, signalling a less-effective screening effect in the FM state . In particular, for RE = Sm the spectra above T_C show up as being typical of an insulator with sharp far-infrared peaks due to the optical phonon modes. As seen in figure 24, the T_Cs of RE = Sm and $Nd_{0.5}Sm_{0.5}$ are remarkably suppressed as compared with other compounds, and steep resistivity drops by several orders of magnitude are observed at T_C. Corresponding to the abrupt changes in the resistivity, the reflectivity spectra for RE = Sm and $Nd_{0.5}Sm_{0.5}$ (figures 25(c) and (d)) change steeply around T_C. These abrupt changes in the electrical property in the RE = Sm and $Nd_{0.5}Sm_{0.5}$ crystal are due to the aforementioned competition between the CO/OOI and the FM and the resultant phase fluctuation enhanced by the presence of the quenched disorder. In spite of large variation in the spectra with RE, the respective position of the apparent plasma-edge (1.5 eV) is little changed, indicating that the net oscillator strength for the $\hbar\omega < 2$ eV transitions is almost preserved (see below).

Spectra of the optical conductivity $\sigma(\omega)$, derived by the Kramers–Kronig analysis of the reflectivity spectra, are shown in figures 25(e)–(h) [92]. The $\sigma(\omega)$ for RE = $Nd_{0.5}Sm_{0.5}$
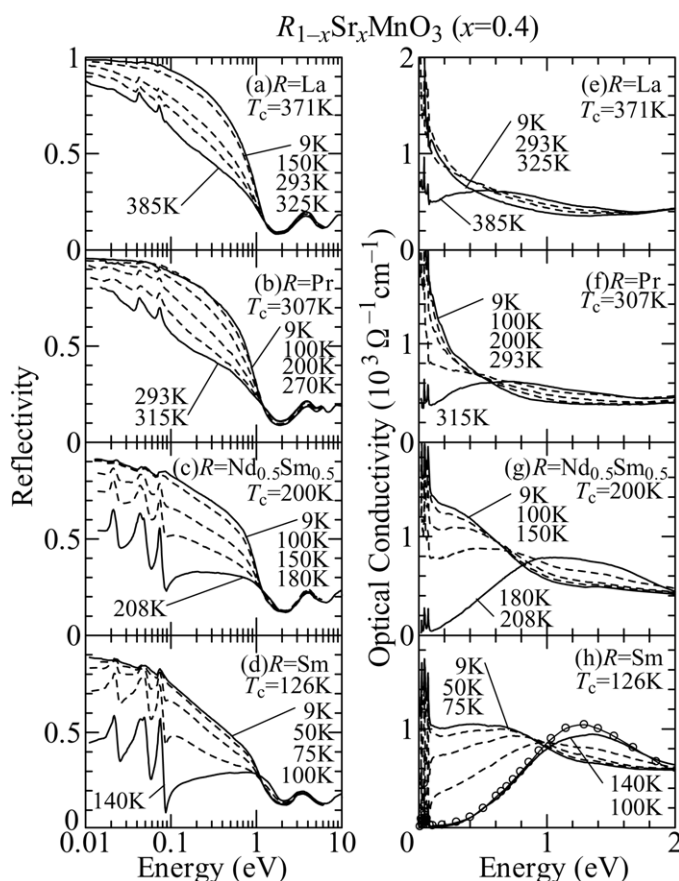
Figure 25. Left panels: reflectivity spectra at various temperatures in $RE_{1-x}Sr_xMnO_3$ ($x = 0.4$) crystals; (a) RE = La, (b) RE = Pr, (c) RE = $Nd_{0.5}Sm_{0.5}$ and (d) RE = Sm. Right panels: optical conductivity spectra at various temperatures in $RE_{1-x}Sr_xMnO_3$ ($x = 0.4$) crystals; (e) RE = La, (f) RE = Pr, (g) RE = $Nd_{0.5}Sm_{0.5}$ and (h) RE = Sm. Open circles in (h) shows, for comparison, the spectrum of $Pr_{0.6}Ca_{0.4}MnO_3$ in the charge/orbital ordered state (pseudo-CE type, at 10 K) (from [89]).

and Sm (figures 25(g) and (h)) show a broad peak around 1 eV above T_C, forming a gap-like structure. The peak shape of the spectra is much more pronounced than those of the RE = La and Pr compounds and is located at higher energy. The intraband excitations, which give rise to the low-energy(<1 eV) spectral weight, appear to be extremely suppressed, perhaps due to the aforementioned charge/orbital correlation.

As argued in the previous section, the RE = Sm compound borders the spin-glass phase with the short-range charge/orbital correlation. The short-range orbital-ordering and the collective Jahn–Teller distortion on the same correlation length scale (1–2 nm) are present above T_c in this compound, producing a conspicuous infrared peak (around 1 eV) in cooperation with the antiferromagnetic spin correlation. In fact, the spectral feature above T_C for RE = Sm ($x = 0.4$) quite resembles that of a $Pr_{1-x}Ca_xMnO_3$($x = 0.4$) crystal in the long-range charge/orbital ordered state [71], as indicated by open circles in figure 25(h) (see also figure 13). At low temperatures below T_C, the double-exchange mechanism overcomes such instability and gives rise to the abrupt phase change to the FM state.
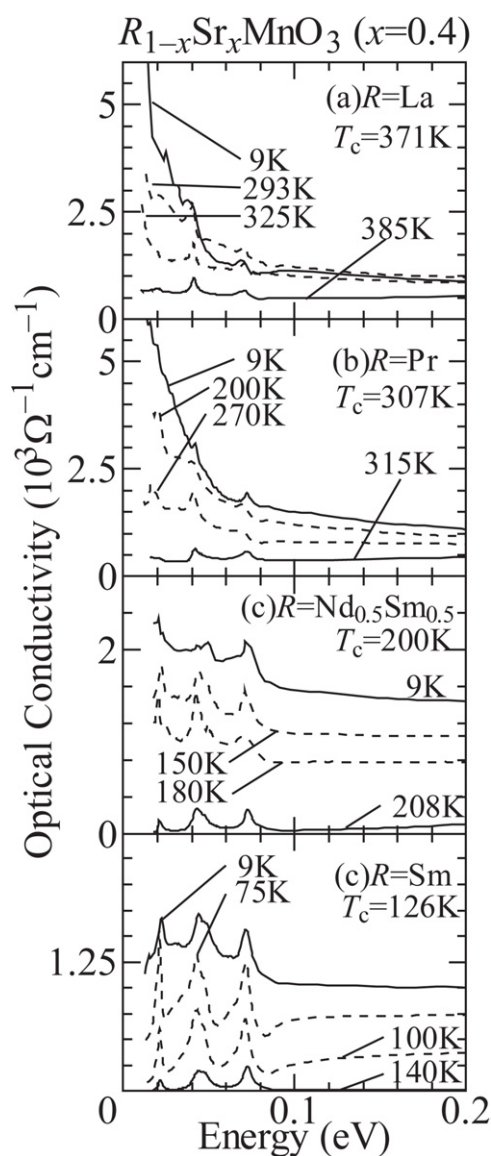
Figure 26. Temperature-dependent optical conductivity spectra magnified in a low energy region ($<0.2\,\text{eV}$) for $RE_{1-x}Sr_xMnO_3$ ($x = 0.4$) crystals with RE = La (*a*), Pr (*b*), $Nd_{0.5}Sm_{0.5}$ (*c*) and Sm (*d*) (from [89]).

With the decrease in temperature below T_C, the spectral weight of the broad peak observed just above T_C gradually decreases and is transferred to a low-energy part as seen in figures 25(*e*)–(*h*). In figure 26 we show a magnification of $\sigma(\omega)$ in the low-energy region below 0.2 eV. At low temperatures the $\sigma(\omega)$ for the maximal-W system, RE = La, forms a sharp Drude-like peak at $\hbar\omega = 0$ which reflects coherent motion of charge carriers. (Here, the nomenclature of 'Drude-like' or 'coherent' stands for the shape of $\sigma(\omega)$ with the $\omega = 0$ centred peak whose spectral width is less than ≈0.05 eV, such as $\sigma(\omega)$ of RE = La at 9 K.) However, note that the whole infrared spectral shape cannot be represented with the conventional Drude

form alone, since the broad tail of conductivity always persists more or less up to ≈ 1 eV (see figures 25(*e*)–(*f*) and 26). In $\sigma(\omega)$ for RE = Pr at 9 K, a Drude-like peak is still clearly observed, but obviously broader than that of RE = La, indicating the increased scattering rate of carriers. In the end, the low-temperature $\sigma(\omega)$ for RE = Sm is far from a conventional Drude-like shape. The $\sigma(\omega)$ for RE = Sm at 9 K, which is viewed as representing the ground-state feature, has no clear Drude-like peak in spite of the full spin-polarization of the carriers and instead the nearly ω-independent incoherent absorption is predominant. The spectral feature for RE = $Nd_{0.5}Sm_{0.5}$ is similar, although a trace of the Drude-like peak is barely discernible at 9 K as a gently increasing tail towards zero energy.

The spectral weight of such a low-lying (<1 eV) incoherent absorption appears to be transferred from the broad peak observed above T_C (see figures 25(*g*) and (*h*)). In this way, the shape of the optical conductivity spectrum for the ground state drastically changes from conventionally Drude-like to highly diffusive and nearly ω-independent, which signals coherent–incoherent crossover of charge dynamics with only modestly changing W. In particular, the zero-energy extrapolation of the broad $\sigma(\omega)$ for RE = Sm is in accord with the anomalously low dc conductivity value ($\approx 10^3 \, \Omega^{-1} \, cm^{-1}$), indicating that the incoherent component governs the dc charge transport as well. These cannot be explained by simple change in effective mass or scattering rate of the carriers. The origin of such anomalously incoherent charge dynamics in the perfectly spin-polarized metallic ground state can neither be ascribed to the CO/OO correlation nor to the phase separation, as evidenced by no observable diffraction signal for CO/OO or MR effect at the FM ground state, and still remains quite puzzling [57, 58]. The following is, however, one of the possible scenarios for explaining this mystery.

It has recently been reported that such a charge-diffusive ferromagnetic ground state as observed in $Sm_{1-x}Sr_xMnO_3$ ($x = 0.4$–0.45) shows anomalous magnon softening near the boundaries of the Brillouin zone along the $(100)_c$ and $(110)_c$, but not $(111)_c$. (Suffix 'c' denotes the cubic setting of the crystal structure.) Phenomenologically this is clearly assigned to the enhanced fourth nearest neighbour exchange interaction [93, 94]. (The fourth nearest neighbour means the Mn-site located at $2a_0$ from the origin along the $[100]_c$ or equivalent direction.) The enhanced fourth nearest neighbour exchange interaction implies the extended character of the relevant orbital state along the $[100]_c$ direction, namely the $3z^2$–r^2 type orbital [94]. Thus, the very diffusive metallic state near $x = 0.5$ may be mediated by $3z^2$–r^2 type orbitals which are not long-range ordered as in the higher-doped (>0.7) ground state (see the case of $Nd_{1-x}Sr_xMnO_3$ shown in figure 4(*b*)) but should remain short-ranged and dynamical while hosting the three-dimensional ferromagnetic interaction. Therefore, the highly incoherent charge dynamics even at the ground state may be interpreted in terms of the short-range dynamical correlation of $3z^2$–r^2 orbitals or the *nematic*-like orbital liquid–crystal state. However, the quantitative elucidation of the low-energy conductivity spectrum as well as the extremely diffusive charge transport at the FM ground state adjacent to the insulator state remains an open problem.

4. Roles of quenched disorder in the critical region

4.1. Bicriticality and quenched disorder

The presence of *quenched* disorder in the bicritical or multicritical region of the manganites can give rise to striking phenomena. Here, quenched disorder means the temperature-independent atomic-scale local inhomogeneity producing randomness in potential energy, transfer energy, electron number, exchange interaction, etc. In the following part of the paper, we argue the essential importance of the quenched disorder in the physics of CMR and related phenomena.
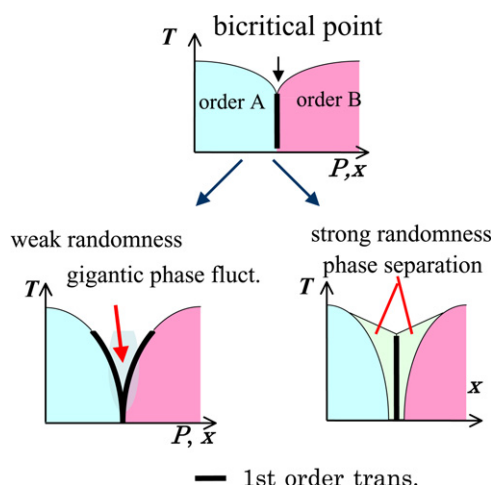
Figure 27. The phase competition forming the bicritical point (upper) and roles of quenched disorder (lower).

The prototypical example for the quenched disorder is the partial substitution of the perovskite A-site or B-site (Mn-site) with other elements. The solid solution of the perovskite A-site with divalent alkaline-earth and trivalent rare-earth ions is a common method to control the band filling (electron number) and the one-electron band width (W). The local distortion arising from the difference in ionic radii and/or the random Coulomb potential from the trivalent/divalent ion mixture is the source of the quenched disorder. In the hole-doped perovskite manganites, therefore, this kind of quenched disorder or the potential randomness is unavoidable except for some special cases (ordered double perovskites as argued in the following section). Here, we will argue in sections 4.2 and 4.3 a highly nontrivial effect of the quenched disorder arising from such a conventional solid solution on the phase competition and CMR phenomena near the bicritical region.

In section 4.4 we will further argue on qualitatively different effects caused by stronger quenched disorder near the bicritical region, that is, the phase separation into the competing two ordered phases on various time-scales and length-scales. For example, substitution of a few per cent Mn sites with other impurity atoms (e.g. Cr) can give rise to the partial melting of the long-range CO/OO state, generating the coexistent state of the ferromagnetic metal (FM) domains and CO/OO insulator (CO/OOI) domains on various length scales from nanometres to micrometres. This quite contrasts with the *homogeneous* (coarse-grained over a few nanometres) state realized by the moderate quenched disorder arising from the A-site solid solution. Thus, the role of the quenched disorder is versatile, as shown in figure 27: on the one hand it enhances the phase fluctuation near the bicritical point and turns the long-range order to the nanometric short-range one and on the other hand causes the spatial phase separation. Hereafter, we will see ample examples of this feature on the structurally-tuned CMR manganites.

4.2. Electronic phase diagrams of cation-ordered and disordered perovskites

The effect of the random potential arising from the chemical disorder is seen in the conventional random alloying on the perovskite A-site with rare-earth (RE^{3+}) and alkaline-earth (AE^{2+}) ions. The latter effect is sometimes argued in terms of difference (variance) in ionic radii of
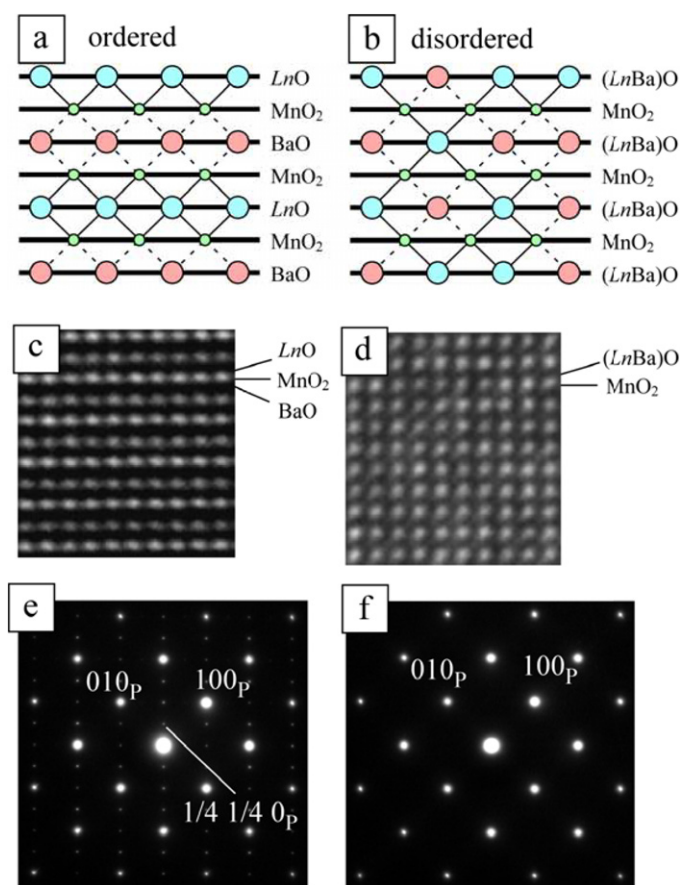
Figure 28. Schematic structures of half-doped perovskite, $Ln_{1/2}Ba_{1/2}MnO_3$, viewed along the b-axis: (*a*) the A-site ordered perovskite with an alternate stack of LnO (denoted as REO in the text) and BaO layers along the c-axis and (*b*) the A-site disordered (solid-solution) perovskite with cubic structure. The lattice images obtained by high-resolution transmission electron microscopy (HRTEM) at room temperature are shown for (*c*) the A-site ordered and (*d*) disordered $Sm_{1/2}Ba_{1/2}MnO_3$. The [001]-zone electron-diffraction pattern of (*e*) the A-site ordered and (*f*) disordered $Sm_{1/2}Ba_{1/2}MnO_3$ at room temperature. The superlattice reflections with a modulation wave vector (1/4, 1/4, 0) are clearly observed in the ordered material, proving the presence of the charge/orbital ordered phase. These superlattice reflections disappear above 380 K. For the disordered material, no superlattice reflection is observed down to low temperature, indicating no long-range charge/orbital order. (Here Ln stands for rare-earth ion, i.e. the same meaning as RE in this paper) (from [98]).

the RE^{3+} and AE^{2+} cations. Attfield and his co-workers [81, 95] are the first who explicitly argued the large change in the ferromagnetic transition temperature (T_C) with variation in the size mismatch between RE^{3+} and AE^{2+} cations, even while keeping the hole doping level (e.g. $x = 0.3$) and the averaged ionic radius (or approximately the averaged lattice structure) the same. Here, we show an example of the least chemical disorder attained in the sheet-like RE–AE ordered perovskite manganites, which can in turn visualize more clearly the dramatic effect of the quenched disorder inherent to the RE–AE solid-solution in the bicritical (or multicritical) region.

The perovskite manganites in the chemical composition of $RE_{1/2}Ba_{1/2}MnO_3$ may provide a good arena to test the above idea, since they have two possible forms of the crystal structure
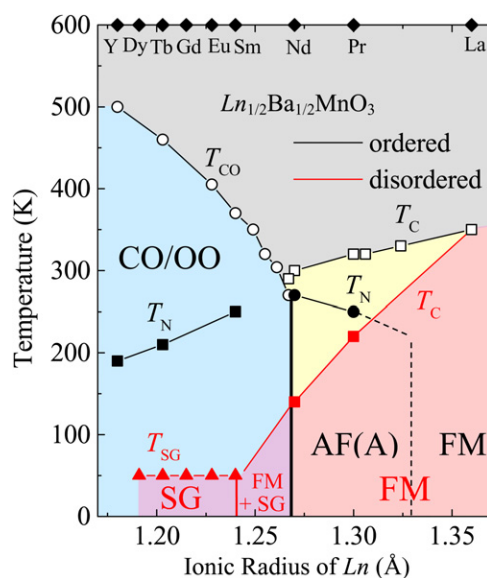
Figure 29. Electronic phase diagrams for the A-site ordered (black line and symbols) and disordered (red line and symbols; the region shaded in red) perovskites with half-doping, $Ln_{1/2}Ba_{1/2}MnO_3$, as a function of the ionic radius of Ln. CO/OO, FM and SG stand for the charge/orbital-ordered, ferromagnetic and spin-glass states, respectively. T_{CO}, T_C and T_{SG} represent the respective transition temperatures. The data for the mixed crystal compounds with Ln = (Nd, Sm) and (La, Nd), both Ln/Ba ordered and disordered, are also shown. (Here Ln has the same meaning as RE in this paper) (from [98]).

(see figures 28(a) and (b)) depending on the synthetic condition [96]. One is the A-site disordered (solid-solution) structure (figure 28(b)) and the other is the A-site ordered perovskite with an alternate stack of REO and BaO sheets along the c-axis with intervening MnO_2 sheets (figure 28(a)). Millange *et al* first studied the difference between the A-site ordered and disordered perovskites in the case of RE = La and reported that the ground states of both materials are FM metal with different T_Cs [96]. Nakajima *et al* later reported that the CO/OO transition temperature (T_{CO}) can be as high as 500 K for the ordered form of $Y_{1/2}Ba_{1/2}MnO_3$ [97] as opposed to the T_{CO} of 200–250 K in the conventional A-site solid-solution $RE_{1/2}Ca_{1/2}MnO_3$ [1]. The A-site ordering and disordering in the two kinds of crystal form can be clearly discerned in the lattice image (figures 28(c) and (d)) obtained by high resolution transmission electron microscopy (HRTEM), e.g. for the RE = Sm case [98]. Modulation of the distance between adjacent MnO_2 layers is seen in the HRTEM image of the ordered material, as attributed to the A-site ordering of Sm and Ba ions. No modulation is observed in the HRTEM image of the A-site disordered material, whose averaged structure is simple cubic perovskite. This A-site ordering is due to the large difference in the ionic radii of RE^{3+} and Ba^{2+} and reminiscent of the structure of well-known 123-type high-temperature superconductors, $REBa_2Cu_3O_7$. The respective MnO_2 sheets in this A-site ordered tetragonal form are free from the random potential which would otherwise arise from the Coulomb potential and/or local strain via the random RE^{3+}/Ba^{2+} A-sites. In contrast, the melt-grown crystal with the same A-site composition shows the complete solid-solution of RE and Ba ions on the A-sites with a simple cubic form as the average structure [98, 99].

Figure 29 shows the electronic phase diagram of $RE_{1/2}Ba_{1/2}MnO_3$ for both the A-site order and disorder [98]. The T_{CO} is as high as 500 K for the ordered form of $Y_{1/2}Ba_{1/2}MnO_3$

as the smallest-RE compound [97], but it steeply decreases with the increase in the RE ionic size. On the other hand, the T_C decreases with the decrease in the RE ionic size. Finally, both the transition temperatures for the competing phases coincide at around RE = Nd, forming the multicritical point. As seen in figure 28(a), the MnO_2 sheets sandwiched between the ordered REO and BaO layers suffer from no random potential. In contrast, the A-site disorder as illustrated in figure 28(b) generates the random Coulomb potential between the MnO_2 sheets and the (REBa)O layers as well as the random local lattice distortion. For the Mn^{3+}/Mn^{4+}-alternate CO state, this should cause a frustrating effect as well. In fact, the randomness of the solid-solution A-site was found to result in a large modification in the electronic phase diagram of $RE_{1/2}Ba_{1/2}MnO_3$, as indicated in figure 29 [98, 99]. First, the long-range order in the charge and orbital sectors with a relatively high transition temperature T_{CO} totally collapses in this A-site disordered system and remains dynamical down to the spin-glass transition temperature of about 50 K [100].

For the clarification of this feature, it is useful to compare the cases of the A-site ordered and disordered forms of $Sm_{1/2}Ba_{1/2}MnO_3$ [98]. The temperature (T) dependence of their magnetization and electrical resistivity are shown in figure 30. In the ordered form (figure 30(a)), the magnetization and resistivity simultaneously exhibit abrupt changes at 380 K where the structure changes from tetragonal with the lattice parameters of $a = 3.915$ Å and $c = 7.622$ Å at 300 K to orthorhombic with those of $a = 3.914$ Å, $b = 3.882$ Å and $c = 7.692$ Å at 380 K. The lattice-structural change is clearly ascribed to the onset of the charge/orbital order [101–105]. Figure 28(e) shows the electron diffraction projected onto the [001]-zone in the tetragonal setting, in which distinct superlattice spots (1/4, 1/4, 0) arising from the diagonal orbital/charge stripes on the Mn square lattice are discerned. The suggested orbital/charge ordering pattern in the ab-plane is identical to that of the conventional disordered manganites as described in section 2.2, but differs in its stacking pattern [$AABB$-type] along the c-axis [102, 104, 105]. Other A-site ordered materials with the ionic radius of RE smaller than that of Sm have the same CO/OO pattern as $Sm_{1/2}Ba_{1/2}MnO_3$, and the T_{CO} is raised with a decrease in ionic radius of RE, as shown in figure 29. The magnetization peak around 250 K ($= T_N$) corresponds to the antiferromagnetic transition [102]. On the other hand, the resistivity of the A-site disordered $Sm_{1/2}Ba_{1/2}MnO_3$ shows no distinct anomaly, and the magnetization behaviour, such as a difference in field-cooling and zero-field-cooling (figure 30(b)) and the frequency dependence of the ac susceptibility (inset to figure 30(b)), indicates the presence of the spin-glass state below 50 K. In accord with this, no superlattice diffraction spot is discerned by the TEM observation (figure 28(f)). These results suggest that the random potential originating in the A-site disorder totally suppresses the long-range order in the charge and orbital sectors to give rise to the SG state at a lower temperature. The glass state also appears below 50 K in other A-site disordered compounds with RE = Eu–Dy (figure 29). The correlation length of the short-range CO/OO is estimated to be as short as ≈ 2 nm, which is anticipated to bring about fragmentation of the ferromagnetic and antiferromagnetic interaction paths from the original CO/OO structure. The detailed ac susceptibility measurement on A-site disordered compounds with RE = Sm and Eu revealed the prototypical *atomic* spin-glass state [100], reflecting the nanometre-scale short-range and globally homogeneous CO/OO correlation with no phase separation.

The disorder on the perovskite A-site appears to produce a further unique feature near the original bicritical (or multicritical) point. The T_C tends to be critically suppressed with the decrease in the RE ionic radius as compared with the A-site ordered case. For RE = Nd, which would be located near the multicritical point in the ordered form, the T_C is most reduced by the A-site alloying. The magnetic and transport properties of $Nd_{1/2}Ba_{1/2}MnO_3$ are shown in figure 31. In the A-site ordered $Nd_{1/2}Ba_{1/2}MnO_3$, the magnetic transitions can be seen around
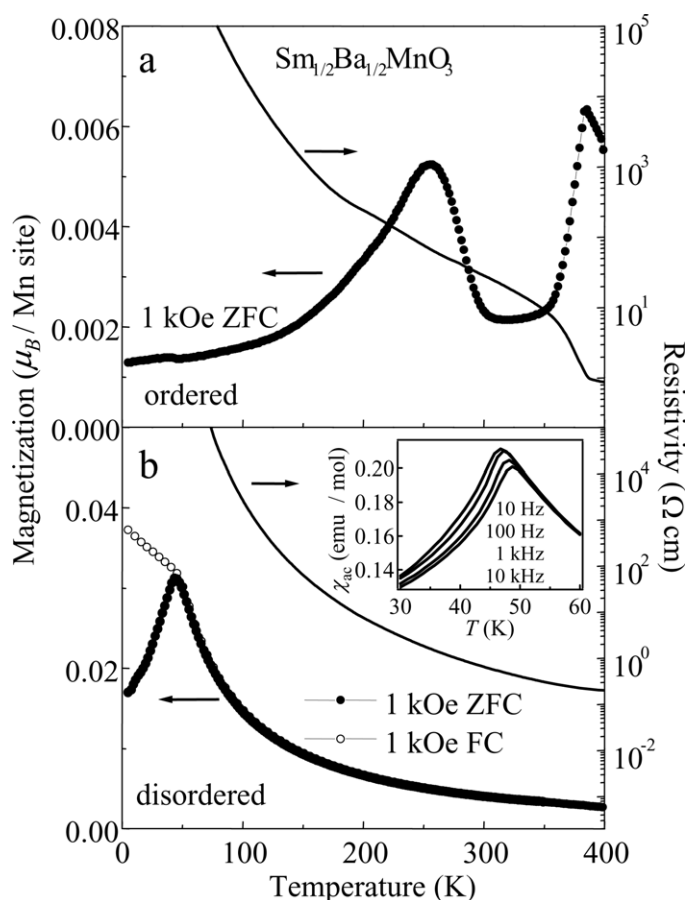
Figure 30. Temperature dependence of magnetization and resistivity for (*a*) the A-site ordered and (*b*) disordered $Sm_{1/2}Ba_{1/2}MnO_3$. The inset of (*b*) indicates the frequency dependence of the ac susceptibility (χ_{ac}). ZFC and FC represent the zero-field-cooling and field-cooling process, respectively. No significant difference is observed between ZFC and FC measurements in the ordered system. The magnetization and resistivity of the ordered material shows an abrupt change at around 380 K, above which the superlattice reflections (figure 28(*e*)) disappear (from [98]).

300 and 270 K. The steep onset of the magnetization around 300 K may indicate the onset of the FM state or the strong FM fluctuation. Around 270 K, the magnetization and resistivity simultaneously show a steep change. The magnetization anomaly at 270 K is due to the onset of the A-type antiferromagnetic (AFM) state [105, 106]. The *ab*-plane is FM associated with the ordering of $x^2 – y^2$ orbitals and stacks antiferromagnetically along the *c*-axis. The A-type AFM phase adjacent to the FM state is well known for the nearly half-doped manganites, as argued in section 2.2. In the clean limit the two ordered states, i.e. the CO/OO and FM states, appear to meet at around RE = Nd ($y = 1$). Thus, the A-site ordered $Nd_{1/2}Ba_{1/2}MnO_3$ is close to the multicritical point where the three ordered states, i.e. FM, A-type AFM and CO/OO states, compete with each other and the respective transition temperatures converge. The T_C of the ordered $RE_{1/2}Ba_{1/2}MnO_3$ shows an increase with the change in the RE ion from Nd (300 K) to La (350 K) as seen in figure 29, while the A-type AFM phase disappears between RE = Pr and La.

In contrast, the A-site disorder in $Nd_{1/2}Ba_{1/2}MnO_3$ located near the original multicritical point tends to suppress such long-range order. The magnetic and electrical properties of
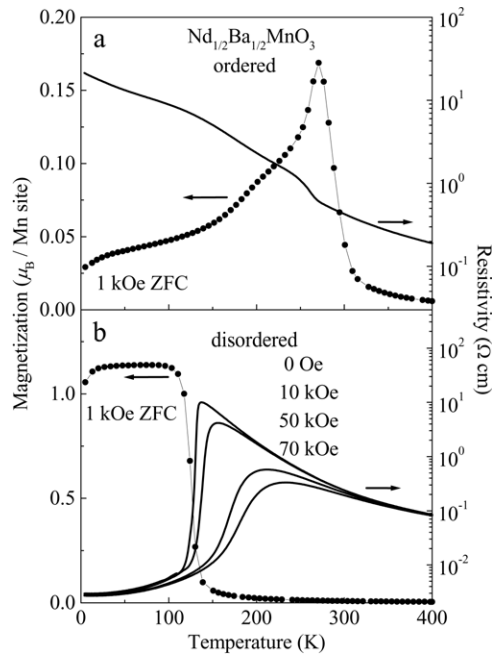
Figure 31. Temperature dependence of magnetization and resistivity for (*a*) the A-site ordered and (*b*) disordered $Nd_{1/2}Ba_{1/2}MnO_3$. No significant difference is seen between ZFC and FC measurements in either system. The A-site disordered material shows the typical CMR behaviour around T_C. Note the logarithmic scale on the ordinate for the resistivity (from [98]).

the disordered $Nd_{1/2}Ba_{1/2}MnO_3$ as observed in figure 31(*b*) indicate that the ground state is the FM with a much decreased T_C of 140 K and that a typical CMR effect accompanying the resistivity change by three orders of magnitude is observed near and above T_C [98]. The charge–orbital correlation as evidenced by x-ray diffuse scattering tends to grow with the lowering of the temperature in this compound, but suddenly disappears at T_C, as generally observed for the CMR manganites (see for example figure 21), in accord with the sharp and gigantic drop in resistivity at T_C (figure 31(*b*)). As described in section 3.2, the CMR effect is maximized in such a most reduced-T_C material as the present A-site disordered $Nd_{1/2}Ba_{1/2}MnO_3$.

4.3. Global phase diagram in the plane of one-electron bandwidth and quenched disorder

The solid solution of RE^{3+} and AE^{2+} on the perovskite A-sites is a common technique to control the band filling (doping level) of the system in the perovskites and related oxide materials, as detailed in section 2.1, yet such a moderate disorder causes a large modification in the transition temperature T_C of the FM phase [81] and even in the phase diagram itself [82, 98, 107], near the bicritical (multi-critical) region. The magnitude of the quenched disorder (perhaps the local structural variation) arising from such a solid solution can be evaluated by the variance in the ionic radii, $\sigma^2 = \sum_i (x_i r_i^2 - r_A^2)$, where x_i and r_i are the fractional occupancies and the effective ionic radii of cations of RE and AE, respectively, as demonstrated by Rodriguez–Martinez and Attfield [81, 107]. The average ionic radius, $r_A^\bullet = \sum_i x_i r_i$, determines the average lattice structure, in most cases the orthorhombically distorted perovskite ($GdFeO_3$ type structure), and hence the one-electron bandwidth (W), as described in section 2.1.
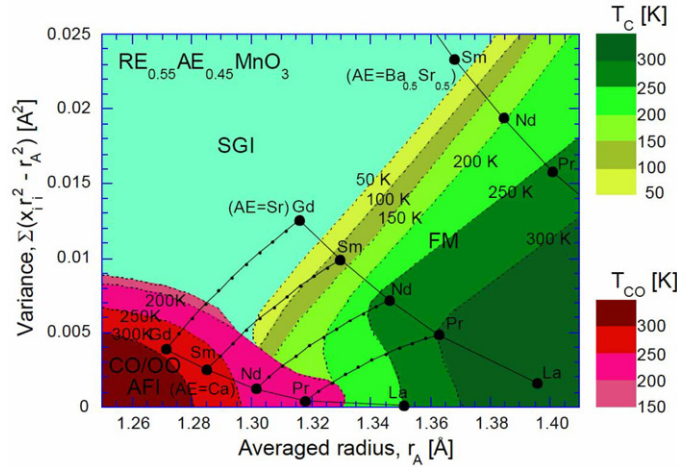
Figure 32. The electronic phase diagram of various $RE_{1-x}AE_xMnO_3$ ($x = 0.45$) crystals in the plane of r_A and σ^2. The phases of ferromagnetic metal, charge/orbital-ordered antiferromagnetic insulator and spin glass-like insulator are denoted as FM, CO/OO AFI and SGI, respectively. Contour lines of the respective transition temperatures are drawn by extrapolation on the basis of the data obtained on more than 50 single crystals. Small and large dots indicate the materials that were actually synthesized, mostly in the form of single crystals, and characterized (from [110]).

In this section, we comprehensively describe the competing features between FM and CO/OO for $RE_{1-x} AE_xMnO_3(x = 0.45)$ crystals. The reason why we have chosen the doping level of $x = 0.45$ is that near the half-doping ($x = 0.5$) the phase competition and the resultant phase variation are most clearly seen, but the exact $x = 0.5$ crystals are known to show the special stability of the CO/OO phase unique to the commensurate effect [77, 108, 109]. We show in figure 32 the electronic phase diagram of $RE_{1-x} AE_xMnO_3(x = 0.45)$ crystals plotted on the r_A–σ^2 plane [110]. Most of the data presented here were obtained for more than 50 high-quality single crystals of the manganites. First, for the lower-left and lower-right regimes, where the σ^2 is relatively small, the CO/OO and the FM are dominant, respectively. In $RE_{0.55}Ca_{0.45}MnO_3$ (RE = Gd, Sm, Nd and Pr), the CO/OO transition temperature T_{CO} shows a decrease from ~300 to ~230 K as RE changes from Gd to Pr. In $RE_{0.55}Sr_{0.45}MnO_3$ (RE = La, Pr, Nd, Sm and Gd), on the other hand, the T_C decreases from ~350 to ~130 K as RE changes from La to Sm. These features for both the CO/OO and FM regions may be interpreted in terms of the change in W. Furthermore, as shown in the cases of $RE_{0.55}(Ca_{1-y}Sr_y)_{0.45}MnO_3$ (RE = Sm, Nd and Pr) ($0 \leqslant y \leqslant 1$), the CO/OO is replaced with the FM with an increase in y, which may also be explained by the increase in W. Thus, the keen competition between the CO/OO and FM forms a prototypical bicritical point, as already described in detail in section 3.1 [77]. However, for the upper regime in this figure the spin-glass insulator (SGI) phase becomes dominant [82]. In $RE_{0.55}(Ca_{1-y}Sr_y)_{0.45}MnO_3$ (RE = Gd) ($0 \leqslant y \leqslant 1$), for example, the CO/OO is replaced with the SGI for $y > 0.3$, as described in detail in section 3.2.

As examples of experimental data which have been used to deduce the global phase diagram (figure 32), we show in figure 33 the temperature profiles of resistivity (*a*)–(*c*) and the electronic phase diagrams (*d*)–(*f*) for $RE_{0.55}(Ca_{1-y}Sr_y)_{0.45}MnO_3$ ($0 \leqslant y \leqslant 1$) with RE = Gd ((*a*) and (*d*)), Sm ((*b*) and (*e*)) and Nd ((*c*) and (*f*)), respectively [110]. In figures 33(*a*) and (*b*), the resistivity for $y = 0$ shows an anomaly around 295 K for RE = Gd and 275 K for RE = Sm in both cooling and warming runs, respectively, which manifests the CO/OO transition. Common to both cases, the T_{CO} is lowered and the transition becomes broadened
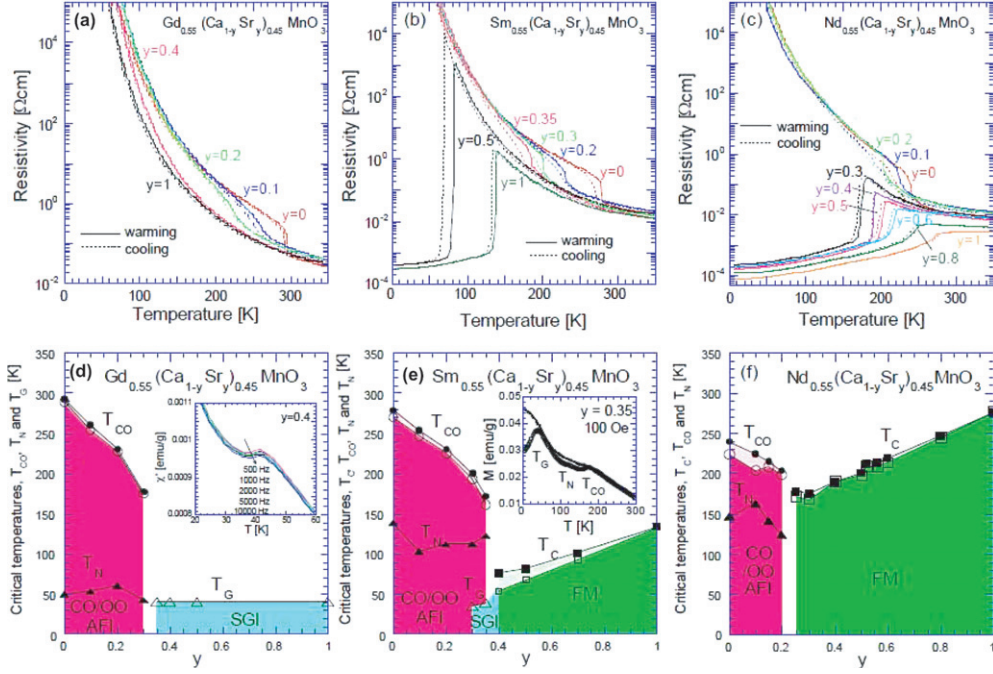
Figure 33. Temperature profiles of resistivity (*a*)–(*c*) and the electronic phase diagrams (*d*)–(*f*) for $RE_{0.55}(Ca_{1-y}Sr_y)_{0.45}MnO_3$ ($0 \leqslant y \leqslant 1$) with RE = Gd ((*a*) and (*d*)), Sm ((*b*) and (*e*)) and Nd ((*c*) and (*f*)). The T_{CO} and T_C, which were determined by the resistivity measurement, are indicated by circles and squares, respectively. The temperatures in the cooling and warming runs are denoted by open and closed symbols, respectively. The hysteresis regions are hatched. The Nèel temperature, T_N, is denoted with closed triangles. The spin glass (SG) transition temperature T_G is indicated by open triangles. The abbreviations, FM, CO/OO AFI and SGI, are the same as in figure 32. Insets show temperature profiles of ac susceptibility (χ') for the $y = 0.4$ crystal of $Gd_{0.55}(Ca_{1-y}Sr_y)_{0.45}MnO_3$ (*d*), and zero-field-cooled (ZFC) as well as field-cooled (FC) magnetization (M) for the $y = 0.35$ crystal of $Sm_{0.55}(Ca_{1-y}Sr_y)_{0.45}MnO_3$ (*e*) (from [110]).

upon the moderate substitution of Ca with Sr. In the case of RE = Gd, no distinct change is discerned in temperature profiles of resistivity for $y \geqslant 0.4$. For $y = 1$, the x-ray diffuse scattering around (2 3/2 0) of the orthorhombic *Pbnm* setting is seen below about 250 K, which is indicative of the short range CO/OO correlation [82]. In the case of RE = Sm, on the other hand, the CO/OO transition is still discerned at around 170 K at $y = 0.35$, while it is abruptly replaced with the FM for $y \geqslant 0.5$.

The inset of figure 33(*d*) shows temperature profiles of ac susceptibility for the $y = 0.4$ crystal of $Gd_{0.55}(Ca_{1-y}Sr_y)_{0.45}MnO_3$. The susceptibility becomes frequency dependent below about 40 K, that is, the SGI prevails below about 40 K in this crystal. Similarly, the inset of figure 33(*e*) shows temperature profiles of zero field cooling (ZFC) and field cooling (FC) magnetization for the $y = 0.35$ crystal of $Sm_{0.55}(Ca_{1-y}Sr_y)_{0.45}MnO_3$. The magnetization shows a tiny decrease around 180 K and a cusp structure around 120 K. With further decrease in temperature, the discrepancy between the ZFC and FC magnetization is pronounced below ≈ 40 K, which is also indicative of the re-entrant SGI below ≈ 40 K.

The electronic phase diagrams for $Gd_{0.55}(Ca_{1-y}Sr_y)_{0.45}MnO_3$ and $Sm_{0.55}(Ca_{1-y}Sr_y)_{0.45}$ MnO_3 ($0 \leqslant y \leqslant 1$) are summarized in figures 33(*d*) and (*e*), respectively. In the case of RE = Gd, even when W is increased by substitution of Ca with Sr, the CO/OO is replaced with the SGI for $y \geqslant 0.35$, and not with the FM. In the case of RE = Sm, the CO/OO is kept

at $0 \leqslant y < 0.3$, while it changes to the FM at $y \geqslant 0.4$. In the narrow intermediate regime of $0.3 \leqslant y < 0.4$, however, the SGI appears re-entrantly below about 40 K in spite of which the CO/OO transition is seen at a higher temperature.

Figures 33(c) and (f) show the temperature profiles of resistivity and electronic phase diagram for $Nd_{0.55}(Ca_{1-y}Sr_y)_{0.45}MnO_3$, respectively. In figure 33(c), the CO/OO at $y = 0$ is manifested by the resistivity anomaly around 235 K. As y increases up to 0.2, the T_{CO} is lowered to about 200 K, and with further increase in y, the FM emerges at $y = 0.25$ with $T_C \sim 165$ K. As a result, as shown in figure 33(f), the T_{CO} and T_C are comparable at $y = 0.2$–0.25, indicating a prototypical bicritical feature, which is quite similar to the case of $Pr_{0.55}(Ca_{1-y}Sr_y)_{0.45}MnO_3$ (see figures 16 and 17) [77].

It is useful to see how the actual series of solid solutions leave the track on the whole phase diagram and represent a part of the phase variation. Figure 34 shows critical temperatures as a function of r_A for the typical two cases [110]; one (bottom panel) is for the relatively small disorder in moving from $Gd_{0.55}Ca_{0.45}MnO_3$ to $La_{0.55}Sr_{0.45}MnO_3$, i.e. $RE_{0.55}Ca_{0.45}MnO_3$ with varying RE from Gd to Pr, $Pr_{0.55}(Ca_{1-y}Sr_y)_{0.45}MnO_3$ with varying y from 0 to 1, and then $(Pr_{1-y}La_y)_{0.55}Sr_{0.45}MnO_3$ with varying y from 0 to 1. The other (top panel) is for the relatively large disorder, $Gd_{0.55}(Ca_{1-y}Sr_y)_{0.45}MnO_3$, with varying y from 0 to 1 and then $RE_{0.55}Sr_{0.45}MnO_3$ with varying RE from Gd to Pr and La. Both the scanning routes of materials are indicated by thick lines in the middle panel (global phase diagram) of figure 34. In the case with relatively small disorder, a typical bicritical feature is seen with $T_{CO} \sim T_C \sim 200$ K, which occurs at $y \sim 0.2$ in $Pr_{0.55}(Ca_{1-y}Sr_y)_{0.45}MnO_3$ [77]. In the case with a relatively large disorder, the T_{CO} decreases and the CO/OO turns into the SGI as y increases in $Gd_{0.55}(Ca_{1-y}Sr_y)_{0.45}MnO_3$. Even in $RE_{0.55}Sr_{0.45}MnO_3$, the SGI remains for $RE = (Gd_{1-y}Sm_y)$ with $0 \leqslant y \leqslant 0.5$, while it is replaced with the FM with $y > 0.5$. As a result, figure 34 demonstrates that the bicritical feature as seen for relatively small disorder is modified to that intervened by the SGI phase for relatively large disorder, even though the r_A (and hence the averaged lattice structure) is used as a common parameter on the abscissa.

The above essential features have also been reproduced qualitatively by the quantum simulation for somewhat simplified theoretical models of manganites [18, 111–113]. For example, Motome *et al* [112] used the model Hamiltonian as the minimum model which can capture the essence, which is composed of (1) an electron hopping term with the strong-limit Hund's-rule coupling to the local classic spin, leading to the double-exchange interaction, (2) classical phonons which couple to the electron density (breathing mode), (3) the cooperative effect of lattice distortion as arising from the fact that the oxygen displacement affects its connecting MnO_6 octahedra and finally (4) the quenched disorder as represented by the random on-site potential. The model calculation with the lattice size $L \times L$ ($L = 4$, 6 and 8) found the following features near the bicritical point under the competition between the long-range CO (checker-board type) and FM states: (a) the increase in the quenched disorder lowers T_{CO} and finally extinguishes the long-range CO, (b) by increasing the quenched disorder the FM state emerges into the region where the long-range CO is originally present and hence the relatively low T_C state appears near the original bicritical point in the clean limit, (c) outside the FM phase there is no static phase separation between the FM and CO states, but only the short range CO correlation remains and the density of state gap is formed as well in the long-range CO state. These predicted features are in good agreement with the observed features as described above.

The essentially identical features were also successfully reproduced by Aliaga *et al* [113] who have considered the more realistic model, though the system size is limited to 4×4, including the antiferromagnetic coupling J_{AF} between the t_{2g} local spins as well as the orbital degree of freedom. When the role of the quenched disorder is introduced as the randomness of
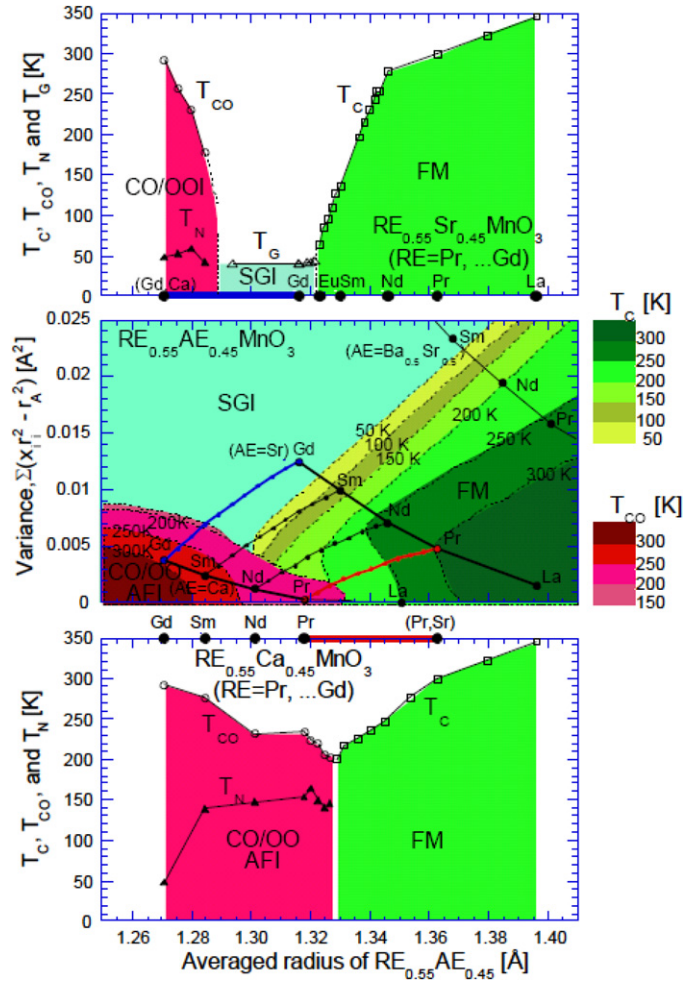
Figure 34. Critical temperatures as a function of r_A for the cases with relatively small (bottom panel) and large (top panel) disorder, respectively. The middle panel reproduces the phase diagram plotted on the $r_A - \sigma^2$ plane, in which the traces of the two cases are drawn. For relatively small disorder, the critical temperatures are plotted in going from $Gd_{0.55}Ca_{0.45}MnO_3$ to $La_{0.55}Sr_{0.45}MnO_3$, through $RE_{0.55}Ca_{0.45}MnO_3$ with RE varying from Gd to Pr, $Pr_{0.55}(Ca_{1-y}Sr_y)_{0.45}MnO_3$ with y varying from 0 to 1, and $(Pr_{1-y}La_y)_{0.55}Sr_{0.45}MnO_3$ with varying y from 0 to 1. For relatively large disorder, those are plotted for the material scans for $Gd_{0.55}(Ca_{1-y}Sr_y)_{0.45}MnO_3$ with y varying from 0 to 1 and for $RE_{0.55}Sr_{0.45}MnO_3$ with RE varying from Gd to Pr and La. For both cases, the T_{CO} and T_C are the averaged values in the cooling and warming runs, which are indicated by open circles and squares, respectively. The Nèel temperature, T_N, and the spin-glass transition temperature, T_G, are denoted by closed and open triangles, respectively. The abbreviations, FM, CO/OO AFI and SGI, are the same as in figure 32 (from [110]).

J_{AF}, the long-range CE spin order with the CO/OO was found to be very susceptible to disorder and turned out to be the glassy state (termed there CE glass), in accord with the observation.

4.4. B-site doping and emergence of magnetic relaxors

Another typical example of the quenched-disorder effect on the bicritical manganites can be seen in the case of doping on the Mn-site with other transition-metal elements, e.g. Cr. The
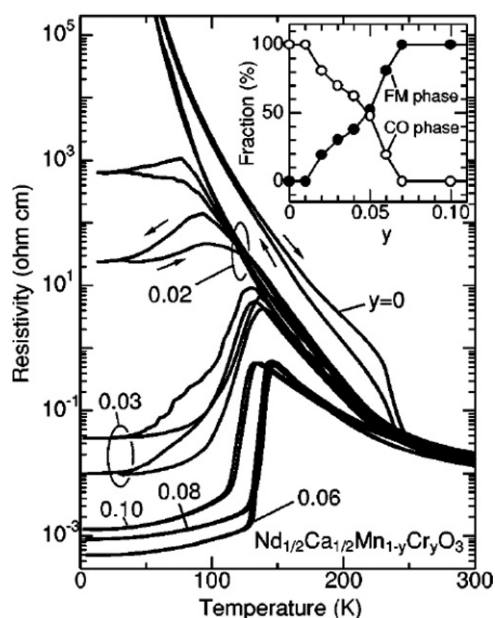
Figure 35. Temperature profiles of resistivity for crystals of $Nd_{1/2}Ca_{1/2}Mn_{1-y}Cr_yO_3$ ($0 \leqslant y \leqslant 0.10$). Inset: fraction of the ferromagnetic-metallic (FM) phase (●) with smaller orthorhombicity and the charge- and orbital-ordered (CO) phase (○) with larger orthorhombicity at 30 K as a function of the Cr content y, as derived by powder x-ray diffraction (from [117]).

dramatic effect of Cr doping in the CE-type charge/orbital ordered (CO/OO) state manganites was first pointed out by Raveau and coworkers [114, 115]. Only several per cent of Cr-substitutes suppresses the long-range CO–OO state and makes the system ferromagnetic-metallic. The Cr impurities (Cr^{3+}: $t_{2g}^3 e_g^0$, $S = 3/2$) may produce not only localized holes but also immovable e_g orbital deficiencies on the Mn sites, which may act as the strong quenched disorder. We describe in the following the case of single crystals of $Nd_{0.5}Ca_{0.5}MnO_3$ doped with Cr (up to 10% on the Mn sites) [116, 117].

The electronic phase diagram of $Nd_{1-x}Ca_xMnO_3$ is similar to that of $Pr_{1-x}Ca_xMnO_3$ (figure 4(c)). The ground state of $Nd_{0.5}Ca_{0.5}MnO_3$ ($x = 0.5$) is a CE-type CO–OO AF insulator. A large external field of more than 20 T is needed to melt the CO–OO AF insulating state in a neat crystal of $Nd_{0.5}Ca_{0.5}MnO_3$, as shown in figure 11. In contrast, only a few per cent of Cr-doping on to the Mn sites can produce the ferromagnetic-metallic (FM) cluster in the bulk of the crystal, which eventually evolves to the whole volume. The crystal is converted to the uniform FM state with further Cr doping (say, above 6%). The respective phase volume of the CO/OO phase and the FM one at 30 K (a low enough temperature to stand for the ground state), as estimated by powder x-ray diffraction, is shown as a function of y in the inset of figure 35 [117]. We also display in figure 35 the temperature profiles of resistivity in $Nd_{0.5}Ca_{0.5}Mn_{1-y}Cr_yO_3$ crystals ($y = 0$ to 0.10). Although the magnitudes of resistivity are comparable around room temperature for all crystals, the low-temperature behaviours depend strongly on the Cr content, y. In the $y = 0$ crystal, a steep rise in resistivity, corresponding to the CO/OO transition, is observed at 220–240 K and insulating behaviour is observed at lower temperatures. Corresponding to the increase in the FM-phase fraction with y, the low-temperature resistivity is drastically suppressed. The crystals with $y \geqslant 0.06$ show an abrupt drop in the resistivity around 120–140 K which is related to the onset of the FM transition and
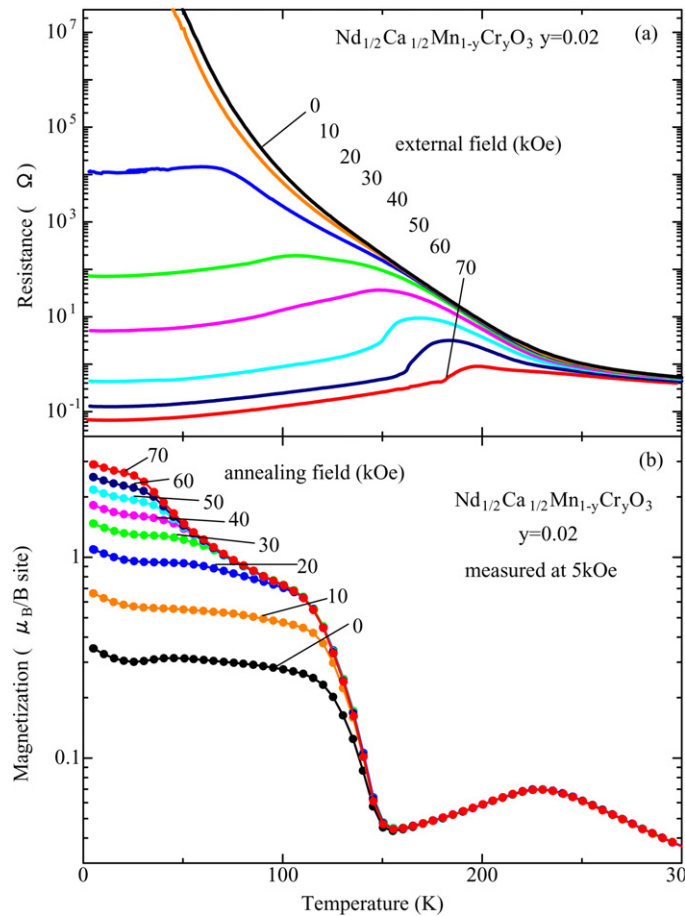
Figure 36. (*a*) Temperature dependence of the resistance in several magnetic fields for a crystal of $Nd_{1/2}Ca_{1/2}Mn_{1-y}Cr_yO_3$ ($y = 0.02$). The measurements were performed in a field-cooling run once the magnetic fields were applied at 300 K. (*b*) Temperature dependence of the magnetization in the warming run at a magnetic field of 5 kOe for the $Nd_{1/2}Ca_{1/2}Mn_{1-y}Cr_yO_3$ ($y = 0.02$) crystal. The measurements were performed once the magnetic fields were applied at 300 K and the crystals were cooled in the respective annealing fields down to 5 K (from [116]).

exhibits metallic behaviour below T_C. The residual resistivity value ranges from as high as $10^3 \, \Omega$ cm to the conventional metal value ($<10^{-3} \, \Omega$ cm), indicating that the Cr-doping induced insulator–metal transition is attributed to the percolation transition in the inhomogeneous state.

In the following, we focus on the $y = 0.02$ crystal in which the volume fraction of the FM phase is close to a threshold concentration for percolation in a simple cubic lattice ($p_c \sim 16\%$) [118]. We display in figure 36(*a*) the temperature profiles of the resistance for the $y = 0.02$ crystal in various external magnetic fields [117]. The resistance shows an insulating behaviour down to the lowest temperature in the absence of a magnetic field. The application of magnetic field reduces the resistance below $T_{CO} \sim 230$ K and makes the system semi-metallic. The value of resistance at the ground state varies with the magnitude of the applied magnetic field, indicating the field variation in the FM volume fraction. Figure 36(*b*) shows the magnetic-field annealing effect on the magnetization. For these measurements, the crystal was cooled from 300 to 5 K in the respective magnetic fields. Then the magnetization was

measured by warming the crystal in a relatively small magnetic field of 0.5 T. The anomaly around 230 K is observed in all the data and is related to the onset of the CO–OO transition. In the temperature range above ∼150 K, no difference in the magnetization was observed. The steep rise in magnetization towards low temperatures is observed at ∼150 K, which is attributed to the onset of ferromagnetic spin ordering. A striking feature in figure 36(b) is that the magnitude of the magnetization below T_C, or equivalently the fraction of the FM phase, is totally governed by the magnitude of the annealing magnetic field. Importantly, the respective values of the resistivity and magnetization at 5 K are maintained at the field-cooled values even after removing the magnetic field at 5 K. In the case of zero-field cooling the fraction of the FM phase remains as small as 20% of the whole crystal, whereas in the case of above-7 T field cooling the FM volume fraction reaches almost 100% [116].

At finite temperatures under some external magnetic fields, a typical long-time relaxation or ageing effect is observed for magnetization as well as for the conductance in such a phase-separated state. In the case where the volume fraction of the FM phase is close to the percolation threshold, this ageing effect even leads to the *temporal* insulator–metal transition [116]. Such magnetic-field annealing and ageing effects on the temporal evolution of the FM micro-embryos in the CO/OO AF matrix bear close analogy to the case of *relaxor ferroelectrics* [119]. In the relaxor ferroelectrics, e.g. $PbMg_{1/3}Nb_{2/3}O_3$, ferroelectric domains embedded in a paraelectric matrix show electric-field annealing and ageing effects, corresponding to the evolution of micropolar clusters by an external electric field. Although most of the relaxor ferroelectrics in perovskites are lead (Pb) based compounds with alloyed heterovalent B-sites expressed as $Pb(B, B')O_3$, diluted impurity systems such as $K_{1-x}Li_xTaO_3$ and $Sr_{1-x}Ca_xTiO_3$ also exhibit all of the above typical properties. One of the promising models for explaining the diffuse transitions of relaxor ferroelectrics is the random-field interaction scheme [120]. It is assumed that the quenched random electric fields are caused by random distribution of different ions on A or B sites [121].

This random field model seems to approximately apply as well to the present manganese oxides in the bicritical region where doped impurities induce the CO/OO-to-FM transition. In this sense, the quenched random field in terms of charge and orbital sectors originating from the Cr^{3+} impurities as e_g-orbital deficiencies is likely to be responsible for all the observed relaxor characteristics, namely the diffuse CO/OO transition accompanying the phase-separation, the field- or time-dependent evolution of FM clusters and the resulting percolative insulator–metal transition.

As argued in figure 27, the *strong* disorder as caused by Cr doping generates the coexistent phases, CO/OOI and FM, on various length scales, ranging from nanometres to micrometres [122]. Note, however, that the Cr doping above some threshold ($y_c = 0.06$) produces the coarse-grained homogeneous phase, the fully FM state below T_C and only the nanometric short-range order above T_C (see figure 35). Thus, the nature of Cr doping as the quenched disorder in this bicritical region undergoes a crossover from a strong to a weak regime with an increase in the concentration y in the light of the scheme shown in figure 27. This bears a close analogy to the issue of weak versus strong pinning in the charge-density-wave (CDW) system [123].

5. Concluding remarks

The perovskite manganites can offer an ideal arena to investigate the interrelated effects of strong electron-correlation and electron–lattice coupling on the metal–insulator phenomena, in which the two important electronic parameters, bandwidth and band-filling, can be finely controlled with the crystal chemistry. The strong electron correlation makes both the spin

and orbital degrees of freedom active, and these degrees of freedom together with charge can produce versatile electronic phases on such a simple perovskite lattice. The collective Jahn–Teller interaction in this orbitally active system promotes the orbital ordering through the displacement of oxygen in a cooperative manner and varies the electronic anisotropy or dimension. The CMR is the magnetically induced metal–insulator phenomenon; therefore, the extreme sensitivity of the less-conducting state to the magnetic field is the key issue of CMR physics. We have argued with ample experimental evidence that the phase competition among the ferromagnetic and the charge–orbital ordered (and in some cases also the A-type layered antiferromagnetic) states is essential in forming the bicritical (or multi-critical) point near which the CMR response is generally observed. The long-range or short-range charge–orbital ordering correlations are amenable to external magnetic fields which favour the competing ferromagnetic state.

The essential ingredients of the CMR mechanism are not only the phase competition but also the unexpectedly important role of quenched disorder. In this paper, we argued the two prototypical cases: in one case (case I), the presence of quenched disorder suppresses the long-range charge–orbital order and turns the correlation to short-range or glass-like. In this case, the first-order ferromagnetic transition temperature T_C is also steeply suppressed near the original bicritical point. By decreasing the temperature to T_C, the charge–orbital correlation evolves in magnitude, but not in length-scale, and below T_C is suddenly extinguished in the ferromagnetic metallic state. The CMR phenomenon is most pronounced in the short-range charge–orbital correlated state just above the lowered T_C or in the glassy state. Namely, the magnetic-field induced extinguishment of the charge–orbital correlation with high efficiency near the bicritical point under the moderate quenched disorder is the microscopic origin of the CMR.

In another important case (case II), the quenched disorder may produce phase separation into the charge–orbital ordered state and the ferromagnetic-metallic one near the bicritical region. Examples of quenched disorder for this case are Cr (or other transition-metal element) doping on the Mn sites and the grain boundaries of polycrystals or lattice imperfections in the crystal domain. Note, however, that the increase in Cr content may drive the system to the macroscopically homogeneous CMR state characteristic of case I. The combined effect of case I and case II is occasionally seen in less-qualified specimens reported in the vast literature or even in high-quality single-domain single crystals located in the immediate vicinity of the bicritical point. In this case, the percolation type insulator–metal transition or cross-over is observed as the CMR phenomenon. However, this *static* or *semi-macroscopic* percolation picture should be strictly distinguished from case I, where the CMR mother state is the well-defined short-range (typically on a length scale of 1–2 nm) charge–orbital correlation, either dynamical above T_C or frozen in the spin-glass phase adjacent to the lowered-T_C phase.

As a final note, let us briefly mention the possible application of the present idea of the multi-critical phase competition to the more general phase control of the electron-correlated oxides. So far, we have confined ourselves to the magnetic control of the bicritical (multi-critical) phase competition. However, any other external stimuli which may unbalance the competing phases can trigger the dramatic phase conversion on a macroscopic scale and/or in a percolative manner. Consider, for example, the case of photo-excitation in the charge–orbital ordered state near the bicritical region. The photo-excitation above the charge gap, typically 0.5 eV, in the charge–orbital ordered state can cause the hopping of the e_g electron into the neighbouring site, hence forming local defects in the regular charge–orbital ordered state. The tuning of the photo-excitation intensity may thus correspond to the concentration of the doped *disorder*, and hence may lead to the local or global melting of the charge–orbital order or the generation of the hidden competing ferromagnetic metallic phase. Intuitively, a similar
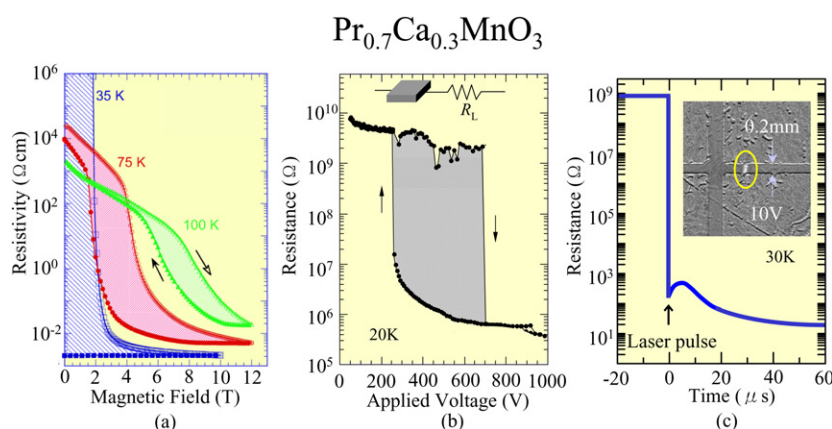
$$Pr_{0.7}Ca_{0.3}MnO_3$$

Figure 37. Insulator–metal phase control in $Pr_{0.7}Ca_{0.3}MnO_3$: (*a*) resistivity change by application of an external magnetic field, (*b*) resistance change by applying a voltage on the circuit connecting the sample with the electrode distance of 1 mm and the load resistance ($R_L = 1\,M\Omega$) in series and (*c*) resistance change upon the 7 ns pulse laser irradiation of the sample with the electrode distance of 0.2 mm and the applied voltage of 10 V. The inset in (*c*) shows the region of the current path (a white streak between the gold electrodes with the separation of 0.2 mm), reflecting the change in reflectance of the crystal surface due to the local insulator–metal transition (from [17]).

situation may happen in the case of current (electron or hole) injection into the charge–orbital ordered state: the current injection may cause local disorder and would eventually cause the local melting of the charge–orbital order. When the percolation is effective, this would result in a gigantic reduction in the resistance. Of course, the analogy between the case of the chemically doped quenched disorder and such a dynamical melting of the charge–orbital order in the nonequilibrium state should be of limited use, but this kind of local (perhaps associated with the metal–insulator phase separation) transition by external stimuli is ubiquitously observed in the bicritical manganites, as exemplified in the following.

Taking the $Pr_{0.7}Ca_{0.3}MnO_3$ crystal as an example, figure 37 displays the three prototypical cases of the local or global transition from the charge–orbital ordered insulator to the (ferromagnetic) metal state [17]: external stimuli are (*a*) magnetic field, (*b*) electric field and (*c*) photo-excitation, respectively. In addition to the well-known case of the magnetic field induced insulator–metal transition (figure 37(*a*)), an electric field as small as $2000\,V\,cm^{-1}$ or the related current injection can cause the local insulator–metal transition as shown in figure 37(*b*) [16]. The load resistance connected in series to the sample plays a role in stabilizing the low-resistance state switched from the original high-resistance, namely the charge–orbital ordered state. This is to be called the dielectric breakdown of the *electron crystal*, yet the percolated conducting path should be local and filamentary judging from the resistance value of the low-resistance state. A similar resistance switching can occur in a low or even zero applied electric field when the trigger is given by photo-excitation [13, 124] or x-ray irradiation [14]. Figure 37(*c*) shows the case when the 7 ns pulse laser (1.2 eV) excitation is made in the region between the gold electrodes with a gap of 0.2 mm under an applied voltage of 5 V [124]. Upon photo-excitation, the resistance shows a gigantic decrease from a $G\Omega$ value to a metallic one as shown in the inset, and the metallic state is maintained during the voltage application. The inset to figure 37(*c*) shows the *colour change* (or more correctly the reflectivity change) in the current path region or the current-induced metallic state. More recently, there have been several publications related to the photo-induced melting of the charge–orbital order in the perovskite or layered-perovskite manganites. All show that the local melting of the long-range

order occurs in an ultrafast manner, i.e. electronically, within the excitation laser pulse width ($\approx 100\,\text{fs} = 10^{-13}\,\text{s}$) [125, 126]. Subsequently the heating-up of the lattice occurs during several picoseconds, and then the orbital disorder tends to be remedied by the thermalization process which usually occurs after several nanoseconds.

The ultrafast modification of the electronic phases enabled by the femto-second laser excitation may find some application in the future. The actual process of the first-order phase transition or the induced phase-separation in the nonequilibrium state involves the excitation density-dependent effects including the nucleation dynamics of the transformed phase region as well as the coherent and/or incoherent coupling with the lattice and orbital excitations. In this context, the orbital excitation or *orbiton*, which was argued in the case of LaMnO$_3$ for the manganite [127], can have high frequency, typically 10^{13}–10^{14} Hz, being comparable to, or even higher than, the optical phonon frequency. This may favour the ultrafast manipulation of the orbital-ordering related electronic phase, since the dynamical process of the order melting is limited by the frequencies of the elementary excitations, such as phonons, magnons, orbitons and excitons, which are relevant to the phase changes.

The possible phase change enabled by electric stimuli is also of current interest in the light of possible application to nonvolatile fast memory devices. In fact, the memory switching between the high-resistance and low-resistance states depending on the polarity of the voltage stress has been reported for thin films of Pr$_{0.7}$Ca$_{0.3}$MnO$_3$ (PCMO) by Ignatiev *et al* [128], which has been confirmed by many other research groups. More recently, such colossal electro-resistance memory (CERM) phenomena have been found for many junctions between specific metal electrodes and correlated-electron oxides. The origin of the CERM effect is under vital investigation, but the consensus is being established that the CERM may originate from the change in the electronic and/or structural properties of the interface between the insulating PCMO and the metal electrode, e.g. Ti or Al [129], upon voltage stress. The possibility of control of the chemical potential (doping level) of the correlated insulator by an external bias field will open a new field for correlated-electron devices. There, the high sensitivity of the competing phases against the external field as typically demonstrated for the case of CMR will be a key issue as well.

Acknowledgments

References

[1] For comprehensive reviews, see for example, Tokura Y (ed) 1999 *Colossal Magnetoresistive Oxides* (London: Gordon and Breach)
     Coey J M D, Viret M and von Molnar S 1999 *Adv. Phys.* **48** 167
     Salamon M B and Jaime M 2001 *Rev. Mod. Phys.* **73** 583
     Dagotto E, Hotta T and Moreo A 2002 *Phys. Rep.* **344** 1
     Dagotto E 2002 *Phase Separation and Colossal Magnetoresistance* (Berlin: Springer)
[2] Searle C W and Wang S T 1969 *Can. J. Phys.* **47** 2023
[3] Kubo K and Ohata N 1972 *J. Phys. Soc. Japan.* **33** 21
[4] Zener C 1951 *Phys. Rev.* **82** 403
[5] Anderson P W and Hasegawa H 1955 *Phys. Rev.* **100** 67
[6] De Gennes P-G 1960 *Phys. Rev.* **118** 141
[7] Kusters R M, Singleton D A, Keen D A, McGreevy R and Hayes W 1989 *Physica B* **155** 362
[8] Chabara K, Ohno T, Kasai M and Kozono Y 1993 *Appl. Phys. Lett.* **63** 1990

[9] von Helmolt R, Wocker J, Holzapfel B, Schultz M and Samwer K 1993 *Phys. Rev. Lett.* **71** 2331

[10] Jin S, Tiefel T H, McCormack M, Fastnacht R A, Ramesh R and Chen L H 1994 *Science* **264** 413

[11] Tokura Y, Urushibara A, Moritomo Y, Arima T, Asamitsu A, Kido G and Furukawa N 1994 *J. Phys. Soc. Japan* **63** 3931

[12] Asamitsu A, Moritomo Y, Tomioka Y, Arima T and Tokura Y 1995 *Nature* **373** 407

[13] Miyano K, Tanaka T, Tomioka Y and Tokura Y 1997 *Phys. Rev. Lett.* **78** 4257

[14] Kiryukhin V, Casa D, Hill J P, Keimer B, Vigliante A, Tomioka Y and Tokura Y 1997 *Nature* **386** 813

[15] Raveau B, Maignan A and Martin C 1997 *J. Solid State Chem.* **130** 162

[16] Asamitsu A, Tomioka Y, Kuwahara H and Tokura Y 1997 *Nature* **388** 50

[17] Tokura Y 2003 *Phys. Today* **56** 50

[18] Dagotto E 2005 *Science* **309** 257 and references cited therein

[19] Sugano S, Tanabe Y and Kamimura H 1970 *Multiplets of Transition-Metal Ions in Crystals* (New York: Academic)

[20] Kanamori J 1960 *J. Appl. Phys.* **31** 14S

[21] MullerHartmann E and Dagotto E 1996 *Phys. Rev.* B **54** R6819

[22] Ye J W, Kim Y B, Millis A J, Shraiman B I, Majumdar P and Tesanovic Z 1999 *Phys. Rev. Lett.* **83** 3737

[23] Lyanda-Geller Y, Chun S H, Salamon M B, Goldbart P M, Han P D, Tomioka Y, Asamitsu A and Tokura Y 2001 *Phys. Rev.* B **63** 184426

[24] Taguchi Y, Oohara Y, Yoshizawa H, Nagaosa N and Tokura Y 2001 *Science* **291** 2573

[25] Furukawa N 1994 *J. Phys. Soc. Japan* **63** 3214

[26] Millis A J, Littlewood P B and Shraiman B I 1995 *Phys. Rev. Lett.* **74** 5144

[27] Goodenogh J B and Longo J M 1970 *Magnetic and Other Properties of Oxides and Related Compounds* ed K-H Hellwege and O Madelung (*Landolt-Bornstein New Series, Group III*) vol 4 Pt. a (Berlin: Springer)

[28] Shannon R D 1976 *Acta Crystallogr.* A **21** 751

[29] Imada M, Fujimori A and Tokura Y 1998 *Rev. Mod. Phys.* **70** 1039

[30] Torrance J B, Lacorre P, Nazzal A, Ansaldo E J and Nidermayer C 1992 *Phys. Rev.* B **45** 8209

[31] Hwang H Y, Cheong S W, Radaelli P G, Marezio M and Batlogg B 1995 *Phys. Rev. Lett.* **75** 914

[32] Tokura Y and Tomioka Y 1999 *J. Magn. Magn. Mater.* **200** 1

[33] Murakami Y *et al* 1998 *Phys. Rev. Lett.* **81** 582

[34] Kimura T, Ishihara S, Shintani H, Arima T, Takahashi K T, Ishizaka K and Tokura Y 2003 *Phys. Rev.* B **68** 060403

[35] Kimura T, Goto T, Shintani H, Ishizaka K, Arima T and Tokura Y 2003 *Nature* **426** 55

[36] Wollan E O and Koehler W C 1955 *Phys. Rev.* **100** 545

[37] Urushibara A, Moritomo Y, Arima T, Asamitsu A, Kido G and Tokura Y 1995 *Phys. Rev.* B **51** 14103

[38] Okuda T, Asamitsu A, Tomioka Y, Kimura T, Taguchi Y and Tokura Y 1998 *Phys. Rev. Lett.* **81** 3203

[39] Kawano H, Kajimoto R, Kubota M and Yoshizawa H 1996 *Phys. Rev.* B **53** R4109
      Kawano H, Kajimoto R, Kubota M and Yoshizawa H 1996 *Phys. Rev.* B **53** R2202

[40] Yamada Y, Hino O, Nohdo S, Kanao R, Inami T and Katano S 1996 *Phys .Rev. Lett.* **77** 904

[41] Endoh Y *et al* 1999 *Phys. Rev. Lett.* **82** 4328

[42] Moussa F, Hennion M, Wang F, Kober P, Rodriguez-Carvajal J, Reutler P, Pinsard L and Revcolevschi A 2003 *Phys. Rev.* B **67** 214430

[43] Korotin M, Fujiwara T and Anisimov V 2000 *Phys. Rev.* B **62** 5696

[44] Kajimoto R, Mochizuki H, Yoshizawa H, Okamoto S and Ishihara S 2004 *Phys. Rev.* B **69** 054433

[45] Fujishiro H, Ikebe M and Konno Y 1998 *J. Phys. Soc. Japan* **67** 1799

[46] Moritomo Y, Akimoto T, Nakamura A, Ohoyama K and Ohashi M 1998 *Phys. Rev.* B **58** 5544

[47] Kawano H, Kajimoto R, Yoshizawa H, Tomioka Y, Kuwahara H and Tokura Y 1997 *Phys. Rev. Lett.* **78** 4253

[48] Kuwahara H, Okuda T, Tomioka Y, Asamitsu A and Tokura Y 1999 *Phys. Rev. Lett.* **82** 4316

[49] Kajimoto R, Yoshizawa H, Kawano H, Kuwahara H, Tokura Y, Ohoyama K and Ohashi M 1999 *Phys. Rev.* B **60** 9506

[50] Kuwahara H, Tomioka Y, Asamitsu A, Moritomo Y and Tokura Y 1995 *Science* **270** 961

[51] Goodenough J B 1955 *Phys. Rev.* **100** 564

[52] Jirak Z, Krupicka S, Simsa Z, Dlouha M and Vlatislav Z 1985 *J. Magn. Magn. Mater.* **53** 153

[53] Yoshizawa H, Kawano H, Tomioka Y and Tokura Y 1995 *Phys. Rev.* B **52** R13145

[54] Maezono R, Ishihara S and Nagaosa N 1998 *Phys. Rev.* B **58** 11583

[55] Kajimoto R, Yoshizawa H, Tomioka Y and Tokura Y 2002 *Phys. Rev.* B **66** 180402

[56] Tobe K, Kimura T and Tokura Y 2004 *Phys. Rev.* B **69** 014407

[57] Ishihara S, Yamanaka M and Nagaosa N 1997 *Phys. Rev.* B **56** 686

[58] Horsch P, Jaklic J and Mack F 1999 *Phys. Rev.* B **59** 6217

[59] Tobe K, Kimura T and Tokura Y 2003 *Phys. Rev.* B **67** 140402
[60] Cuoco M, Noce C and Oles A M 2002 *Phys. Rev.* B **66** 090427
[61] Huang D J *et al* 2004 *Phys. Rev. Lett.* **92** 87202
[62] Wilkins S B, Stojic N, Beale T A W, Binggeli N, Castleton C W M, Bencok P, Prabhakaran D, Boothroyd A T, Hatton P D and Altarelli M 2005 *Phys. Rev.* B **71** 245102
[63] Sternlieb B J, Hill J P, Wildgruber U C, Luke G M, Nachumi B, Moritomo Y and Tokura Y 1996 *Phys. Rev. Lett.* **76** 2169
[64] Tomioka Y, Asamitsu A, Moritomo Y, Kuwahara H and Tokura Y 1995 *Phys. Rev. Lett.* **74** 5108
[65] Tokunaga M, Miura N, Tomioka Y and Tokura Y 1998 *Phys. Rev.* B **57** 5259
[66] Jirak Z, Krupicka S, Simsa Z, Dlouha M and Vlatislav Z 1985 *J. Magn. Magn. Mater.* **53** 153
[67] Tomioka Y, Asamitsu A, Kuwahara H and Tokura Y 1996 *Phys. Rev.* B **53** R1689
[68] Asaka T, Yamada S, Tsutsumi S, Tsuruta C, Kimoto K, Arima T and Matsui Y 2002 *Phys. Rev. Lett.* **88** 097201
[69] Chen C H, Cheong S W and Hwang H Y 1997 *J. Appl. Phys.* **81** 4326
[70] Liu K, Wu X W, Ahn K H, Sulchek T, Chien C L and Xiao J Q 1996 *Phys. Rev.* B **54** 3007
[71] Okimoto Y, Tomioka Y, Onose Y, Otsuka Y and Tokura Y 1998 *Phys. Rev.* B **57** R9377
     Okimoto Y, Tomioka Y, Onose Y, Otsuka Y and Tokura Y 1999 *Phys. Rev.* B **59** 7401
[72] Tomioka Y, Asamitsu A, Kuwahara H and Tokura Y 1997 *J. Phys. Soc. Japan* **66** 302
[73] Tokura Y, Tomioka Y, Kuwahara H, Asamitsu A, Moritomo Y and Kasai M 1996 *J. Appl. Phys.* **79** 5288
[74] Maezono R, Ishihara S and Nagaosa N 1998 *Phys. Rev.* B **58** 11583
[75] Millis A J, Mueller R and Shraiman B I 1996 *Phys. Rev.* B **54** 5405
[76] Solovyev I V 2003 *Phys. Rev. Lett.* **91** 177201
[77] Tomioka Y and Tokura Y 2002 *Phys. Rev.* B **66** 104416
[78] Yoshizawa H, Kajimoto R, Kawano H, Tomioka Y and Tokura Y 1997 *Phys. Rev.* B **55** 2729
[79] Murakami S and Nagaosa N 2003 *Phys. Rev. Lett.* **90** 197201
[80] Salamon M B, Lin P and Chun S H 2002 *Phys. Rev. Lett.* **88** 197203
[81] Rodriguez-Martinez L M and Attfield J P 1998 *Phys. Rev.* B **54** 15622
[82] Tomioka Y, Okimoto Y, Jung J H, Kumai R and Tokura Y 2003 *Phys. Rev.* B **68** 094417
[83] Tomioka Y, Kuwahara H, Asamitsu A, Kasai M and Tokura Y 1997 *Appl. Phys. Lett.* **70** 3609
[84] Terai T, Sakai T, Kakeshita T, Fukuda T, Saburi T, Kitagawa H, Kindo K and Honda M 2000 *Phys. Rev.* B **61** 3488
[85] Sundaresan A, Maignan A and Raveau B 1997 *Phys. Rev.* B **55** 5596
[86] Shimomura S, Wakabayashi N, Kuwahara H and Tokura Y 1999 *Phys. Rev. Lett.* **83** 4389
[87] Shimomura S, Tonegawa T, Tajima K, Wakabayashi N, Ikeda N, Shobu T, Noda Y, Tomioka Y and Tokura Y 2000 *Phys. Rev.* B **62** 3875
[88] Jirak Z, Damay F, Herview M, Martin C, Raveau B, Andre G and Bouree F 2000 *Phys. Rev.* B **61** 1181
[89] Saitoh E, Tomioka Y, Kimura T and Tokura Y 2000 *J. Phys. Soc. Japan* **69** 2403
[90] Yamamoto K, Kimura T, Ishikawa T, Katsufuji T and Tokura Y 2000 *Phys. Rev.* B **61** 14706
[91] Okimoto Y, Katsufuji T, Ishikawa T, Urushibara A, Arima T and Tokura Y 1995 *Phys. Rev. Lett.* **75** 109
     Okimoto Y, Katsufuji T, Ishikawa T, Arima T and Tokura Y 1997 *Phys. Rev.* B **55** 4206
[92] Saitoh E, Okimoto Y, Tomioka Y, Katsufuji T and Tokura Y 1999 *Phys. Rev.* B **60** 10362
[93] Hwang H Y, Dai P, Cheong S W, Aeppli G, Tennant D A and Mook H A 1998 *Phys. Rev. Lett.* **80** 1316
[94] Endoh Y, Hiraka H, Tomioka Y, Tokura Y, Nagaosa N and Fujiwara T 2005 *Phys. Rev. Lett.* **94** 017206
[95] Attfield J P 1998 *Chem. Mater.* **10** 3239
[96] Millange F, Caignaert V, Domenges B, Raveau B and Suard E 1998 *Chem. Mater.* **10** 1974
[97] Nakajima T, Kageyama H and Ueda Y 2002 *J. Phys. Chem.* **63** 913
[98] Akahoshi D, Uchida M, Tomioka Y, Arima T, Matsui Y and Tokura Y 2003 *Phys. Rev. Lett.* **90** 177203
[99] Nakajima T, Yshizawa H and Ueda Y 2004 *J. Phys. Soc. Japan* **73** 2283
[100] Mathieu R, Akahoshi D, Asamitsu A, Tomioka Y and Tokura Y 2004 *Phys. Rev. Lett.* **93** 227202
[101] Uchida M, Akahoshi D, Kumai R, Tomioka Y, Arima T, Tokura Y and Matsui Y 2002 *J. Phys. Soc. Japan* **71** 2605
[102] Arima T, Akahoshi D, Oikawa K, Kamiyama T, Uchida M, Matsui Y and Tokura Y 2002 *Phys. Rev.* B **66** 140408
[103] Nakajima T, Kageyama H, Yoshizawa H and Ueda Y 2002 *J. Phys. Soc. Japan* **71** 2843
[104] Kageyama H, Nakajima T, Ichihara M, Ueda Y, Yoshizawa H and Ohoyama K 2003 *J. Phys. Soc. Japan.* **72** 241
[105] Akahoshi D, Okimoto Y, Kubota M, Kumai R, Arima T, Tomioka Y and Tokura Y 2004 *Phys. Rev.* B **70** 064418
[106] Nakajima T, Kageyama H, Yoshizawa H, Ohoyama K and Ueda Y 2003 *J. Phys. Soc. Japan* **72** 3237
[107] Rodriguez-Martinez L M and Attfield J P 2000 *Phys. Rev.* B **63** 024424

[108] Tokura Y, Kuwahara H, Moritomo Y, Tomioka Y and Asamitsu A 1996 *Phys. Rev. Lett.* **76** 3184
[109] Kuwahara H, Moritomo Y, Tomioka Y, Asamitsu A, Kasai M, Kumai R and Tokura Y 1997 *Phys. Rev.* B **56** 9386
[110] Tomioka Y and Tokura Y 2004 *Phys. Rev.* B **70** 014432
[111] Burgy J, Mayr M, Martin-Mayor V, Moreo A and Dagotto E 2001 *Phys. Rev. Lett.* **87** 277202
[112] Motome Y, Furukawa N and Nagaosa N 2003 *Phys. Rev. Lett.* **91** 167204
[113] Aliaga H, Magnoux D, Moreo A, Poilblanc D, Yunoki S and Dagotto E 2003 *Phys. Rev.* B **68** 104405
[114] Barnabe A, Maignan A, Hervieu M, Damay F, Martin C and Raveau B 1997 *Appl. Phys. Lett.* **71** 3907
[115] Raveau B, Maignan A and Martin C 1997 *J. Solid State Chem.* **130** 162
[116] Kimura T, Tomioka Y, Kumai R, Okimoto Y and Tokura Y 1999 *Phys. Rev. Lett.* **83** 3940
[117] Kimura T, Kumai R, Okimoto Y, Tomioka Y and Tokura Y 2000 *Phys. Rev.* B **62** 15021
[118] Scher H and Zallen R 1970 *J. Chem. Phys.* **53** 3759
[119] For example, Cross L E 1987 *Ferroelectrics* **76** 241
     Cross L E 1994 *Ferroelectrics* **151** 305
[120] Imry Y and Ma S-K 1975 *Phys. Rev. Lett.* **35** 1399
[121] Westphal V, Kleemann W and Glinchuk M D 1992 *Phys. Rev. Lett.* **68** 847
[122] Mori S, Shoji R, Yamamoto N, Asaka T, Matsui Y, Machida A, Moritomo Y and Katsufuji T 2003 *Phys. Rev.* B **67** 012403
[123] Gruner G 1988 *Rev. Mod. Phys.* **60** 1129
[124] Fiebig M, Miyano K, Tomioka Y and Tokura Y 1998 *Science* **280** 1925
[125] Ogasawara T, Kimura T, Ishikawa T, Kuwata-Gonokami M and Tokura Y 2001 *Phys. Rev.* B **63** 113105
[126] Ogasawara T, Tobe K, Kimura T, Okamoto H and Tokura Y 2002 *J. Phys. Soc. Japan* **71** 2380
[127] Saitoh E, Okamoto S, Takahashi K T, Tobe K, Yamamoto K, Kimura T, Ishihara S, Maekawa S and Tokura Y 2001 *Nature* **410** 180
[128] Liu SQ, Wu NJ and Ignatiev A 2000 *Appl. Phys. Lett.* **76** 2749
[129] Sawa A, Fujii T, Kawasaki M and Tokura Y 2004 *Appl. Phys. Lett.* **85** 4073